Western Graduate&PostdoctoralStudies

Western University
Scholarship@Western

Electronic Thesis and Dissertation Repository

8-22-2022 10:00 AM

Numerical Analysis of Internal Hydraulic Jump in Complex Topography

Dylan MacRiner, *The University of Western Ontario*

Supervisor: Ogden, Kelly A, *The University of Western Ontario*

A thesis submitted in partial fulfillment of the requirements for the Master of Engineering Science degree in Mechanical and Materials Engineering

© Dylan MacRiner 2022

Follow this and additional works at: https://ir.lib.uwo.ca/etd

Part of the Hydraulic Engineering Commons, and the Ocean Engineering Commons

Recommended Citation

MacRiner, Dylan, "Numerical Analysis of Internal Hydraulic Jump in Complex Topography" (2022). *Electronic Thesis and Dissertation Repository*. 8765.
https://ir.lib.uwo.ca/etd/8765

This Dissertation/Thesis is brought to you for free and open access by Scholarship@Western. It has been accepted for inclusion in Electronic Thesis and Dissertation Repository by an authorized administrator of Scholarship@Western. For more information, please contact wlswadmin@uwo.ca.

Abstract

Topographic effects on internal hydraulic jumps in stratified flow over complex geometry are studied. The simulations are motivated by flow conditions present in a channel in Hood Canal, Washington with continuous density profiles and constant inlet velocities. Results show that mixing in the domain is typically increased by topographic variation, where isolated expansions saw an increase in mixing, but the associated velocity decrease in expansions had contrasting effects on mixing. Likewise, a contraction with an increased velocity caused more mixing, seeing geometry change and velocity acting as compounding factors. 2D results including along channel topographic variation modelled after Hood Canal's topography and density profiles differed from observational results because channel width variation was excluded, but mixing was affected by the direction of the flow over the topography, and the density profile. Given these results, future work into more realistic 3D simulations is encouraged.

Keywords: Hood Canal, Internal Hydraulic Jump, Mixing, Complex Geometry

Summary for Lay Audience

A hydraulic jump is a phenomenon that can occur when a flow of relatively high speed is forced to abruptly transition to a low speed, typically due to a change in topography, or the meeting of high and low speed flows. This velocity transition is accompanied by a large amount of turbulence that is dissipative in nature, and often utilized by engineers in dams and spillways as a method of flow control. Hydraulic jumps also frequently occur in nature for and the turbulence associated with this phenomenon can modify water properties and affect aquaculture in various regions across the globe. Not only can this phenomenon occur at the surface of flows with a constant density, but they are also known to occur internally in flows that have density variation, like those seen in channels and straits, or in the open ocean.

Of particular interest is the indication that a hydraulic jump is occurring in Hood Canal, a channel located in the Kitsap Peninsula, in Washington State, USA. Hood Canal periodically experiences a reduction in the amount of oxygen dissolved in the water, resulting in a large number of fish dying over a short period; the amount of mixing caused by a hydraulic jump in the channel may affect the severity of these events. Some observational data has shown that a hydraulic jump may be occurring in an area of the channel where the topography is complex, such as expanding then contracting walls, and a drastic and abrupt change in the channel depth. The effect that the complex boundaries have on the mixing and intensity of hydraulic jumps has not previously been thoroughly investigated, and is the focus of this work. Using computational fluid dynamics to simulate hydraulic jumps in 3 cases; a 3D domain with an expansion, a 3D domain with a contraction and a 2D domain with a complex bottom are investigated. The results show that as, the width of the channel expands or contracts, mixing increases, and that complex bottom topography is important to consider.

Acknowlegements

First and foremost, I would like to express my sincere gratitude toward my advisor Dr. Kelly Ogden for her continued support and assistance throughout my study and research. Her patience, enthusiasm and motivation when challenges arose helped me immensely throughout the completion of my work and degree, as well as her incredible knowledge of the topics covered. I could not have imagined having a better advisor to mentor me through the completion of this work.

In addition to my advisor, I would like to extend my sincere thanks to Dr. Eric Savory for his contribution and insightful feedback during the tail end of my thesis completion. He provided helpful comments to keep my scope narrow and complete.

Finally, I would like to extend a thank you to MITACS for the Research Training Award in support of my thesis.

Nomenclature

General Fluid Mechanics

A - Cross-sectional area

c - Wave speed

D - Two-layer channel depth

ϵ - Turbulent dissipation rate

$F_r = \sqrt{\frac{u^2+v^2}{gD}}$ - Froude Number

g - Gravity

H - Channel depth

κ - Density diffusivity

$L_B = \frac{L_k}{\sqrt{Pr}}$ - Batchelor scale

$L_K = (\frac{\nu^3}{\epsilon})$ - Komogorov scale

M - Momentum flux

$N^2 = \frac{-g}{\rho_0}\frac{\mathrm{d}P}{\mathrm{d}z}$ - Buoyancy frequency

ρ - Density

ρ_0 - Reference density

p - Absolute pressure

Pr - Prandtl number

Q - Volume flow rate

u, v, w - Velocity components in x, y, z

$\mathbf{V} = \sqrt{u^2 + v^2}$ - Velocity magnitude

$\omega = \frac{\partial u}{\partial y} - \frac{\partial v}{\partial x}$ - Vorticity

Θ - Turbulent component of scalar quantity

Simulation Parameters

b - Minimum channel width

h_1, h_2 - Sill height and 0.9% of Sill Height

L - Length Scale

L_x, L_{x2} - First and second Sill locations

$R(x)$ - Interface Height

q - Rate of expansion

m - Expansion width

U_{sill} - Velocity at jump sill

U_0 - Inlet velocity

t - Averaging times

T - Simulation density

Contents

Abstract i

Summary for Lay Audience ii

Acknowlegements iii

Nomenclature iv

List of Figures ix

List of Tables xvi

1 Introduction 1

1.1 Hood Canal . . . 3

1.2 Background and Theory . . . 5

1.2.1 Hydraulic Jump . . . 5

1.2.2 Boussinesq & Incompressible Approximation . . . 8

1.2.3 Internal Hydraulic Jump in Two-Layer Flows . . . 11

1.2.4 Stratified Flow Over Topography . . . 16

1.3 Literature Review . . . 18

1.3.1 Hydraulic Jumps in the Environment . . . 19

1.3.2 Hydraulic Jump in Complex Channels . . . 24

1.3.3 Turbulence Modelling and Mixing in the Environment . . . 27

1.4 Gaps in Current Knowledge . . . 33

1.5 Scope & Objectives 35
1.6 Thesis Outline 35

2 Internal Hydraulic Jump in Expanding and Contracting Channels 37
2.1 Introduction 37
2.2 Numerical Modelling 39
2.2.1 Gerris 39
2.2.2 Simulation Setup 41
Topography 41
Initialization and Boundary Conditions 47
Grid Convergence 52
2.3 Verification 55
2.4 Results and Discussion 57
2.4.1 Channel Expansion 61
Set A - Constant Expansion with Variable Inlet Velocity 61
Set B - Constant Expansion with Constant Inlet Velocity 75
Set C - Variable Expansion Rate with Constant Inlet and Sill Velocity . 80
Qualitative Comparison of Expansion Cases 84
2.4.2 Channel Contraction 89
Set D - Constant Contraction with Constant Sill Velocity 89
Set E - Constant Contraction with Variable Sill Velocity 92
Set F - Variable Expansion Rate with Constant Sill Velocity 97
2.5 Conclusion 100

3 2D Internal Hydraulic Jump with Realistic Topography 104
3.1 Introduction 104
3.2 Numerical Modelling 105
3.2.1 Simulation Setup 105

Topography . . . 105
Initialization . . . 107
3.3 Results and Discussion . . . 109
Mixing . . . 109
Wave Speeds . . . 113
3.3.1 Comparisons with 3D simulations . . . 117
3.4 Conclusions . . . 119

4 Conclusion **121**
4.1 Mixing in Complex Domains . . . 121
4.2 Future Work . . . 123
4.2.1 MIT General Circulation Model . . . 124
4.2.2 Simulation Setup . . . 125
4.2.3 Recommendations . . . 129

Bibliography **130**

Curriculum Vitae **138**

List of Figures

1.1 Map of Kitsap Peninsula, situated in the Puget Sound Region in Washington State. Hood Canal is the area of interest with the specific region of interest shown in the exploded view. Data points used for density and velocity were obtained from the South (red) and North (blue) locations [1] 4

1.2 Single layer hydraulic jump in an open channel defined by an upstream supercritical flow and a downstream subcritical flow. 5

1.3 Hydraulic jump in a two-layer flow 11

1.4 Top view of Yasua & Hager [2] experimental setup for hydraulic jump through choked area. 25

2.1 Gerris simulation domain with 12 boxes and 11 connections. Each box is 1 unit high, 1 unit wide and 1 unit long. 40

2.2 Channel cross-sectional profile in the form of a parabolic function, $P(x, y)$ at some position x along the channel 41

2.3 Along channel topography profile at position y = 0.5. Sill forcing the hydraulic jump is shown at x = 6, while second sill to manage boundary conditions is shown at x = 11. 43

2.4 Top view of channel domains showing coastlines for 9 different simulations corresponding with expanding and contracting channels. Colors are paired for mirrored expansion or contraction. Black line indicates straight channel topography. m corresponds to amount of expansion/contraction, q corresponds to rate which is constant for all cases 44

2.5 Top view of channel domains showing coastlines for 8 different simulations corresponding with expanding and contracting channels. Colors are paired for mirrored expansion or contraction. m corresponds to amount of expansion/contraction which is constant for all cases, q corresponds to rate. 45

2.6 3-D isometric surface plot for computational domain maximum expansion case $m = 0.23$ 46

2.7 Cross-sectional areas along the channel which shows the area for each case of m is smallest at the sill, which is needed to force a hydraulic jump to occur. . . 47

2.8 Data slices for along channel (top) xz at a fixed transverse y, along channel xy at a fixed depth z and cross channel yz at a fixed x. 50

2.9 Comparison of levels of grid refinement with density plots showing jump development for data in the center of the channel for the straight channel case, $m = 0$. Coarsest grid is 2^6, while finest grid is 2^8. Topography appears in blue below the red, denser fluid. 53

2.10 Interface height $R(x)$ for refinement levels 2^6, 2^7 and 2^8, in the straight channel case $m = 0$ along the channel centre line. 54

2.11 Instantaneous ρ plots of hydraulic jump along slice $xz5$ (channel center) for non-dimensional time $t = 5$ to $t = 35$ and case $m = 0$ with no cross-sectional variation. Topography appears in blue below the red, denser fluid. 58

2.12 Time averaged density plots (left) between $t = 25$ to $t = 35$ for data in a position across the channel. Outline of topography (right) with domain highlighted in red ($m = 0$). Channel positions are $y = 0.35$ ($xz3$), $y = 0.5$ ($xz5$) and $y = 0.65$ ($xz7$). 59

2.13 **Set A** instantaneous density snapshots of jump development at $t = 12$ and $t = 25$ for expanding channel with variable inlet velocity (left & middle). Corresponding topographies highlighted in red (right) 62

2.14 Transverse channel density comparison for expansion cases $m = [0.1, 0.15, 0.2, 0.23]$ with a constant velocity through the minimum cross-section. Slices $xz3$ to the left of center (left) and $xz5$ center slice (center) and $xz7$ right of center (right). Topography plots for each row (right) highlighted in red. 63

2.15 **Set A** interface height, $R(x)$, for expansion m at transverse channel positions $y = 0.35$, $y = 0.5$ and $y = 0.65$. Topographies corresponding to interface heights (bottom right) where solid lines indicate center of channel and dotted lines indicate off center. 64

2.16 **Set A** time averaged u velocity for increasing rates of expansion at an xy slice z = 0.7 (left). Corresponding topographies highlighted in red (right). Sill velocity constant for each case, with non-dimensional velocity amount (top) indicated with red coloring as supercritical, and blue as sub-critical. 65

2.17 **Set A** along channel average u-velocity for cases $m = [0, 0.1, 0.15, 0.2, 0.23]$ (top-bottom) along the thalweg ($y = 0.5$, $xz5$) and off-center ($y = 0.35, xz3$) (right - left). 67

2.18 **Set A** time averaged vorticity, ω for increasing rates of expansion, $m = [0.1, 0.15, 0.2, 0.23]$ with a constant average velocity across the sill (left). Topography plots with corresponding topography case outlined in red (right). Results are shown across the channel at a depth of 0.3, just above the sill crest. 69

2.19 **Set A** instantaneous thalweg ($y = 0.5$) ρ snapshots (top) over turbulence averaging period for average turbulent ρ (T) (middle), and vertical scalar variance production in jump region (bottom) for expansion case $m = 0.23$ 71

2.20 Simulation **Set A** mixing trend for time average scalar variance quantities from $t = 20$ to $t = 30$ for each component of mixing. Turbulent kinetic energy is also plotted comparing the trend to increasing m. Black line indicates channel center, while red and blue indicate off-center regions. Amount of expansion is increased with increasing m. 73

2.21 **Set B** Interface heights, $R(x)$, for expansion m at transverse channel positions $y = 0.35$ ($xz3$), $y = 0.5$ ($xz5$) and $y = 0.65$ ($xz7$). Plot of corresponding topographies (bottom right) where solid lines indicate channel center interface height, and dotted lines indicate off center. 76

2.22 **Set B** time averaged u velocity for cases $m = [0, 0.1, 0.15, 0.2, 0.23]$ in the along channel direction for data along the thalweg ($y = 0.5$) and off-center ($y = 0.35$) with a constant inlet velocity $U_0 = 0.1$ (right to left). Channel plots for amount of expansion increase from top-bottom. 77

2.23 Simulation **Set B** trend for each componet of mixing (vertical, horizontal, lateral and total) for increase m with a sill velocity that decreases with a larger expansion. Black line indicates center channel mixing, while red and blue indicate off center. 79

2.24 **Set C** interface heights with variable rate of expansion (q) and constant amount of expansion ($m = 0.15$) shown for each case of q. Simulation domain is shown (bottom right) for which the amount solid lines indicate channel center, while dotted lines indicate off-center. 81

2.25 **Set C** along channel average u velocity for a constant $m = 0.15$, with varying rates of expansion, $q = [1.5625, 3.5156, 6.25, 8.2656]$ along the thalweg ($y = 0.5$) and off-center ($y = 0.35$) (right - left). 82

2.26 **Set C** mixing components (vertical, horizontal and lateral) for variable rate of expansion (q) and constant amount of expansion (m). Topography plot indicates different simulation domains (bottom right) with solid black line the center data, and dotted red and blue off center. 83

2.27 Comparison of vorticity, ω for simulation sets A (left), B (middle), C (right) for small m (top row) to large m (bottom row) (for set A and B) or a small to large q for set C. Plots are shown across the channel at a depth of 0.3. 84

2.28 Mode 2 wave speeds, c, for **Set A** simulations along channel slices $xz3$, $xz5$ & $xz7$ (left). Black solid line corresponds to center data, while red and blue dotted lines correspond to off center. Topographies are plotted corresponding to each simulation case highlighted in red (right). 87

2.29 Mode 2 wave speeds, c, for **Set B** simulations along channel slices $xz3$, $xz5$ & $xz7$ (left). Black solid line corresponds to center data, while red and blue dotted lines correspond to off center. Topographies are plotted corresponding to each simulation case highlighted in red (right). 88

2.30 **Set D** interface heights, $R(x)$, for increasing contractions, m, at a constant rate, $q = [1.5625, 3.5156]$ and constant velocity across the sill. Corresponding topographies (bottom right) relate to coloured lines and are plotted for data along the channel center. 90

2.31 **Set D** - Constant contractions with variable inlet velocity mixing trend for all mixing components (Lateral, vertical and horizontal) as well as total mixing and TKE. Data plotted for channel center for increasing amounts of contraction. 91

2.32 **Set E** interface heights, $R(x)$, for increasing contractions, m, at a constant rate, $q = [1.5625, 3.5156, 6.25]$ and variable velocity across the sill. Corresponding topographies (bottom right) relate to coloured lines and are plotted for data along the channel center. 93

2.33 u_{avg} just ahead of hydraulic jump for Set E simulations. Results are plotted for increasing amounts of contraction. Corresponding topographies (top left) show colored lines relating to position of jump and corresponding topographies. . . . 94

2.34 **Set E** - Constant contractions with constant inlet velocity mixing trend for all mixing components (Lateral, vertical and horizontal) as well as total mixing and TKE. Data plotted for channel center for increasing amounts of contraction. 95

2.35 Comparison of vorticity, ω_z, for simulation sets **D, E & F** (left - right) plotted at a depth of 0.3 in the across channel slice. Smallest contraction amount (top row) to largest (bottom row) is shown for each case. 96

2.36 **Set F** interface heights, $R(x)$, for constant amounts of contractions, m, with variable rate, $q = [1.5625, 3.5156, 6.25]$. Corresponding topographies (bottom right) relate to coloured lines and are plotted for data along the channel center. . 98

2.37 **Set F** - Constant contraction amount, m, with variable rate, q, mixing trend for all mixing components (Lateral, vertical and horizontal) as well as total mixing and TKE. Data plotted for channel center for increasing amounts of contraction. 99

3.1 Hood Canal bathymetric data between Washington University [1] density data in the south (red) and north (magenta). Data for the thalweg is plotted and used for polynomial fit. The sill creates a hanging valley towards the relative west ($\diamond$) and occurs in the middle of the maximum cross-sectional area (expansion). The channel has been rotated to run north-south for reference to density profiles. 106

3.2 Polynomial fit to Hood Canal topographic data at deepest part of channel for 2D slice. Thalweg data represented by blue line, while curved fit used for simulation domain boundary represented in orange. 107

3.3 Density profile data for North (flood tide) and South (ebb tide) ends of Hood Canal collected from Washington University [1]. Density and depth is non-dimensional for simulations and fit to a smooth curve. 108

3.4 Velocity profile data for North and South ends of Hood Canal collected from Washington University [1] and obtained through forced simulation data. Average constant velocity used for simulations calculated along black line in center of channel for respective directions. 109

3.5 Flood tide instantaneous u-velocity at $t = 150$ to $t = 250$ (top), time averaged density with isopycnals (middle) and cumulative scalar mixing over the averaging period (bottom) 110

3.6 Ebb tide instantaneous u-velocity at $t = 150$ to $t = 250$ (top), time averaged density with green isopycnals (middle) and cumulative scalar mixing over the averaging period (bottom) 112
3.7 Mode 1 and 2 wave speeds during flood tide, averaged over $t = 150$ to $t = 250$. Plots show along channel min/max wave speeds corresponding to sub or supercritical flow. 114
3.8 Mode 1 and 2 wave speeds during ebb tide, averaged over $t = 150$ to $t = 250$. Plots show along channel min/max wave speeds corresponding to sub or supercritical flow. 116
3.9 Mixing comparisons for §2 and §3 data. 2D mixing intensity for ebb (top left) and flood tide (top right) shown compared to mixing intensity for straight channel case, $m = 0$, in the channel center from chapter 2 118

4.1 Top view of extruded topography profile for Hood Canal MITgcm simulation initial setup. 127
4.2 Top view of extruded topography cut to region around sill with increased grid refinement 128

List of Tables

2.1 Set A simulation parameters 51
2.2 Set B simulation parameters 51
2.3 Set C simulation parameters 51
2.4 Set D simulation parameters 52
2.5 Set E simulation parameters 52
2.6 Set F simulation parameters 52

Chapter 1

Introduction

Understanding the complex nature with which flows in oceans, channels and seas interact with their environment has become of increasing importance as water levels rise, and climate conditions continue to change. Specifically, investigation into the generation of internal tides and how their characteristics affect mixing has been a topic of interest following observations that 30% of tidal dissipation occurs in the open ocean [3]. This dissipation and mixing is often a result of turbulence caused by internal tides, or the flow phenomenon, internal hydraulic jump (Fig. 1.2, page 5) which has been seen in a variety of channels and dense ocean regions [4]. As such, several studies have also examined the existence and investigated the impact hydraulic jumps have in a variety of channel flows. Some of these include the Strait of Gibraltar where mixing driven by the exchange flow impacts the water properties in the Mediterranean [5].

Although these types of flows have been studied for at least 70 years, the topography and water properties vary between regions, making each occurrence unique [6]. For example, the well known hydraulic jump occurring at Knight Inlet is tidally driven, and thus simulations of the region must be transient in nature, however the channel is small enough that the rotation of the earth doesn't seem to have an impact on the flow. Conversely, the Strait of Gibraltar is density driven, rather than tidally, and the size of the channel causes accurate examination to include the Coriolis effect, which differs still from flow in the Pre-Bosphorus which is

considered steady rather than transient [7][5][8]. These details make simulations difficult to generalize, and thus require investigation of flow characteristics specific to each region such as density profiles, topographical makeup, and flow source.

Furthermore, the mixing and energy dissipation which occurs as a result of hydraulic jump is important to quantify. This is because the level of mixing determines the water properties and thus affects biological productivity by changing the distribution of dissolved oxygen [6]. Altering the levels of dissolved oxygen content can have a significant impact on the aquatic environment. For example, Hood Canal, a channel in Washington State, has experienced decades of low dissolved oxygen conditions reaching hypoxic levels. The occurrence of hypoxia, especially in the southern reach, which led to frequent seasonal fish kills in the early 2000s resulted in the formation of the Hood Canal Dissolved Oxygen Program (HCDOP) as a response to understand what is driving the low dissolved oxygen [9]. However, root-cause determination is difficult due to the several factors increasing complexity of the situation. These include climate, inputs of ocean and freshwater, and flow restrictions due to topography characteristics such as a large sill in the North [10][11].

In 2010, Gregg & Pratt investigated the flow and hydraulics near the sill of Hood Canal and found that the density field can resemble an overflow with internal hydraulic control and a hydraulic jump landward seen at flood tide [7]. However, the long wave speeds indicate that the flow remains supercritical through the apparent jump, which suggests the transition from sub-critical to supercritical flow you would expect to see in a hydraulic jump is missing. Therefore, the observational evidence indicates the possible occurrence of an internal hydraulic jump, but more investigation is required. Thus, the motivation for this thesis stems from the need to understand Hood Canals unique characteristics, such as specific density profiles and topography, the public alarm caused from the occurrence of hypoxia related fish kills, and the indication that a hydraulic jump may exist at the sill.

1.1 Hood Canal

Hood Canal is a fjord-like body of water situated at the base of the Olympic Mountains in the Pacific-Northwest. Fisheries and aquaculture are the driving industries of the region which is home to a diverse group of marine life including Oysters, Salmon, Lingcod, and Orcas. These species play a pivotal role in the economic interests of Puget Sound. The canal (shown in Figure 1.1 on page 4) stretches 110 km from the northern tip of the Kit-sap Peninsula to the end of Lynch Cove and sees width variation between 2-4 km along the entire channel. Unique features of the channel include a long sill in the norther section, rising within 50 m of the waters surface, while depths beyond the sill plunge to 175 m. Additionally, the channel is narrow to the south and experiences an expansion around the sill. Furthermore, the variation in depth, combined with the constriction at the Admiralty Inlet in the north causes deep water renewal to be limited [7]. In addition to the topographical characteristics affecting the flow, seasonal upwelling caused by runoff from the glacial melt of the Olympic Mountains occurs in the autumn. The influx of saline water displaces the bottom water beyond the sill, and increases the oxygen content in the south, resulting in strong stratification in the fall. After deep water renewals occur, oxygen content steadily decreases beyond the sill to hypoxic conditions less than 3ml/l. As mentioned above, the seasonal fish kills that occur is linked to the hypoxic conditions occurring in the fall and has raised public alarm due to the impact on fisheries and aquaculture in the region. Newton [9] noted that the levels of dissolved oxygen have been decreasing since the 20^{th} century and as such there has been scientific interest in the region to understand the cause. One theory, is that the topographical and environmental features of Hood Canal complicates the circulation and mixing [12] [7]. As Gregg and Pratt pointed out, mixing could be further complicated by the occurrence of a hydraulic jump beyond the sill. Therefore, gaining a better understanding of how the unique topographic and flow features of Hood Canal affect, or contribute to a hydraulic jump, can be studied through numerical simulations, using bathymetric data available for Hood Canal, and the density profiles for the spring or fall.

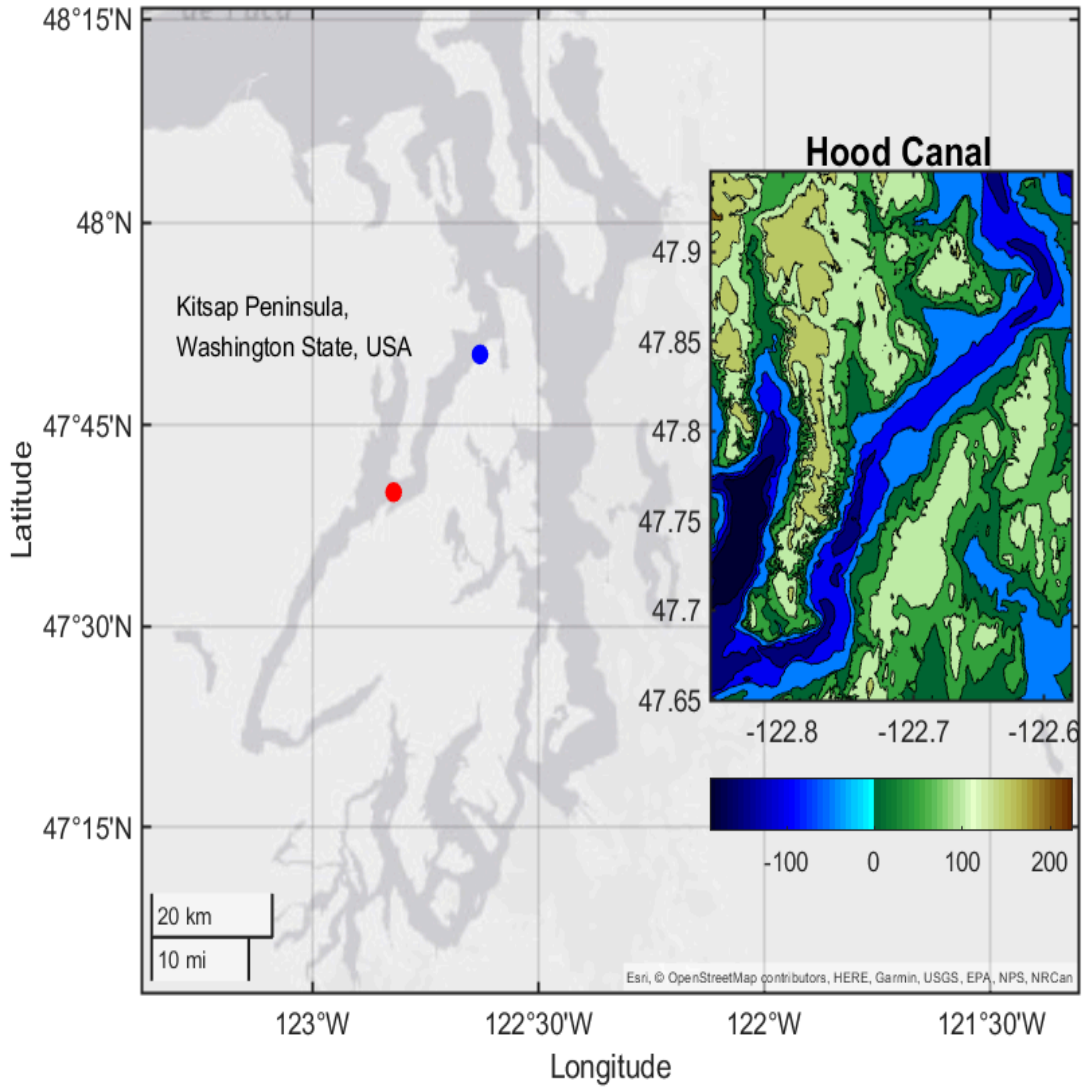

Figure 1.1: Map of Kitsap Peninsula, situated in the Puget Sound Region in Washington State. Hood Canal is the area of interest with the specific region of interest shown in the exploded view. Data points used for density and velocity were obtained from the South (red) and North (blue) locations [1]

1.2 Background and Theory

1.2.1 Hydraulic Jump

A hydraulic jump is a flow phenomenon which commonly occurs in rivers and canals, dam spillways, industrial applications, and dense overflows in the abyssal ocean [13]. While often developing naturally in open channel flows, engineers frequently take advantage of the energy dissipation and mixing that is associated with the turbulence generated by the jump, often utilized in a variety of flow control applications. This phenomenon arises when a supercritical flow regime suddenly and abruptly transitions to a subcritical region, for example, a fast moving layer of water impinging on a standing pool in an open channel (Fig. 1.2), or a small disturbance in topography causing the upper surface to transition. Generally, the fluid considered is water

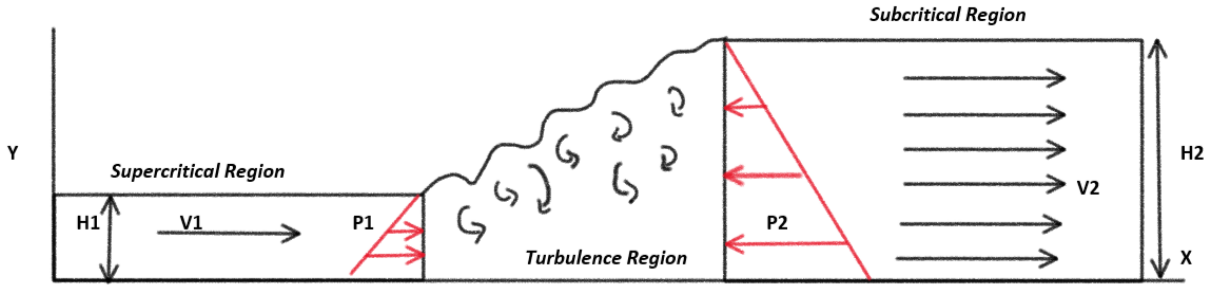

Figure 1.2: Single layer hydraulic jump in an open channel defined by an upstream supercritical flow and a downstream subcritical flow.

and the condition of the flow is described by the **Froude number**, a dimensionless number defined as the ratio of channel velocity to the propagation speed of a small-disturbance wave [14]. The Froude Number is

$$\mathrm{F_r} = \frac{\mathbf{v}}{c} \tag{1.1}$$

where $\mathbf{v} = Q/A$ is the average cross-sectional velocity and c is the speed at which the wave is transmitted through the medium. If A is the cross-sectional area of the channel and H is the depth, then $\partial A/\partial H = c = \left[gA/\left(\partial A/\partial H\right)\right]^{\frac{1}{2}}$ [15].

Subcritical flows occur when $\mathrm{F_r} < 1$, in which the flow velocity is much smaller than the

wave speed and waves can propagate both upstream and downstream, while supercritical flow occurs for $F_r > 1$, a high speed flow compared to wave speed propagation, for which waves can only propagate downstream. Thus, this transition between criticality causes a shock, or hydraulic jump to occur.

Additionally, due to the abrupt nature with which the transition occurs, a number of interesting characteristics are often associated with hydraulic jumps. These include:

- Highly turbulent flow through the transition region shown in Fig. 1.2
- Two phase flow due to air-entrainment
- Energy dissipation as a result of turbulence production
- Wave development downstream of the jump

Turbulence production occurs as a result of conservation of mass and momentum constraining the supercritical flow to abruptly dissipate in order to match downstream conditions. Thus, the local turbulence production associated with the transition between flow regimes results in significant energy dissipation in the form of mixing between fluids. Furthermore, this conversion is accompanied by large scale vortex formations in the roller (recirculation region) and advective transport caused by the formation of entrained air bubbles in the mixing layer.

While hydraulic jumps can occur in both the atmosphere or in stratified overflows in the ocean (internal hydraulic jump), the classical jump shown above is analyzed under conditions for single-layer flows, an idealization that doesn't actually occur in nature. To investigate single-layer hydraulic jumps, an idealized setup is considered. An open prismatic channel with a constant cross-sectional area and fixed depth is considered, and the fluid is homogenous with frictionless boundaries.

Continuity and momentum are applied to develop an expression for the head loss across the jump. Using a control volume analysis to balance inlet and outlet transport, and assuming flow

into and out of the control volume are steady, x-momentum reduces to,

$$\frac{1}{2}\rho g b {H_1}^2 + \rho Q V_1 = \frac{1}{2}\rho g b {H_2}^2 + \rho Q V_2 \tag{1.2}$$

Additionally, depth, H, is small compared to the length of the channel, therefore the pressure distribution is considered hydrostatic away from the jump region [15], while wall friction is neglected and the velocity distribution is uniform. Applying these assumptions and dividing Eq.(1.2) by $2/\rho g b {H_1}^2$ provides the equation for the ratio of sequent depths,

$$\frac{H_2}{H_1} = \frac{1}{2}\left[\left(1 + 8{\mathrm{F_{r1}}^2}\right)^{\frac{1}{2}} - 1\right] \tag{1.3}$$

from which the jump height can be determined for upstream conditions. For relatively large Froude numbers where $\mathrm{F_{r1}} = Q/\left(g b^2 {h_1}^3\right)^{\frac{1}{2}} > 2$, Eq. (1.3) is approximated as,

$$\frac{H_2}{H_1} = \sqrt{2}\mathrm{F_{r1}} - \frac{1}{2}. \tag{1.4}$$

As shown in Fig. 1.2, the x-momentum balances the forces of hydrostatic pressure in Eq. (1.3) due to fluid depth with inlet and outlet momentum flow rates. The pressure terms act inward on either side of the control volume and are of equal specific gravity (ρg) multiplied by $\frac{H_1}{2}, \frac{H_2}{2}$ on each side, and by the height the pressure acts over per side (H_1, H_2). Finally, once height differences are resolved, jump efficiency and thus energy loss is expressed as $\eta^* = \left[1 - \frac{\sqrt{2}}{\mathrm{F_{r1}}}\right]^2$.

Eq. (1.3) yields 3 unique solutions: (1) Inlet depth is equal to outlet depth, in which case no jump has occurred. (2) A negative liquid level which is not physical and can be eliminated and (3) an abrupt increase in depth which we call a hydraulic jump.

While the above equations have been extremely useful in the development of theory surrounding hydraulic jumps [13], and provide estimations of energy loss across the jump due to turbulence, they are highly idealized and specified to the classical jump condtions. These con-

ditions are often not applicable to flows that are seen in nature, such as internal jumps, jumps in complex channels, or jumps occuring in the atmosphere, in which environmental conditions drastically complicate the physics.

For example, in flows combining stratification and flow-topography interactions due to strong barotropic and baroclinic currents forced by tides and density exchanges, typically seen in fjord entrances with sills, complexity is exceedingly increased. For one, observations in these exchanges indicates both local energy loss and internal tide generation are important in Froude numbers ranging from small values [16] to those close to and above one [17]. For a stratified fluid, Fr can be found for an infinite number of internal wave modes, wherein the first wave mode is the fastest, and thus has the lowest Froude number. Therefore, a more relevent Froude number applied to two layer flow is the composite Froude number [18]; for a two-layer flow, this is defined as

$$G^2 = {F_1}^2 + {F_2}^2, \tag{1.5}$$

for which, $G^2 < 1$ is subcritical and $G^2 > 1$ is supercritical.

Here, complexity is significantly increased by changing a few of the flow conditions. Namely, in the scope of internal hydraulic jumps occuring in oceans and brackish channels, the main interest is the complexity added by flow-topography interactions and density stratification. Additionally, the above equations fail to quantify the mixing which can result from the turbulent region of the flow. Some two-layer theories have been proposed to address some of these complications, which will be the focus of subsequent sections.

1.2.2 Boussinesq & Incompressible Approximation

Environmental flows such as those in deep channels or in the open ocean typically exhibit a thermocline depending on the season, latitude and turbulent wind mixing on the surface. In colder climates, such as Hood Canal, this can lead to stratification as discussed. Due to the non-isothermal nature of the flow, density variations exist and must be accounted for in the Navier

Stokes Equations. For viscous 3-dimensional flows, problems become extremely complex and computationally expensive. To deal with this problem a popular method is to apply the Boussinesq approximation which is accurate when density variations are small thus reducing the nonlinearity of the problem increasing the likeliness of convergence to be achieved.

Therefore, for open channel flows the general compressible Navier-Stokes equations, Eq. (1.6) and continuity, Eq. (1.10) are solved together.

$$\frac{\partial(\rho\mathbf{u})}{\partial t} + \mathbf{u}\cdot\nabla(\rho\mathbf{u}) = -\nabla p + \nabla\cdot(\mu\left(\nabla\mathbf{u} + (\nabla\mathbf{u})^T\right) - \frac{2}{3}\mu(\nabla\cdot\mathbf{u})\mathbf{I}) + \rho\mathbf{g} \tag{1.6}$$

$$\frac{1}{\rho}\frac{D\rho}{Dt} + \nabla\cdot\mathbf{u} = 0 \tag{1.7}$$

where $\mathbf{u}$ is the fluid velocity, p is the pressure, ρ is the density μ is the dynamic viscosity, $\mathbf{I}$ is the identity matrix, and $\mathbf{g}$ is acceleration due to gravity. Then the Boussinesq approximation is applied, which assumes the density variations are negligible in the inertial terms, but gravity is sufficiently strong and therefore the specific weights between the two fluids is appreciably different. Thus, the density variation is only important in the buoyancy term, ρg and is neglected elsewhere. Eq (1.6) is then simplified to,

$$\rho_0\left(\frac{\partial\mathbf{u}}{\partial t} + \mathbf{u}\cdot\nabla\mathbf{u}\right) = -\nabla p + \nabla\cdot(\mu\left(\nabla\mathbf{u} + (\nabla\mathbf{u})^T\right) - \frac{2}{3}\mu(\nabla\cdot\mathbf{u})\mathbf{I}) + \rho\mathbf{g} \tag{1.8}$$

where density, ρ is replaced by ρ_0 everywhere but the buoyancy force term. Additionally, since the magnitude of density fluctuations with respect to the velocity gradients is small

$$\frac{\mathrm{D}\rho}{\mathrm{D}t} \ll \rho\nabla\cdot\mathbf{u} \tag{1.9}$$

so that velocity terms are leading order and the continuity equation is simplified to the incompressible form,

$$\nabla\cdot\mathbf{u} \approx 0. \tag{1.10}$$

This further simplifies equation Eq. (1.8) as $\nabla \cdot \mathbf{u} \approx 0$ reduces $-2/3\mu(\nabla \cdot \mathbf{u})\mathbf{I}$ to zero. Since viscosity, μ can also be considered constant the diffusion term $\nabla \cdot (\mu(\nabla \mathbf{u} + (\nabla \mathbf{u})^T))$ is rewritten as $\mu \nabla^2 \mathbf{u}$.

Finally, from the energy equation,

$$\frac{\mathrm{D}T}{\mathrm{D}t} = \kappa \nabla^2 T, \tag{1.11}$$

the buoyancy term ρg is written as $(\rho_0 + \Delta\rho)\mathbf{g}$ where $\Delta\rho = \rho - \rho_0$. Since the density variations only have a dependency on temperature then ρ can be simplified to

$$\rho = \rho_0 - \kappa\rho_0 (T - T_0) \tag{1.12}$$

where κ is the coefficient of thermal expansion. Thus yielding,

$$\frac{\mathrm{D}\rho}{\mathrm{D}t} = \kappa \nabla^2 \rho \tag{1.13}$$

which makes use of the energy equation to calculate density, while maintaining the continuity equation.

Therefore the final form of the Navier-Stokes equations are with hydrostatic and Boussinesq approximations are simplified to

$$\frac{\partial \mathbf{u}}{\partial t} + \mathbf{u} \cdot \nabla \mathbf{u} = -\frac{1}{\rho_0} \nabla p' + \nu \nabla^2 \mathbf{u} + g' \mathbf{k} \tag{1.14}$$

where p' is the pressure variation due to hydrostatic pressure, and $g' = \frac{g(\rho - \rho_0)}{\rho_0}$ is the reduced gravity as a product of the Boussinesq flow.

These equations are applied to Boussinesq flows common in atmospheric fronts, oceanic circulation and katabatic winds, where density variations are essentially negligible other than in terms multiplied by gravity. This is extremely useful for reducing computing time by drasti-

cally simplifying the Navier stokes equations, and will be used in the simulations in this paper. It is important to note that the Boussinesq approximation is making a contradictory statement that density fluctuations are negligible, but body force is due to density variation, however this has been shown to be an acceptable approximation in environmental flows where density is temperature and salt driven [19].

The next section discusses the two-layer theories, used in conjunction with Boussinesq approximations to solve two-layer flow problems.

1.2.3 Internal Hydraulic Jump in Two-Layer Flows

Hydraulic jumps that occur in dense ocean overflows arise from density differences as well as tidal interactions with topography. Accounting for these density differences adds to the complexity of quantifying parameters associated with hydraulic jumps. While stratified flow can have many layers of differing densities, approximating the flow as having two layers provides insight into the dynamics with a relatively simple model. As such, a few two-layer theories have been developed and are the focus of the set of problems discussed here.

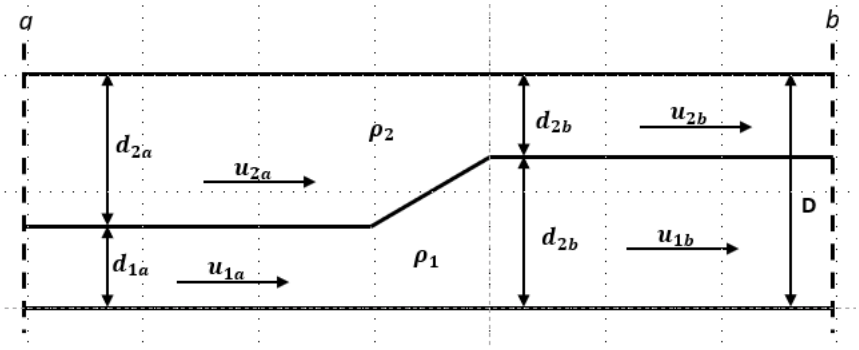

Figure 1.3: Hydraulic jump in a two-layer flow

Fig. 1.3 shows the domain for resolving internal hydraulic jumps between differing densities. These internal shocks in two-layer fluids are effectively a transition between two steady flow states of immiscible fluids with uniform velocities and distinct densities. Waves may propagate on the interface between layers, but the barotropic flows free surface undulations are approximated as pressure variation on the upper bound where the amplitude of the disturbance

is related to δp between layers. The amplitude at the free surface, where δp is large, is much smaller than the amplitude of the disturbance at the interface where δp is small, thus free surface undulations are neglected, and upper and lower boundaries assumed horizontal. Theories dealing with these flows are termed two-layer. While a jump does actually occur at the surface, it is small compared to the internal jump height and it is approximated by the pressure at the rigid lid. This assumption is also applied in the CFD solver Gerris [20] used in the first part of this work, while MITgcm [21], used in §4 calculates the surface height as part of the numerical solution. Furthermore, these theories are two-dimensional, and neglect entrainment and mixing between layers, and thus are highly simplified; however they can be used to estimate the size of a hydraulic jump between two-layer flows. Theories are developed with 3 initial assumptions:

1. The jump is steady in a reference frame moving with it,

2. Mixing between layers is neglected,

3. A rigid lid is imposed on the upper and lower boundaries

As shown in 1.3, the flow has an upper and lower density, ρ_1, ρ_2 where, $\rho_2 < \rho_1$. Additionally, the rigid lid condition sets a uniform depth, D, and the jump is regarded as a turbulent structure with a supercritical upstream state with known upstream conditions, $u_{1a}, u_{2a}, d_{1a}, d_{2a}, \rho_1, \rho_2$ and unknown downstream conditions, $u_{1b}, u_{2b}, d_{1b}, d_{2b}$, which may be sub or supercritical. Therefore, with the assumption flows are steady moving with the jump, the total depth of the domain and volume flow rate of each layer are constant:

$$\begin{aligned} D &= d_{1a} + d_{2a} = d_{1b} + d_{2b}, \\ Q_1 &= (u_{1d})_a = (u_{1d})_b\,, \quad Q_2 = (u_{1d})_a = (u_{1d})_b\,, \\ Q &= Q_1 + Q_2, \\ Q &= d_{1a}u_{1a} + d_{2a}u_{2a} = \text{const.} \end{aligned} \tag{1.15}$$

Therefore, momentum flux is,

$$M = \int_0^D p + \rho u^2 \, \mathrm{d}z = \text{constant}. \tag{1.16}$$

Yih & Guha [22] made the first attempt with additional assumptions that (a) interfacial stresses are negligible, (b) surface pressure, p, varies linearly with upper layer thickness, d_2 and (c) the flow is hydrostatic away from the jump. They proposed a two-layer model in which they argue that if the fluids are assumed immiscible then by conserving mass in each layer, but momentum globally an equation describing the bores' propagation could be described. In a reference frame moving with the bore, momentum flux was described as,

$$\begin{aligned} M &= p_a D + \frac{1}{2}\Delta\rho g d_{1a}^2 + \rho_1 {u_{1a}}^2 d_{1a} + \rho_2 u_{2a}^2 d_{2a} + \frac{1}{2}\rho_2 g D^2 \\ &= p_b D + \frac{1}{2}\Delta\rho g d_{1b}^2 + \rho_1 u_1 b^2 d_{1b} + \rho_2 u_2 b^2 d_{2b} + \frac{1}{2}\rho_2 g D^2. \end{aligned} \tag{1.17}$$

Combining Eq. (1.17) with mass conservation in the Boussinesq limit revealed more information is needed to describe the bore speed. The momentum flux introduces the variable $p_a - p_b$, and thus an additional expression is needed to relate the pressure drop along the top of the channel to the upstream and downstream conditions.

Chu & Baddour [23] and Wood & Simpson [24] conducted dye streak experiments, with observations suggesting that over the jumps short distance, the energy loss in the contracting layer is (likely) an order of magnitude less than the expanding layer. They imposed the additional assumption that energy loss in the contracting layer is small. Therefore, assuming energy is conserved across a bore in the contracting layer and applying the Bernoulli equation with no head loss along a streamline in the upper layer an equation for front bore velocity is given as,

$$U_{ws} = \left[\frac{g' h_f \left(h_f + d_{1a}\right)\left(\mathrm{D} - h_f\right)^2}{\mathrm{D}\left(h_f^2 - 3 d_{1a} h_f + 2 d_{1a}\mathrm{D}\right)} \right]^{\frac{1}{2}} \tag{1.18}$$

where from Fig. (1.3), D is the channel height, h_f is the bore height, and d_{1a} is the thickness of

the lower layer ahead of the bore. Eq. (1.18) is conventionally referred to as the WS model.

Conversely, in the turn of the century Klemp, Rotunno & Shamarock[25] proposed the opposite assumption to that of Wood & Simpson, instead deriving a model with a better fit to updated experimental data. Conserving energy in the lower layer and applying the Bernoulli equation to the related streamline, they developed an equation for frontal bore speed known as the KRS model,

$$U_{KRS} = \left[\frac{g' h_f^2 \left(2\mathrm{D} - d_{1a} - h_f\right)\left(\mathrm{D} - h_f\right)}{\mathrm{D}\left(h_f^2 + \mathrm{D}\left(h_f + d_{1a}\right) - 3 d_{1a} h_f\right)} \right]^{\frac{1}{2}}. \tag{1.19}$$

Borden, Meiburg & Constantinescu [26] compared WS and KRS models to experimental results conducted by Wood & Simpson [24] and showed for non-dimensional front velocity plotted as a function of $\mathrm{R} = h_f/d_{1a}$, the KRS model is a better fit, but moderately overpredicts the bore velocity.

In terms of energy dissipation, these models have a few problems. Yih & Guha [22] solution shows that there is a net gain in energy flux in the contracting layer across the jump [27], which is a non-physical occurrence. Furthermore, the other models have an absence of energy loss in both layers which can not be correct. Thus, Borden Meiburg & Constantinescu also carried out a numerical study, in the Boussinesq limit which showed that mixing at the interface could cause a gain in potential energy in the expanding layer [26]. This motivated the most recent model developed by Borden & Meiburg [28] to solve the problem of unknown surface pressure change across the jump. Using the Boussinesq approximation, under non-hydrostatic, two-dimensional conditions, they proposed a method in which energy conservation assumption is not relevant, but rather vorticity flux of the frontal bore is considered in addition to mass and momentum equations.

This model uses the 2D vorticity equation for Boussinesq flows,

$$\mathbf{u} \cdot \nabla \omega = -g' \frac{\partial \rho^*}{\partial x} + \nu \nabla^2 \omega \tag{1.20}$$

for a plane flow and dimensionless density. With a control volume defined around the bore, the

pressure term disappearing as a result of the Boussinesq approximation, and in- and outflow normal to the control-volume boundaries with vorticity generated away from the walls, Eq. (1.20) is integrated to find bore speed. The resulting balance yields,

$$\frac{1}{2}\left(U_2^2 - U_1^2\right) = g'\left(h_f - d_{1a}\right) \tag{1.21}$$

which no longer contains a pressure term and therefore does not require a fourth equation. Combining conservation of mass and momentum with Eq. (1.21) provides the expression for frontal bore speed without making any assumptions about where energy is conserved. While numerical simulations showed that the above vortex sheet model is more accurate at predicting vorticity flux just ahead of the bore, the KRS model still produced a more accurate prediction of bore speed [28].

These theories, however, still do not consider mixing or upstream shear. Ogden & Helfrich [29] compared the above two-layer shock joining theories to numerical solutions of the Navier-Stokes equations. They found that none of the two-layer theories reliably predicted the relation between jump height and speed. Additionally, the numerical simulations showed different qualitative jump types occur including, undular bores, smooth-front jumps and overturning turbulent jumps. Finally, they found that mixing does increase with upstream shear.

Therefore, while the two-layer theories described are an improvement on the idealized free surface jump equations, and show some accurate predictions of bore speed, they still fail to solve the full Navier-Stokes equations. Additionally, hydraulic jumps occurring in nature are typically more complex due to interactions with topography, and multiple densities. Furthermore, as Ogden & Helfrich showed, upstream shear is important in quantifying the mixing, therefore justifying the need for numerical simulations to the full Navier-Stokes equations.

1.2.4 Stratified Flow Over Topography

The previous sections demonstrate the differences between the physics of ideal single-layer straight channel flows, to two-layer straight channel flows, and how the complexity of the solutions change. These solutions, however are still trivial compared to the realistic conditions in nature. Fluids flowing over obstacles is a ubiquitous consequence of flows in the environment. The impact of density driven flow-topography interactions can be seen in many examples in nature including undular bores such as the Morning Glory in Australia and Oklahoma [29], or internal hydraulic control as flow plunges over sills in deep basins such as that seen in Knight inlet [4]. The effect of these interactions often can result in hydraulic jumps and gravity currents occurring. Furthermore, a common feature of these environmental flows is stratification due to temperature variance and brackish water.

Density-stratified flow exists in fluids where density varies with position within the fluid. Typically, density variation in the ocean and coastal waters is stable with nearly horizontal isopycnals represented as 'layers' of density increasing as depth increases and unstable stratification will quickly adjust to become stable. The density can be continuous, as commonly seen in the atmosphere and ocean, or concentrated in discontinuous interfaces seen at the surface of the ocean. While variations are small, they can have a dominant effect on the flow if small buoyancy forces are given enough time to act. The simplest form of these types of flows exist in topographically forced homogeneously layered fluids with a free surface, often applicable to flows in rivers or channels. Additional complexity is added with more layers of distinct density fluids, such as exchange flows, or for flows where the full 3D topography effects become relevant, such as those where cross waves occur [4] or rotation is relevant [30].

The general governing equations used to describe stratified fluid motion over topography are

$$\frac{\mathrm{D}\mathbf{u}}{\mathrm{D}t} = -g\hat{\mathbf{z}} - \frac{1}{\rho}\nabla p + \nu\nabla^2\mathbf{u} \tag{1.22}$$

$$\frac{1}{\rho}\frac{\mathrm{D}\rho}{\mathrm{D}t} + \nabla\cdot\mathbf{u} = 0 \tag{1.23}$$

in which fluid velocity is $\mathbf{u} = (u, v, w)$, ρ is density, p is pressure and ν is the kinematic viscosity. In most cases (but not all [29]) viscous effects between layers are assumed to be small and are thus neglected. Additionally, most solutions are treated as incompressible as the density of each parcel of fluid remains constant as it moves in space, regardless of any pressure variations, therefore Eq. (1.23) is reduced to the incompressible continuity equation,

$$\nabla \cdot \mathbf{u} = 0. \tag{1.24}$$

Furthermore, buoyancy frequency N is used to characterize continuously stratified fluids, where N is the frequency of the unforced small amplitude vertical oscillations and characterizes the stratification. For incompressible fluids at rest

$$N^2 = -\frac{g}{\rho}\frac{\mathrm{d}\rho}{\mathrm{d}z}. \tag{1.25}$$

This leads to the hydrostatic equilibrium approximation which is an important assumption used in analytical and numerical simulations, essentially considering these frequencies as motions about a basic state in hydrostatic equilibrium. Therefore, density and pressure fields are expressed as

$$p = p_0(z) + p'(x, y, z, t) \qquad \rho = \rho_0 + \rho'(x, y, z, t). \tag{1.26}$$

Additionally, the hydrostatic approximation is often imposed to simplify the vertical velocity component and increase numerical simulation speed. Since vertical accelerations in the global ocean are typically small compared due to gravitational acceleration, then the vertical momentum is deemed essentially hydrostatic [31]

$$\frac{\mathrm{d}p_0}{\mathrm{d}z} = -\rho_0 g. \tag{1.27}$$

However, mixing in regions of hydraulic jump is dominated by vertical accelerations, and therefore a non-hydrostatic model is used for simulations. Furthermore, since jumps typically

occur far away from bottom topography, some instances can impose free slip boundaries while still accounting for viscous stresses between interfacial layers. These assumptions, including the Boussinesq approximation discussed in §1.2.2 and the free slip boundaries are applied to the simulations conducted in this work.

1.3 Literature Review

Hydraulic jumps have been studied for close to two centuries, although the first detailed considerations date back to 16th century drawings by Leonardo Da Vinci. These alluded to the recognition of large scale eddies and abrupt expansions in river outflows [32] and showed characteristics consistent with jumps studied today. The first physical models were developed by Bidone [33], who conducted many discharge tests and was able to link the upstream and downstream height interfaces to the velocities of meeting flows, however experimental and analytical results were not agreeable as Bidone did not account for the head loss of the flow. A decade later, Jean Baptiste Belanger noted that Bidone's experimental and analytical results did not agree and applied the momentum-conservation principles under idealized conditions which led to the development of Eq. (1.3).

Later, work by Riegel & Beebe expanded on the straight channel flow investigating how stilling basins with angled topography, cross-sectional expansion angles and bottom obstructions impacted energy dissipation [34]. Rouse emphasized the importance of the Froude number in characterizing the hydraulic jump as well as the turbulence characteristics seen across the flow, which gave a greater understanding of the energy transformations happening within the jump. Both the Froude number and turbulence statistics have become important quantities to determine hydraulic jump occurence and effects.

More recently, stationary internal shocks and gravity waves have been of interest to oceanographers and meteorologists, and hydraulic investigation into the effects of energy dissipation and turbulence characteristics across the interface began to grow [35][36]. While two-layer

theories have been developed to deal with some stratified flows (§ 1.2.3), numerical modelling has been useful in obtaining turbulence statistics and resolving fully three-dimensional flow fields.

However, while experimental and analytical studies have been conducted [22][2] [37][38][28], the complexity and non-linearity that can arise from stratification, channel variation, turbulence, entrainment, mixing, and recirculation leaves many problems unresolved. Additionally, the complexity which arises in real flows presents unique problems that need to be solved. Therefore, calibrating numerical modelling with datasets obtained from the extensive experimental literature presents useful opportunity to study hydraulic jump characteristics in real world flows.

1.3.1 Hydraulic Jumps in the Environment

Stratified flows over topography variations in the deep ocean have been of particular interest in many oceanographic studies because these flows may play an important role in determining water properties due to the complex dynamics that arise moderating exchange between oceans and estuaries [39][30][4]. The focus of many of these studies have been to determine the hydraulic control around the topography, and if any turbulent mixing or recirculation occurs. Observational data exist for locations in the abyssal ocean, and in narrow exchange, or tidally driven channels around the world [38] [3] [4].

Polzin *et al.* [38] studied the intense mixing in the bottom water of the Antarctic Ocean and whether significant mixing occurs at the bathymetric constrictions for the deep ocean circulation. Using the Conductivity-Temperature-Depth (CTD) instrument, which estimates the oceans temperature and salinity variations with depth, and the high-resolution profiler, they were able to obtain horizontal velocity estimates and turbulent temperature gradient information. Data showed three localized regions characterized by abrupt descent of isotherms. These corresponded with topographical features including a horizontal constriction, followed by a sill immediately downstream of the constriction and a sharp increase in bottom depth. Ad-

ditionally, velocity profile data supports the theory that dramatic changes in the flow can be inferred from sloping isotherms and energy conservation laws, in which the bottom water accelerates downstream of the sill where potential energy is exchanged for kinetic energy along the channel, which is characterized by the occurrence of internal hydraulic jumps. Furthermore, energetic, turbulent velocity fluctuations were observed downstream of the sill and maximum dissipation rates in excess of 10^{-6} W/kg were observed. These features of a highly stratified flow obstructed by a constriction which empties into a deep basin past a sill being accompanied by intense turbulence and mixing beyond the sill is just one example of the outcomes internal hydraulic jumps can have on re-circulation in the ocean.

Other research by St. Laurent [40] looked at internal wave propagation data of the Mid-Atlantic Ridge in the subtropical North Atlantic. They surveyed the rift valley of the Lucky Strike, a region with dense overflows past a sill. Data was collected with the CTD and deep microstructure profiler. Velocity data indicated Froude numbers with an increase in values near the sill and an abrupt decrease downstream. This suggests hydraulic jump may occur downstream of the sill. Measurements of turbulent dissipation rates upstream of the sill are generally below 10^{-8} W/kg while downstream levels reach nearly 10^{-6} W/kg, indicating strong mixing.

Additionally, channel flows more closely related to Hood Canal have also been investigated which explicitly show the existence of a hydraulic jump [41][30][42][4]. Farmer and Armi's analysis focussed on the internal hydraulics of the Strait of Gibraltar and the jumps influence on the exchange of the Mediterranean waters [41]. Observational data was collected of profiles along the east-west axis using CTD and acoustic Doppler current profiling. Results described in 2D showed maximal exchange (subcritical flow bounded by supercritical flow at either end of the Strait [43]) did occur but with subtleties not incorporated into the theoretical developments presented in previous work. Additionally, they found a distinct jump occurring past the Camarinal Sill, with internal bores propagating to the Tarifa Narrows, a contraction to the east. Finally, mixing was shown to occur in the lee of the hydraulic jump, but the propagating

internal bore was determined not to be a significant factor.

Conversely, Klymak and Gregg argue that field data used for studying internal hydraulic jumps over a sill is typically assumed as two-dimensional (e.g Knight Inlet [42], Strait of Gilbraltar [41]) but that the flow instead is significantly three-dimensional [4]. Using acoustic profiles and data obtained with CTD instrumentation at Knight Inlet, they found strong recirculations containing substantial vortices and strong three-dimensional flow, as well as indication of a possible 3D hydraulic jump, not previously documented in nature. Flood tide data was divided into four layers: a thin stratified layer at the top, spreading intermediate layers 2 and 3, and a plunging dense layer, which is more complicated than the typical two-layer assumption uses in analytical models. Results showed several ways observations differ from simple two-dimensional channel flow approximations. These include the thinning of layer 3 landward of the sill crest, layer 2 reversing direction landward of the sill, and all water below 20-m depth flowing against tide at 0.1 m/s not expected as may be seen in two-dimensional flow. Additionally, ebb tide showed significant cross channel flow. Volume and energy budgets were calculated to quantify recirculation and amount of energy dissipation in the lee of the sill and showed that the sources of intermediate water that is the focus of Farmer and Armi [44] is probably lateral entrainment. Furthermore, formation of a wedge-like layer, as well as a lack of hydraulic jumps on the along channel line where recirculation is high indicates the flow is strongly three-dimensional and thus they postulate there is a three-dimensional hydraulic jump occurring. This is significant in regards to running numerical simulations, as two-dimensional analysis may not be sufficient.

Hood Canal, on the other hand, lacks explicit observational evidence of a hydraulic jump [7], but comparisons to Knight Inlet can provide some insight as the volume of literature is larger for the latter [44][4][45][17][46][47][48] . Knight Inlet is similar to Hood Canal, as the flow is tidally driven, fed by glacial melt in the spring and fall, and has a jump occurring over a sill which is dependent on the season and phase of the tide. Observations show that isopycnals plunge down over the sill and then jump toward the surface in a hydraulic jump. Gregg and

Pratt also investigated turbulent energy dissipation, finding that about one-third of the total energy lost from the barotropic tide was a result of radiating internal waves [7], thus indicating the important role played by wave propagation and mixing in the lee of the sill. Furthermore, the flow was also found to be highly three dimensional, with indication that the hydraulic jump occurring is three-dimensional in space, beginning from the lee of the sill and curving in space, accounting for some of the dissipation in energy budgets. Applying this to Hood Canal, it is evident that quantification of turbulent mixing as well as generating a well resolved three-dimensional simulation is important for understanding the complex characteristics of the flow.

Furthermore, numerical simulations of these regions have also been conducted to address some of the controversy surrounding the two-dimensional interpretation. Sachez-Garrido *et al.* [30] used MIT general circulation model to solve the non-linear, non-hydrostatic Navier stokes equations for a Boussinesq flow. Two-way exchange was obtained by lateral forcing through the imposition of mean baroclinic velocities extracted from intermediate resolution models done through nested simulations. Moderate tidal forcing showed that hydraulic jumps existed at the Camarinal Sill, in confirmation with observational data, however jumps developed from parallel isopycnals were distinctly different demonstrating that spatial variation is relevant. Likewise, Afanasyev & Peltier [48] carried out simulations on an ideal domain based on similar geometry and flow conditions of Knight Inlet. Their goal was to study high-resolution numerical simulations to show that the main source of mixing is the breaking of internal waves in two-dimensions. The Boussinesq approximation was used to filter sound waves and remove the impact of background variation of density on internal wave amplitude, and a rigid lid condition was imposed. To model similar conditions to Knight Inlet, topography was modelled by a piece-wise linear approximation while upstream velocity profiles were specified as a harmonic function with a tidal period of 7 h. These were chosen as a good fit for local tidal oscillations of Knight Inlet data parameters. Afanasyev & Peltier's results generated two conclusions: (1) Upon analysis of total volume in the turbulent region around the formed

jump it was shown to increase only during the initial phase of the flow evolution. After wave breaking occurred and the subsequent quasi-steady hydraulic-like flow was established, volume changes were only subject to oscillations caused from episodic wave activity. Since volume is conserved, the local thickening that occurred requires the layer become narrower upstream, in which a flow adjustment would take place only if steady flow is established. Thus, the most important mechanism for the intermediate layer creation is the wave breaking inducing mixing. (2) The simple two-layer hydraulic flow approximation over an obstacle does not provide a straightforward procedure where hydraulic analysis is applicable for realistic flows. While the model employed by Afanasyev & Peltier is an ideal case of Knight Inlet, the continuous density stratification complicates the two-layer approximation and loses the benefit in simplicity as many layers are needed to be applied. Thus, they argue that simple 2D approximations cannot be applied to Knight Inlet, and further numerical studies of the potential 3D affects should be investigated. Therefore, it can be concluded there is a need for more numerical simulations more closely matching the realistic characteristics of some of these complex channel flows.

Gregg & Pratt [7] collected bathymetric and observational data in the sill region of Hood Canal in the spring and fall between 2001 to 2003. Data was collected along the thalweg using the Shallow Water Integrated Mapping System, a depth-cycling towed body measuring one tidal period of a nominal 12.5 h from slack to ebb tide. Complex geometry, time dependence and a lack of distinct interfaces hindered a complete description of the hydraulic properties of the canal. Therefore, using the Taylor-Goldstein equation, criticality was assessed section by section, accounting for width variation and nonuniform vertical variations in velocity and stratification. Flood tide saw the density field resemble an overflow with internal hydraulic control and an apparent hydraulic jump landward of the sill. Wave speeds, however, were typically above zero and indicated that the flow remains largely supercritical through the jump, which suggests these disturbances could be cross waves, but they could also be transients caused by changing tides. Another peculiarity is the region upstream of the flow is not subcritical, as it would be in standard overflows, but has stretches of supercritical flow. This could indicate that

the flow is in a supercritical state over the sill, in which case the region downstream can experience a transition from supercritical with a deep lower layer to another supercritical state with a shallow lower layer. However, density observations do not fit this scenario. Ebb tide also sees flow of both subcritical and supercritical nature around the sill, with a trapped dome of dense water that could be associated with a recirculating roller seen in hydraulic jumps. What is clear is that there are indicators of features familiar to a hydraulic jump, and the transitions between subcritical and supercritical are common in the canal, but the complexity of the topography, and the transient nature vastly complicate observational assessments. Thus, numerical modelling of Hood Canal in a more idealized sense should contain some geometric complexity.

Finally, Gregg & Özsoy [8] studied the exchange flow seen in the Bosphorus. They investigated the accuracy of hydraulic theories compared to observational data, and found poor agreement. Sharp bends throughout the strait, a contraction in the South that is not coincident with the minimum cross-section, and widening toward the North were found to strongly affect the flow dynamics. Furthermore, they found intense mixing occurring downstream of the contraction as a result of a hydraulic jump occurring past a sill in the North. The conclusion was that the complexity of the channel geometry affects the flow such that hydraulic theory cannot correctly predict wave-speeds. However, the existence of the hydraulic jump does indicate that the theory holds for some part of the channel. This is an important realization, as it gives further motivation to study the expanding region around the sill at Hood Canal. If a jump is occurring there, the hydraulic control theories may not be able to accurately predict some flow features, and thus numerical investigation is needed, as Gregg & Pratt pointed out.

1.3.2 Hydraulic Jump in Complex Channels

Environmental flows rarely fit the ideal conditions assumed in the two-layer theories, as rivers and channels typically have cross-section variation. This is clear in many of the previously discussed flows; Hood Canal is dominated by widening near the sill which leads to a channel area maximum [7], Knight inlet is abruptly constricted and 3-dimensional [4], and the exchange

in the Strait of Gibraltar is clearly affected by the contraction at the Tariff Narrows [30]. While complexity in channel geometry is evident, the effect this variation has on the occurrence and characteristics of the internal shocks has not been thoroughly investigated.

Most of the literature covering complex topography focuses on experimental analysis of a variation of the single-layer jumps with different rates of abrupt contractions or expansion. Yasuda & Hager [2] investigated the flow features of hydraulic jumps forming in an asymmetric linearly contracting channel (Fig. 1.4).

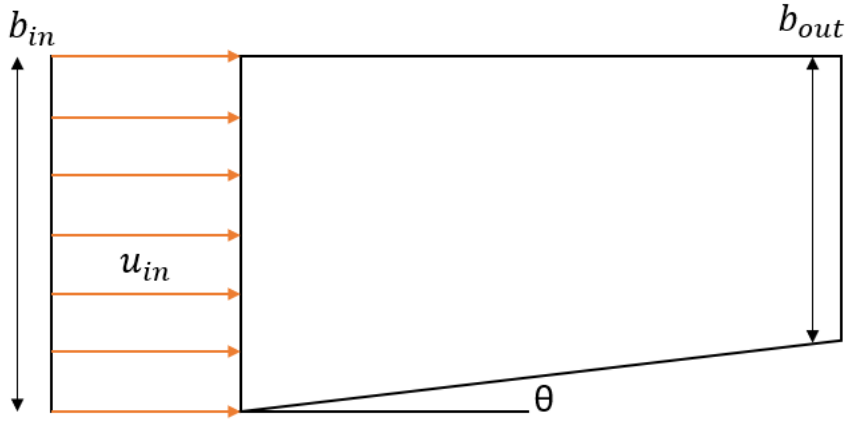

Figure 1.4: Top view of Yasua & Hager [2] experimental setup for hydraulic jump through choked area.

While they did not investigate any of the turbulence features of the jump, energy loss across the jump was computed. They found that sequent depth ratio between the ideal single-layer, straight channel jump and the choked jump were very similar and depended on the upstream froude number, however jump structures in the contraction differed significantly from the classical jumps as shown from profiles along the deflected sidewall. Additionally, they found that energy loss across the jump decreased in the contracting case. A similar study conducted by Hassanpour *et al.* [49] obtained experimental results for the pressure fluctuations in a spatial hydraulic jump with varying expansion ratios. Experiments were run using a stilling basin with upstream width $b_1 = [0.5, 0.4, 0.3, 0.2]$ and a constant downstream width of $b_2 = 0.5$, allowing for gradual symmetric increases in angle of expansion. Results indicated that pressure near the

toe in the spatial jumps is larger than those observed in classical free surface jumps due to the gradually expanding walls decreasing the sequent depth ratio. Additionally, the data showed that larger expansion ratios were accompanied by an increase in the intensity of turbulent fluctuations on the free surface, causing the difference in pressure fluctuation patterns. However, results are obtained for a homogenous fluid, with no abrupt changes in topography and only give an idea of what may occur in stratified flow over topography changes within an expansion. This is an interesting result, as compared to Yasuda and Hager, where jump structures between expansions and contractions seem to be unique.

Winters and Seim [50] numerically investigated simulations of exchange flow through idealized contracting channels. They relaxed several of the simplifying assumptions used in two-layer theories as their particular focus was on the effects and consequences of mixing and dissipation due to the channel. Motivation for increasing the complexity was generated from Bray, Ochoa & Kinder [51] observing exchange flow in the Strait of Gilbraltar having a thick interfacial layer with variable properties resulting in vertical exchange of mixing between upper and lower layers. Numerical solutions were obtained for non-hydrostatic flow of a continously stratified fluid in three dimensions. The numerical results were examined in comparison to two-layer theory with a focus on the effects of mixing and dissipation. Using the equations of motion for an incompressible, density stratified fluid under the Boussinesq approximation and a variable-width channel with vertical, free-slip walls and a stress free rigid lid approximation consistent with the Boussinesq approximation. The simulations are initialized with a lock-exchange where fluids of slightly different densities fill either end of the channel and are separated by a gradual transition region centered at the narrow part of the contraction. Comparing the results with Armi and Farmer two layer maximal exchange solutions showed that the addition of interfacial friction didn't fundamentally change the maximal exchange solutions. However, much more of the flow was shown to be subcritical than predicted. Additionally, Froude numbers were small than predicted, and friction acted to shift the throat control downstream. Simulations in the work presented here will instead investigate expanding regions in

one direction, more relevent to tidally driven flows.

Castro *et al*. [52] conducted numerical simulations of stratified flows in channels with irregular geometry. Simulations were run considering the real geometry of the Strait of Gibraltar by extracting breadth data from bathymetric measurements. Both lock exchange and tidal forcing initial conditions were conducted and semidurnal and diurnal tidal waves were simulated. They observed good agreement between simulations results and experimental data and achieved development of internal bores travelling westward and eastward as seen in Gibraltar. Finally, the numerical results they obtained revealed fluctuations in interfacial levels and moving control points for different stages of the tide. The numerical techniques that were used are similar to those that will be used in this paper, and show an additional level of detail that may not be obtained from experimental data. However, the work presented in this paper investigates idealized geometry with the objective of identifying the fundamental influence of channel width variations in order to apply results generally to other locations, rather than a very realistic simulation for a specific region.

1.3.3 Turbulence Modelling and Mixing in the Environment

Turbulence is a three-dimensional, time-dependent, nonlinear phenomenon commonly observed in fast flowing rivers, breaking waves, and most fluid flows occurring in nature. Important flow characteristics include unsteady large and small scale vortices and large amounts of kinetic energy. In the ocean, turbulence induced transfer of momentum, heat, and other water properties are commonly controlled by waves, both internal and free surface, while small-scale turbulent diffusion in the abyssal ocean is shown to affect the overall thermohaline circulation [53]. Furthermore, dispersion of pollutants and mixing of microorganisms affects growth and vitality of marine life and aquaculture. This has stimulated research into turbulent mixing in channels and oceans, quantification of mixing rates, and the efficiency of energy transfer from tidal forcing to small-scale turbulent mixing [48] [54] [55] [56].

Additionally, several studies have shown the role that tide-topography interactions have

on tidally generated mixing influenced by ocean topography such as steep ridges [57] [58] or continental slopes [59]. These studies show that internal waves are generated from the tidal energy interaction with the complex boundaries and propagate away from topography and mix locally at the topography. Thus, the role turbulence initiated from tidally forced hydraulic jumps has in local mixing needs to be further understood.

However, most of the current literature ([37][31][25] [60][24][22]) concentrates on two-dimensional internal hydraulic jumps which ignore mixing and turbulent entrainment. This leaves many open questions regarding the nature and structure of internal shocks forming in the environment.

Challenges in modelling turbulence and mixing in the environment arises from topographical complexity, density stratification, and intense current fields that can rapidly change horizontally and vertically. Specifically, vertical mixing is an important process driving global overturning circulation, nutrient redistribution for fisheries and transport of heat and salt. In the deeper ocean, internal tides and flow interaction with topography and over sills dominate contributions to vertical mixing; [61], while 1 TW (half of the estimated 2 TW of mixing energy required to maintain the large-scale thermohaline circulation of the ocean) of tidal mixing has been attributed to internal tides generated by the barotropic interaction with topography [62] [3]. What makes these problems so complex is the dynamics of the vertical mixing processes of interest occur on smaller scales than can be provided by mesoscale numerical models offering spatial information between 1-10 m in the vertical, which is typical for the large scale simulations required for ocean flows. Some closure schemes have been proposed, although Durski [54] showed they can produce significantly different solutions in coastal regions as compared to the deep ocean. Therefore, since flows in regions such as Hood Canal, which are characterized by density stratification and irreversible fluxes of tracers, are often on the weaker end of the turbulent state [63] applying the turbulence closures typically used for large scale oceanographic problems may not be entirely useful.

Mixing in the environment can be described as the irreversible homogenization of a scalar,

relying on the molecular diffusion of a scalar substance such as heat or salt. This diffusion, for statistically homogenous turbulent flows occurs on scales close to the Batchelor scale, $L_B = L_k/\sqrt{Pr}$, where $L_k = \left(\frac{\nu^3}{\epsilon}\right)^{\frac{1}{4}}$ is the Komogorov scale and Pr is the Prandtl number. For typical open ocean conditions where the dissipation rate of kinetic energy is between $\epsilon = 10^{-10} - 10^{-6} m^2 s^{-3}$ [38][40] Batchelor scales are on the order of mm. These scales are far less than the typical vertical scales previously mentioned, and as such make small-scale resolutions difficult, if not impossible. Therefore, the general approach for resolving mixing in the sub-grid region for ocean flows is to model turbulent motions through turbulent diffusivity defined as the averaged scalar flux [64]. Therefore, the general objective for estimating mixing in canals with stratification and weaker turbulence is to measure vertical turbulent scalar flux.

Direct measurements of vertical velocity and scalar concentration can be extremely difficult to obtain as internal waves can induce reversible contributions to the scalar flux [64] which can be difficult to remove. Additionally, due to spatially localized patches of turbulent mixing, ship based sampling of dissipation rates can become unreliable. Consequently, almost all microstructure turbulence measurements in the ocean use indirect methods to infer values of K_ρ (turbulent eddy coefficient for mass, a process by which substances are mixed in the ocean) from a scalar turbulent quantity such as the temperature variance dissipation rate using the mode proposed by Osborn [65] based on the turbulent kinetic energy equation,

$$-\frac{1}{2}\frac{\partial \overline{u_i'^2}}{\partial t} - \frac{1}{2}\overline{u}_j\frac{\partial \overline{u_i'^2}}{\partial x_j} - \overline{u_i'u_j'}\frac{\partial \overline{u_i}}{\partial x_j} - \frac{\partial}{\partial x_j}\left(\overline{\frac{1}{2}u_j'u_i'u_i'} + \frac{1}{\overline{\rho}}\overline{u_j'p'} + \nu\overline{u_i'\frac{\partial u_i'}{\partial x_j}}\right) = \epsilon + \mathrm{b} \tag{1.28}$$

which, if length scales are small, unsteadiness can be neglected and Eq.1.28 can be reduced to a balance between local shear production, buoyancy and dissipation.

$$-\overline{u_i'u_j'}\frac{\partial \overline{u_i}}{\partial x_j} = \epsilon + \mathrm{b} \tag{1.29}$$

For a smooth front turbulent jump with moderate shear, the mixing can be quantified from the

cumulative integral of buoyancy flux,

$$b = \int_0^x \int_0^D \overline{w'b'} \mathrm{dzdx} \tag{1.30}$$

and shear production [29],

$$\int_0^x \int_0^D -\overline{u_i' u_j'} \frac{\partial \overline{u_i}}{\partial x_j} \mathrm{dzdx} \tag{1.31}$$

.

Additionally, the second commonly used indirect method to quantify mixing is finding the cumulative integral of the scalar variance production through the region of mixing, for which internal waves occur across the jump. Temporal change in scalar variance is governed by

$$\frac{\partial \overline{\theta'^2}}{\partial t} + \overline{u}_j \frac{\overline{\theta'^2}}{\partial x_j} + 2\overline{u_j' \theta} \frac{\partial \overline{\theta}}{\partial x_j} - \frac{\partial}{\partial x_j} \left(\overline{u_j' \theta'^2} + \kappa \frac{\partial \overline{\theta'^2}}{\partial x_j} \right) = -2\kappa \overline{\left(\frac{\partial \theta'}{\partial x_j} \right)^2}, \tag{1.32}$$

where θ represents a scalar in the flow. In a steady flow without flux of density across boundaries, the amount of mixing between water masses with different densities, represented y T, is $\overline{u_j T} \frac{\partial \overline{T}}{\partial x_j}$.

Continued advancements in computational power have aided in studying turbulence; however, despite a relatively large number of experimental studies on internal hydraulic jumps, numerical investigations are still moderately limited. The three main classes of modelling for many large scale turbulent flows for environmental fluid mechanics (EFM) are Direct Numerical Simulation (DNS), Large Eddy Simulation (LES) and Reynolds-Averaged Navier-Stokes (RANS), as well as constant or defined functions or diffusivity are often used for large scale environmental flows. DNS is capable of solving the exact Navier-Stokes equations down to the smallest length and time scales, however for many EFM applications, with Reynolds numbers from 10^4 to 10^9 and mixing occurring on the mm scale, this resolution is largely impractical due to the computational cost. As a result, approximate forms of the NS equations are solved instead, in which some physical modelling is required to reduce the complexity of the domain.

Large Eddy Simulations filter the NS equations to resolve only eddies that are larger than the filter size. In implicit LES, small scale turbulence is modelled by the numerical error. Since the numerical dissipation associated with high-order non-oscillatory finite volume Gudonov schemes has similar behaviour on small scales to that of a sub-grid scale model no explicit sub-grid model is applied. Instead, ILES modelling has shown comparable solutions to DNS for passive scalar mixing [66] and stratified flows [29][67][68][69], and will be applied for the majority of simulations in this work. Finally, RANS solutions are modelled as eddy-viscosity or first order models and second order closures. RANS is time-averaged and most or all the of the turbulence scales are modelled by a turbulence model [70].

While application and interpretation of CFD simulation results for turbulence problems are known to be highly sensitive to a range of computational parameters, this is especially true for models of environmental flows. Since typical industrial applications often occur in closed systems with pre-defined boundary conditions and well known system properties, results validation can be easier to obtain. For environmental problems, there is uncertainty in almost every aspect of the modelling process and because boundary conditions, flow characteristics, driving forces, and interactions are difficult to fully quantify due to the scales of the problem, some practical guidelines for validation have been established [70]. Best practices for modelling environmental flows include clear definition of modelling purpose, scope and resources, basis for modelling selection and parameter choices, model sensitivity testing, and comparison to observational data and other numerical study techniques. This is the approach taken in this work, and it is beneficial to look at some existing literature discussing numerical hydraulic jumps and complex topography Simulations in the environment both and how mixing and turbulence is quantified.

Soontiens and Allen [71] investigated the sensitivity of a high resolution regional ocean model to several choices in turbulence closure schemes. They modelled sensitivity to mixing and advection in the Juan de Fuca Strait-Strait of Georgia sill-basin estuarian system, located near Hood Canal in Puget sound. With similar exposure to the Salish Sea, and regional tem-

peratures, turbulence comparisons can also be applicable to Hood Canal. The model equations integrate the Reynolds averaged Navier-Stokes equations under the Boussinesq and hydrostatic approximations, in which $k - \epsilon$ and $k - \omega$ vertical turbulent closure equations are compared. They found no significant differences in deep or intermediate salinity between either closure case and that the model was relatively insensitive to several mixing choices.

Furthermore, net impact of mixing in a specified region of some river outflows and canals depends on not only intensity of the turbulence, ϵ and density gradients available, but also spatially on the active mixing area, and duration. This puts an emphasis on the importance of hydraulic control and spatial variation on mixing which can be seen across hydraulic jumps. As such some numerical studies have been conducted to determine the importance internal hydraulic jumps may be as a mechanism for locally generated mixing over steep topography.

Legg and Klymak [56] carried out a series of numerical simulations of tidally driven flow over an isolated ridge to explore contributing factors to overturning and mixing. The numerical study is motivated by the inability of theoretical models to examine regimes with finite-amplitude barotropic forcing or energy partitioning between local mixing and radiated internal tides. They found that large steepness and large amplitude flow enhances the strength of overturning internal bores for a tidally driven flow. Thus, one mechanism for mixing is the tidal flow interaction with topography, at topic that will be studied in §3 of this work. They due note there are a number of other mechanisms for generating mixing including shear instability, wave-wave interactions and sub-harmonic instabilities. Additionally, since simulations were run in 2D a number of important turbulence generating instabilities are omitted, and thus they do not attempt to quantify the mixing, but rather qualify the impact the topography has on the mixing, which is shown to be relevant.

Furthermore, Legg and Adcroft [72] showed that nonhydrostatic modelling is preferred as highly non-linear internal bores are poorly represented by hydrostatic models. They modelled a series of 2D simulations of internal wave breaks over concave and convex continental shelfs using the Massachusetts Institute of Technology General Circulation Model (MITgcm). The

results showed that contrasting with analytical predictions, no reduction in mixing is found for one type of slope compared to another, which differed compared to the analytical results due to the non-linearity of the numerical calculations. Additionally, they found that any mixing was associated with reflected waves off of the slope, until a quasi-steady state was reached, at which point cancellation of reflected waves around a concave critical point might occur. While this is simulated for different bottom topographies, this cancellation could be apparent in concave channel expansions as will be simulated in this work.

What is evident from the above numerical simulations is; the ability to alter solutions parameters and model turbulence features can yield better results than the current analytical models, and are able to give results for mixing occurring as related to topography changes. However what both of the above studies outline is the need for 3D simulations to more effectively model the complexity of the turbulence occurring in the channels.

1.4 Gaps in Current Knowledge

Hydraulic jumps have been of interest to scientists for centuries; however, many questions still remain. The previous sections provide justification for the work presented in this thesis and highlight the current gaps in the literature. This includes: motivation for hydraulic jumps in the environment [9][4][5][8] and Hood Canal [7], gaps in current analytical theories [29][8], lack of complex channel studies, and justification for turbulence and mixing quantification [61]. These questions are not fully addressed in the current literature and will be investigated in this work.

1. **What is the motivation for internal hydraulic jump in Hood Canal?** Outlined in the §1.1, depleting oxygen concentrations [9] and seasonal fish kills cause concern associated with hypoxia in Hood Canal motivated studies by Gregg & Pratt [7]. Observations indicate a hydraulic jump may exist past a sill, but due to the complexity of the channel (expansion around a sill) further study is needed to better characterize the flow parame-

ters. Furthermore, definitive reason for the hypoxic conditions has yet to be established, but due to the turbulence and mixing associated with hydraulic jumps and the effect that can have on micronutrient redistribution, quantifying how mixing is affected by the complexity in realistic channels is needed.

2. **Why is a numerical simulation required?** Described in §1.2.3 and §1.3.1 the present two-layer theories fail to include mixing and spatial variation in their assumptions. What's evident from Knight Inlet [4] and Bosphorus [8] is channel geometry plays an important role, and may affect the jump conditions, however it is not clear how. Some studies investigating the effects of spatially varying topography exist, but they are mostly experimental and are not directly applicable to the environment as conditions cannot be as easily controlled as in numerical analysis. Additionally, there appears to be few studies looking at how varying rates of expansion or contraction affect the flow, although Gregg & Özsoy [8] showed this to be important. Furthermore, there appears to be no studies addressing a hydraulic jump occurring in an expansion coincident with a sill. While §1.3.3 shows the challenge associated with simulating turbulent flows in the environment, steps have been taken to further improve these results, and good estimations can be obtained. Therefore, due to the question around the accuracy of two-layer theories applied to environmental flows, and the indication that three-dimensional effects matter, the best that can be offered for these flows is numerical simulations.

3. **What is the best way to model turbulence in environmental flows?** Choosing the appropriate turbulence modelling is important for environmental flows as validation is difficult to achieve. Gerris, the numerical code used here, uses LES to model turbulence and allows modelling of complex topographies; it has been shown to be successful in modelling the turbulence in the type of flows studied here [6][67]. Therefore, Gerris is used to model idealized cases, however, for more realistic simulations, tools such as MITgcm, which parameterized a range of more realistic components in the flow may be

useful as well. This future research is briefly introduced in the final chapter.

Hydraulic jumps are a complex phenomenon that are still undergoing extensive research experimentally, analytically, and numerically. Furthermore, there is clear indication that internal shocks are occurring in the environment and are of importance in some regard. However, evidence shows that approaches going forward should consider the complexity of the geometry, whether it be an expanding or contracting channel, complex bathymetry, spatial variance or the fully resolved 3D domain.

1.5 Scope & Objectives

The scope of this thesis is confined to flow features modelled after, or similar to Hood Canal. Furthermore, rotation and boundary layer theory is not considered, as the only interest is the role varying channel geometry has on the jump characteristics and associated mixing. Therefore, the objectives of this thesis are:

- Quantify channel expansion and contraction impact by comparing mixing and wave-speed quantities and qualitatively investigate the effect a changing cross-section has on hydraulic jumps
- Investigate 2D flow over complex topography modelled after Hood Canal and compare wave-speeds to Gregg & Pratt [7]. Determine relative amount of mixing between ebb and flood tide.

1.6 Thesis Outline

In §2 an idealized model emulating a sill coincident with an expansion or contraction, motivated by the topography in Hood Canal, will be simulated for various amounts of expansion and contraction cases. In addition, a fixed maximum expansion will be chosen, with varying rates of expansion (that is, the slope approaching the maximum expansion is increased). These

cases will be compared qualitatively to observe differences that might appear between expanding and contracting channels, and quantitatively via investigating changes of scalar variance production as a determination of mixing to identify the effect of channel width variation on mixing, if any.

§3 will consider a more realistic topography, derived from bathymetric data available for Hood Canal. Flow will be simulated for ebb and flood tide, and density and velocity values will be derived from Hood Canal data. These simulations will investigate how a more realistic bottom profile affects hydraulic jump and wave speeds in 2D. Additionally, mixing rates and wave-speeds will be calculated, and wave speeds will be compared to the observational data provided by Gregg & Pratt [7] for flood and ebb tide.

Finally, the future work discussed in §4 has set up the simulation for a realistic full topography for Hood Canal from available data and is discussed in detail as an effort to stimulate further work. The discussion in this section involves modelling the simulation domain after available data, discussion of benefits & drawbacks of the tools used and discussion of a future direction to take the existing work.

Chapter 2

Internal Hydraulic Jump in Expanding and Contracting Channels

2.1 Introduction

Investigation of hydraulic jumps forming from continuously stratified flow forced over topography in channels and passages has mostly been approximated as two-layered and two-dimensional [29][28][55] with some studies looking at three-dimensional effects [67]. These internal jumps are much more complex than those occurring in surface flows because mixing between density layers, vertical velocity profiles, and tidal forcing all play important roles in characterizing these flows. Additionally, many channels in nature often exhibit drastic variations in cross channel geometry, increasing the complexity of the dynamics. Knight inlet, which has been investigated extensively, has been shown to be a largely 3D flow [4] with evidence suggesting a three-dimensional hydraulic jump is occurring. Furthermore, the channel meanders, with a mix of expansions and contractions defining the bounds. Likewise, Hood Canal has also shown evidence of a hydraulic jump, occurring with geometry around the sill equivalent to a significant expansion followed by a moderate contraction [7]. The influence of the channel width variations has yet to be thoroughly investigated. Building on work from

Ganotaki and Ogden [73], which briefly considered channel contractions coincident with a sill and following similar but idealized channel characteristics to that of Hood Canal, this chapter will investigate the effect of channel width variation. Specifically, the impact of varying rates of expansion and contraction coincident with a sill on the mixing and structure of internal hydraulic jumps will be determined.

This chapter will investigate sets of idealized simulations for non-rotating internal hydraulic jumps over a sill for (1) constant rates of expansion/contractions for varying max/min channel width and, (2) varying rates of expansion/contraction for a set of max/min channel width. Furthermore, since cases of constant rates of expansion/contraction vary in cross-sectional area at the sill, the sill velocity is different in each case if the volume flow rate is constant. In order isolate the effect of the geometry changes from the effect of the upstream velocity, which has previously been shown to affect the jump size and mixing [29], a set of simulations with a constant average velocity at the sill is also conducted for topographies in (1). The objectives of this chapter are:

- Investigate qualitative differences in flow structure for topographies with different expansions/contractions.
- Quantify mixing through the hydraulic jump to determine how mixing varies spatially under channel expansion and contraction for channels with constant rates of expansion (Fig. 2.4).
- Compare mixing for expansion/contraction of constant sill velocity or variable sill velocity
- Quantify mixing for variable rates (Fig. 2.5) of expansion with a fixed maximum width to show how approach angle effects mixing rates.

2.2 Numerical Modelling

2.2.1 Gerris

Finding numerical solutions to time-dependent turbulent, stratified, large scale environmental problems can be constrained by a maximum time-step value due to a finite speed of sound wave propagation. As such, considering the fluid as strictly incompressible creates an elliptic problem on the pressure, expressed as instantaneous propagation throughout the entire solution space. This fundamentally changes the problem from spatially explicit, to spatially implicit. The simulations studied in this paper therefore model the non-hydrostatic, incompressible Navier Stokes equations with the Boussinesq approximation and reduced gravity applied (Eq. 1.14, Eq. 1.13, & Eq. 1.23). To solve this type of problem, Gerris uses a combination of quad/octree discretization, multilevel Poisson solver, and projection method to solve this class of elliptic problems. Advection terms are discretized using a second-order upwind finite volume scheme while complex solid boundaries are approximated using cut cells. This greatly simplifies complex boundaries which are usually represented through structured and unstructured curvilinear grids. The geometry and grid generation are designed for environmental flows which typically have an approximatly flat surface, and depths defined by a varying bottom boundary. Due to the complex topography defining Hood Canal, Gerris is a useful solver in this case [20].

Simulations are conducted with implict large-eddy simulation (ILES), which is computationally more affordable than direct numerical simulations, yield comparable results [74], and thus are more useful for environmental flows that occur on a large scale. Since the finite volume approach treats nonlinear advection terms as non-oscillatory, the sub-grid stresses are of the same form as the viscous stress tensor. The numerical error then becomes the sub-grid scale turbulence scheme which conserves mass and momentum while dissipating energy at the grid-scale. This approach has been shown to produce comparable results to a DNS simulation for a gravity current [75][66], which has similar dynamics to the flows studied here.

Cases of 3D idealized simulations in contracting and expanding channels are investigated in this chapter using the Gerris open source code. The domain is spatially discretized using cartesian (or cubic) finite volumes organized hierarchically as octree in 3D. Each cell has a direct neighbour in six directions. Handling of embedded solid boundaries is done with mixed cells cut by the solid boundary and imposes three constraints to simplify calculations at the boundaries,

1. levels of direct neighbour cells cannot differ by more than one

2. levels of diagonally neighbouring cells can not differ by more than one

3. all the cells directly neighbouring a mixed cell must be at the same level

These constraints simplify the gradient and flux calculations. Constraint (3) is the most restrictive, forcing the whole solid boundary to have the same resolution interior. Vertical resolution is 2^7 for both the 2D and 3D flows presented. The domain is specified using 12 rectangular boxes in a row as shown in Figure 2.1, and the problem is non-dimensinoalized by the maximum depth in the flow so that the non-dimensional box height is one. The left side of the left most box is the inlet of the channel, while the right side of the right most box is the outlet, and the sides of the other boxes between allow the fluid to flow freely from one box to the next along the channel. The topography defines the bottom and sides of the channel, and the top of the boxes represent the free surface.

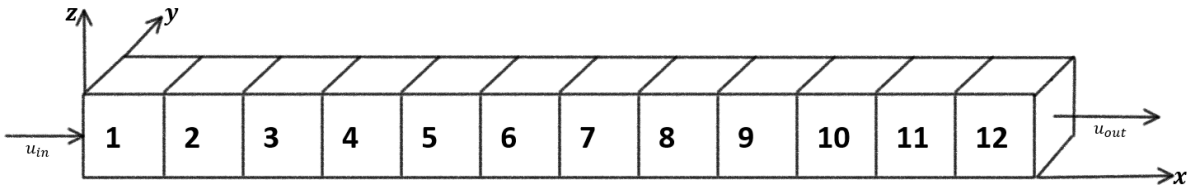

Figure 2.1: Gerris simulation domain with 12 boxes and 11 connections. Each box is 1 unit high, 1 unit wide and 1 unit long.

2.2.2 Simulation Setup

Topography

The topography is modelled after a generalized set of geometric features relating to those existing in Hood Canal. That is, a lateral expansion occurring coincident with a sill. Forced stratified flow over the sill will cause a hydraulic jump to occur downstream of the sill, which is similar to what is occurring in Hood Canal [7]. Comparing quantitative and qualitative results of the impact of the expanding region allows the effect of channel width variations to be identified. Previous work by Ogden and Ganotaki [73] on contracting channel topography is also used as reference for some cases.

In a domain where z is channel depth, y is channel width, and x is the along channel direction, a general topography function is developed. The channel cross-section is defined by the function $z(x, y)$; for a given $x = x_0$, $z(x_0, y)$ is parabolic as shown in Figure 2.2. The width and height of the parabola vary with x to form the sill and expansion.

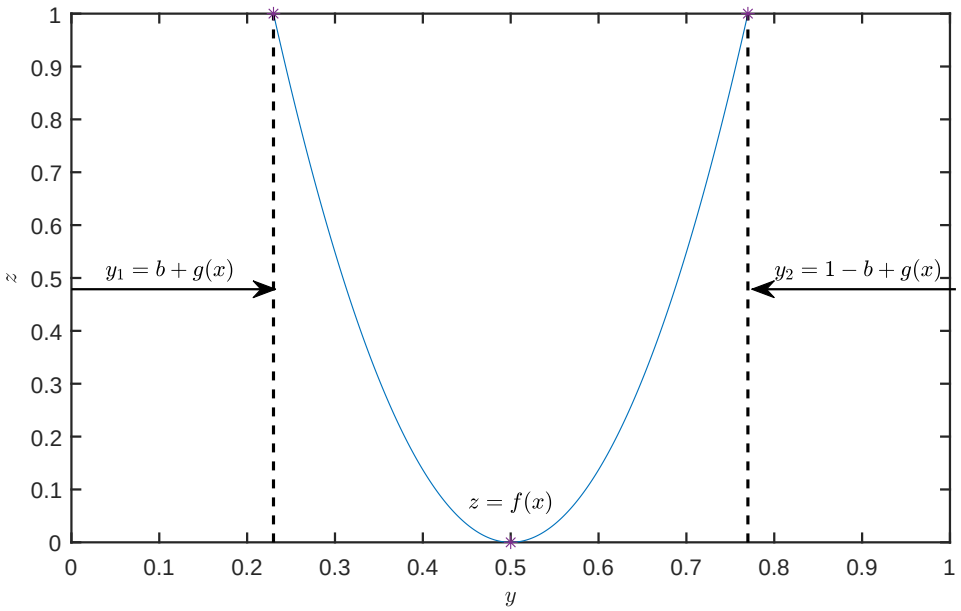

Figure 2.2: Channel cross-sectional profile in the form of a parabolic function, $P(x, y)$ at some position x along the channel

The expansion or contraction is symmetric about $y = 0.5$ and thus a parabolic function of

the form,

$$z(x, y) = a(y - 0.5)^2 + c \tag{2.1}$$

describes the cross-section. Parameter c is defined by the thalweg, the deepest part of the channel, chosen to have a Gaussian sill to elicit smooth transition between regions. Therefore, along the thalweg ($y = 0.5, z = f(x)$),

$$\begin{aligned} z(x, y = 0.5) = f(x) &= a(0.5 - 0.5)^2 + c \\ c &= f(x). \end{aligned} \tag{2.2}$$

Furthermore, the expansion or contraction is defined by choosing the position of the symmetric coastline occurring at $y_1 = b + g(x)$ and $y_2 = 1 - b + g(x)$ where $g(x)$ is also a Gaussian function that gives the corresponding expansion or contraction. Therefore,

$$\begin{aligned} z(x, y_1 = 1 - b + g(x)) = 1 &= a(1 - b + g(x) - 0.5)^2 + f(x) \\ a &= \frac{1 - f(x)}{(0.5 - b + g(x))^2} \end{aligned} \tag{2.3}$$

This yields the general topography function describing both the sill $f(x)$ and the coastline $g(x)$, given as,

$$z(x, y) = \frac{(1 - f(x))\,(y - 0.5)^2}{(0.5 - b + g(x))^2} + f(x) \tag{2.4}$$

where $f(x) = h_1 e^{-(x - \frac{L_x}{2})^2}$ and $g(x) = m e^{-\frac{(x - \frac{L_x}{2})^2}{q}}$.

For the sill function, $f(x)$, the peak is controlled by $h_1 = 0.65$, and was chosen as a comparable sill height-to-depth ratio to that at Hood Canal [7]. Additionally, the term $L_x/2$ represents the location in the x-direction of the sill peak. With $L_x = 12$, and 12 boxes, the sill peaks at the channel center. After running test simulations with Eq. (2.4), it was found that the outlet condition resulted in waves reflecting off the outlet into the domain toward the jump region. Therefore a second sill was added downstream to transition the flow to supercritical and isolate the outlet from the rest of the domain, shown in Fig. (2.3).

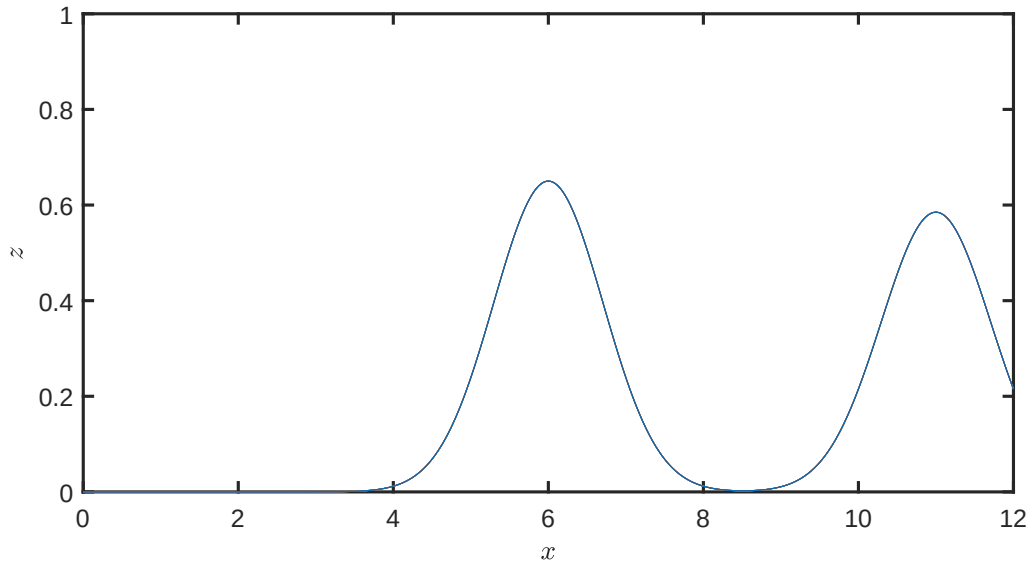

Figure 2.3: Along channel topography profile at position y = 0.5. Sill forcing the hydraulic jump is shown at x = 6, while second sill to manage boundary conditions is shown at x = 11.

Likewise, the coastline, $g(x)$, has a peak value controlled by m (the distance from lines $y_1 = b$ and $y_2 = 1 - b$) for which $+m$ corresponds to an expansion and $-m$ to a contraction and a *rate of expansion/contraction* controlled by q. For cases with a constant rate of expansion/contraction (Fig. (2.4)) the maximum slope of the coastline remains constant for all cases, where q varies with respect to m, while cases with variable expansion/contraction rates (Fig. 2.5)) see a constant m value and varying q, and thus varying coastline slopes.

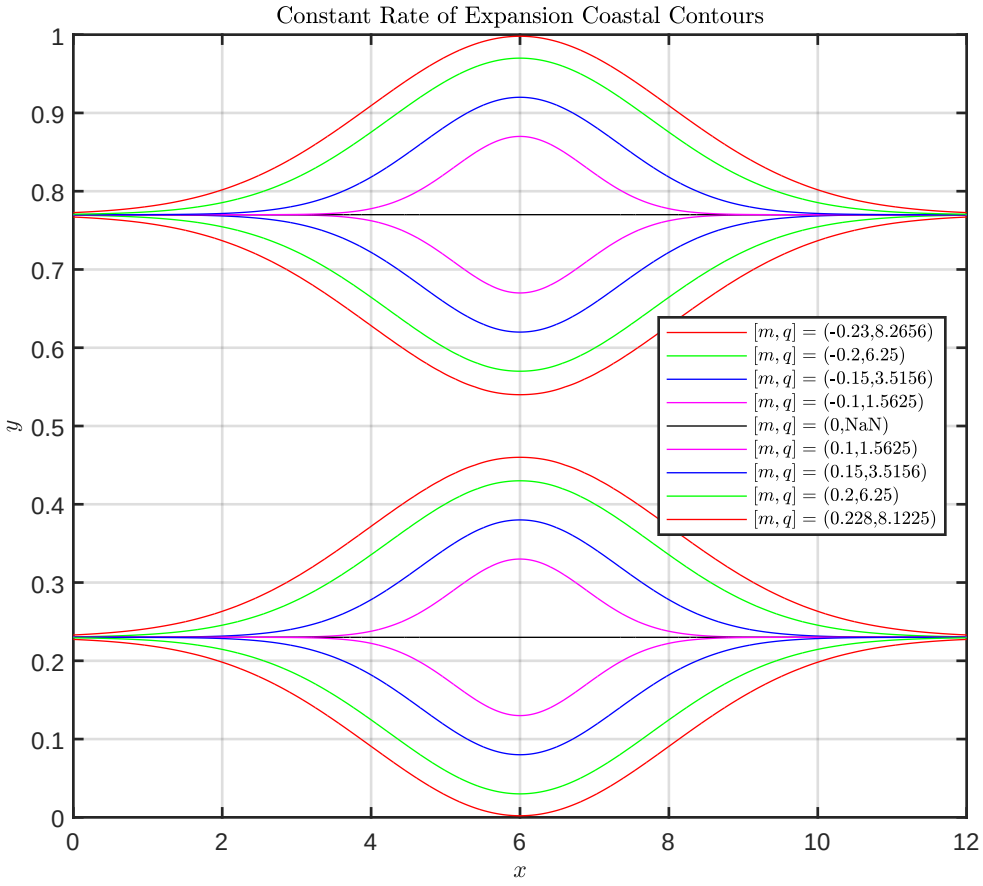

Figure 2.4: Top view of channel domains showing coastlines for 9 different simulations corresponding with expanding and contracting channels. Colors are paired for mirrored expansion or contraction. Black line indicates straight channel topography. m corresponds to amount of expansion/contraction, q corresponds to rate which is constant for all cases

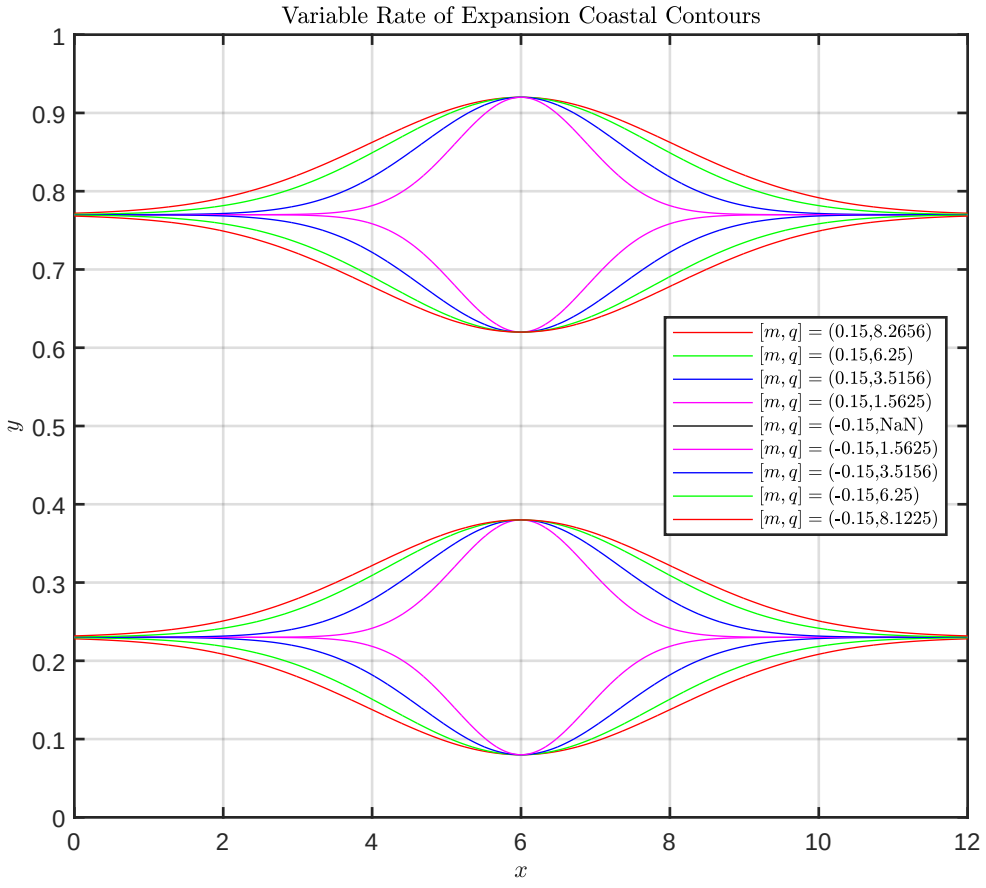

Figure 2.5: Top view of channel domains showing coastlines for 8 different simulations corresponding with expanding and contracting channels. Colors are paired for mirrored expansion or contraction. m corresponds to amount of expansion/contraction which is constant for all cases, q corresponds to rate.

Therefore, the final form of the topography function is,

$$z(x,y) = \frac{\left(1 - \left(h_1 e^{-\left(x-\frac{L_x}{2}\right)^2} + h_2 h_1 e^{-(x-L_{x2})^2}\right)\right)}{\left(0.5 - b + m e^{-\frac{\left(x-\frac{L_x}{2}\right)^2}{q}}\right)^2} (y-0.5)^2 + h_1 e^{-\left(x-\frac{L_x}{2}\right)^2} + h_1 h_2 e^{-(x-L_{x2})^2} \tag{2.5}$$

for which Fig. (2.6) shows application of Eq. (2.5) for expansion case $m = 0.23$.

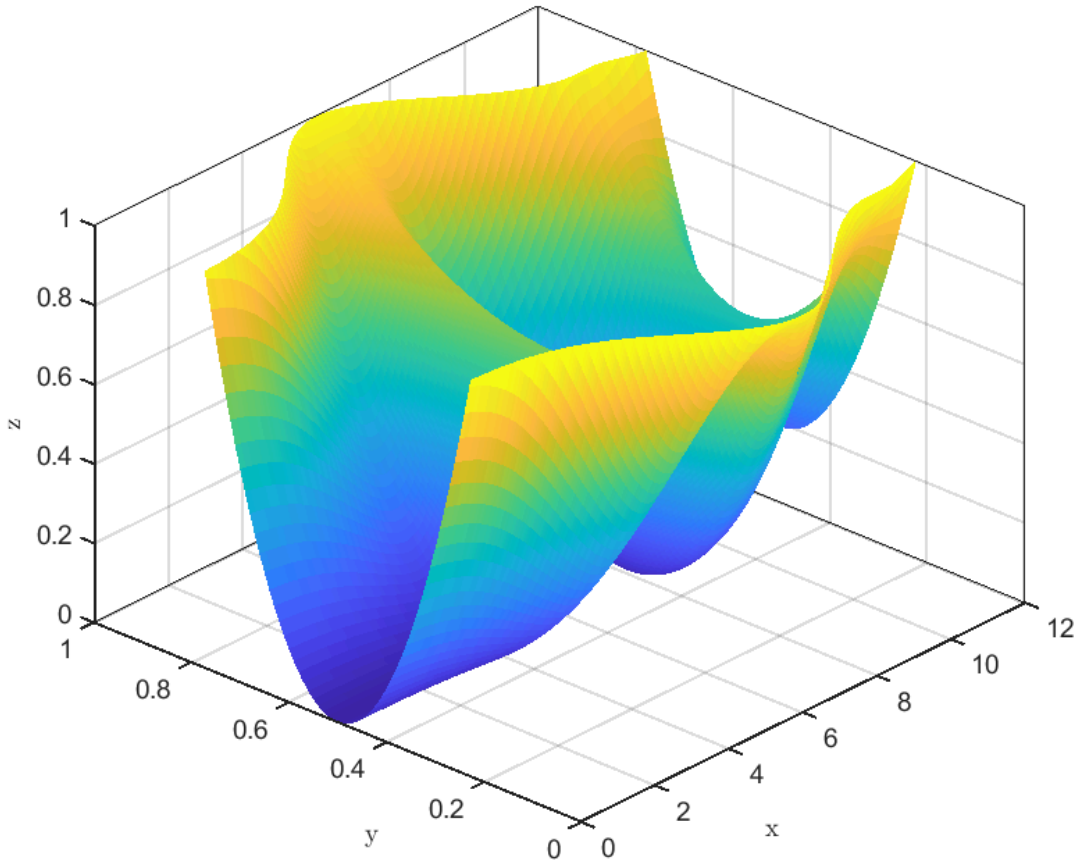

Figure 2.6: 3-D isometric surface plot for computational domain maximum expansion case $m = 0.23$

Finally, Figure 2.7 shows plots of the cross-sectional area along the channel with the minimum in each case occurring at the sill. This allows the flow to transition to supercritical at the sill and a hydraulic jump to form.

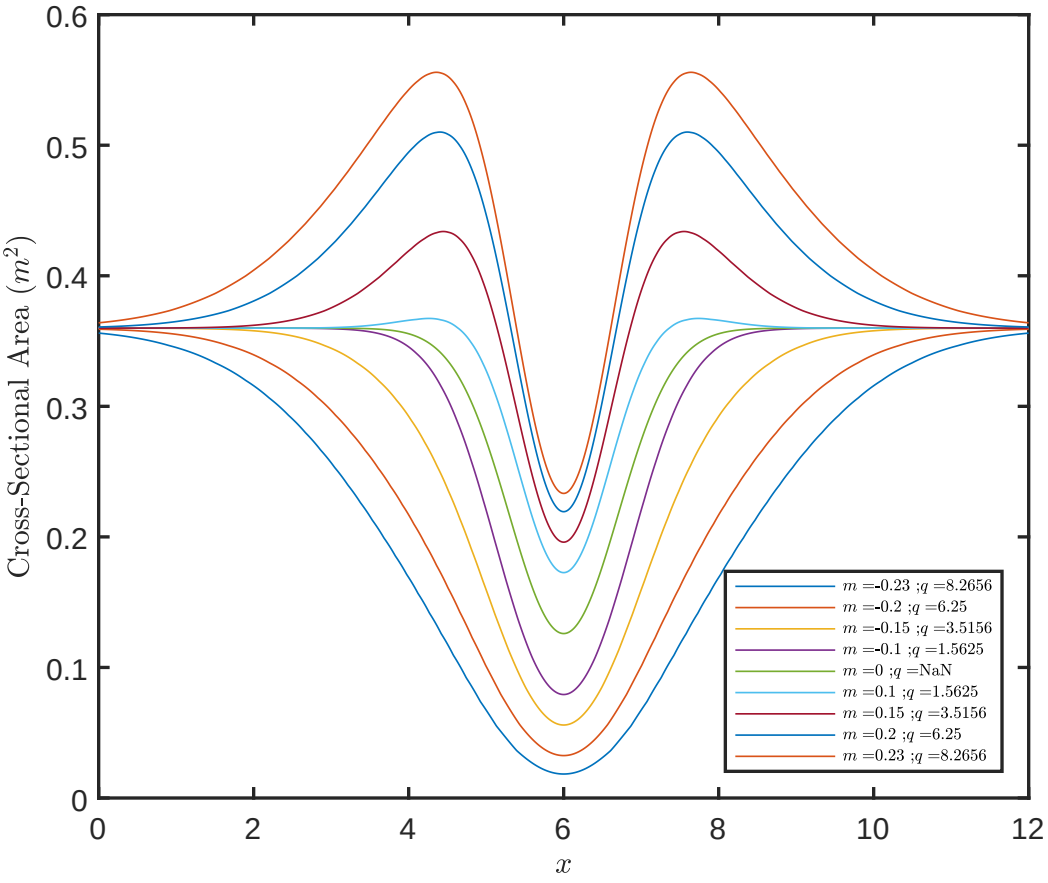

Figure 2.7: Cross-sectional areas along the channel which shows the area for each case of m is smallest at the sill, which is needed to force a hydraulic jump to occur.

For the expanding cases, the cross-sectional area is a is maximum just upstream and downstream of the sill compared to the remainder of the channel, while the cross-sectional area for contractions decreases for each case. This will alter upstream and downstream velocities in the flow, and should be considered.

Initialization and Boundary Conditions

Simulations are set up in terms of non-dimensional parameters: the characteristic length scale, L, is the maximum depth of the channel, velocity is nondimensionalized by $\sqrt{g'L}$, where $g' = g\frac{\rho_{max}-\rho_{min}}{\rho_{max}}$ is the reduced gravity, and the density field is scaled so that $T = \frac{\rho-\rho_{min}}{\rho_{max}-\rho_{min}}$. The initial density field is approximately two layered, with a hyperbolic tangent transition from a dense

lower layer to a lighter upper layer:

$$T(t=0) = \frac{1}{2}\left(1 - tanh(\lambda\,(z - 0.9))\right). \tag{2.6}$$

The interface height of 0.9 is chosen to be consistent with the thin upper layer seen in Hood Canal. This density profile is imposed at the inlet and initially throughout the domain.

The inlet velocity starts from zero and slowly ramps up over a period of time, as shown in Eq. (2.7). This is done to avoid discontinuities in the velocity field and reach maximum velocity at smoothly.

$$U_0\,(x=0) = \begin{cases} U_0 \sin\left(\frac{2\pi t}{T_t}\right) & \text{if } t < \frac{T_t}{4} \\ U_0 & \text{if } t > \frac{T_t}{4} \end{cases} \tag{2.7}$$

The time scale is $\sqrt{\frac{L}{g'}}$. Once $\frac{T_t}{4}$ the tidal cycle is reached, the simulation maintains a constant velocity U_0. A constant forcing velocity is used and a velocity profile develops naturally due to the topography.

For this work, two sets of inlet velocities are used. Simulation sets **Set B,C, E & F** (Table 2.2,2.3,2.5,2.6) use $U_0 = 0.1$ as the inlet velocity, which is based on flow-rate data obtained from Hood Canal [73]. However, due to the expansion/contraction, the average sill velocity varies between cases which could contribute to the amount of mixing. Therefore, in order to isolate the effect of the changing topography from the velocity, the flow rate across the sill should be constant between cases of different values of m.

Therefore, for simulations **Set A & D** (Table 2.1, 2.4), inlet velocities were calculated based on achieving a constant average velocity at the sill for all cases in the set. These velocities were based on the straight channel case ($m = 0$) cross-section, $U_0 = 0.1$, and the ratio of the corresponding cases cross-sectional areas to that of $m = 0$, as obtained from Fig. (2.7). This yields $[m, U_0] = [(0.23, 0.19), (0.2, 0.17), (0.15, 0.15), (0.1, 0.14)]$ for the expansions and $[m, U_0][(-0.1, 0.063), (-0.15, 0.044), (-0.2, 0.025), (-0.23, 0.015)]$ for contraction cases. In order to isolate the effect of the geometry variation on mixing, removing the effect of velocity

is justified.

The outlet boundary conditions are chosen to allow the fluid to flow out of the domain without disturbing the jump. To achieve this $\frac{\partial(\mathbf{u}T)}{\partial \mathbf{n}} = 0$ is imposed on the velocity and density fields, and $p_{out} = 0$, which allows the denser fluid to spill out of the domain while holding the lighter fluid in with hydrostatic pressure. This pressure condition, combined with the second sill transitions the flow to supercritical just ahead of the outlet, minimizing the effect of waves reflecting off the outlet and propagating into the jump region that is being analyzed.

Gerris [20] solves the incompressible Boussinesq Navier-Stokes equations as discussed in §1.2.2

$$\begin{aligned} \frac{\partial \mathbf{u}}{\partial t} + \mathbf{u} \cdot \nabla \mathbf{u} &= -\frac{1}{\rho}\nabla p' + \nu \nabla^2 \mathbf{u} - g'\mathbf{k} \\ \frac{\partial \rho'}{\partial t} + \mathbf{u} \cdot \nabla \rho' &= \kappa \nabla^2 \rho' \\ \nabla \cdot \mathbf{u} &= 0, \end{aligned} \tag{2.8}$$

where $\mathbf{u} = \{u, v, w\}$ in which u is the along channel (x-direction) velocity, w is the vertical and v is the traverse (y-direction), and $p = p_0 + p'$, $\rho = \rho_0 + \rho'$ and $\frac{\mathrm{d}p_0}{\mathrm{d}z} = -\rho g$. For the simulations, due to the high Re of the relevant flows, the turbulent viscosity is much larger than the molecular viscosity, so $\mu = 0$ is used, and eddy viscosity dominates. Furthermore, given the objective to isolate the effect of the geometry, a free slip boundary condition is used. This allows turbulence or mixing that develops as a result of the shape of the channel to be determined.

Finally, to limit the amount of data that must be saved for each simulation, instantaneous results on a set of two-dimensional slices within the channel are saved every 0.1 non-dimensional time units. The positions of along channel slices ($xz1 - 9$) are plotted in Fig.2.8 (top) and provide data for a constant y position for channel length x and height z. Slices are symmetric around the center $y = 0.5$ and are plotted in pairs spaced $dx = 1/2^7$ (grid size) apart to allow y-derivatives to be calculated. Locations were chosen for the center of the channel, just before the expansion/contraction, and within the expansion/contraction area. This allows comparison of mixing and average turbulent quantities off-center of the thalweg.

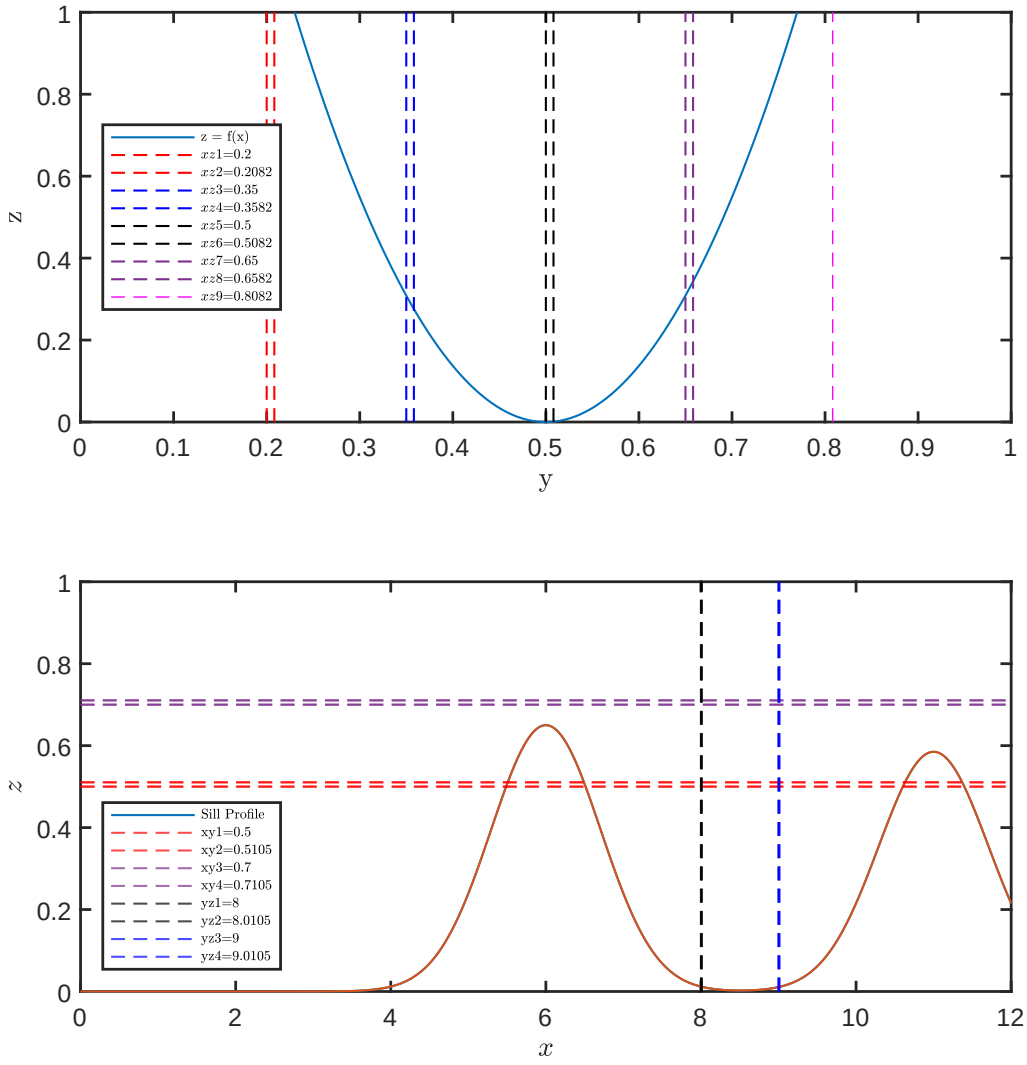

Figure 2.8: Data slices for along channel (top) xz at a fixed transverse y, along channel xy at a fixed depth z and cross channel yz at a fixed x.

Additionally, xy slices were chosen just above and below the sill height, while yz slices were chosen for two positions downstream of the sill.

Therefore, there are 6 sets of simulations with the key varying parameters being m, q, U_0 and the data slice positions, which are outlined below:

Table 2.1: Set A simulation parameters

Set A - *Constant expansion rate and constant sill velocity*								
m	q	U_0	U_{Sill}	$xz3$	$xz5$	$xz7$	t_1	t_2
0.228	8.2656	0.19	0.33	0.35	0.5	0.65	$t = 18$	$t = 30$
0.2	6.25	0.174	0.33	0.33	0.5	0.65	$t = 22$	$t = 30$
0.15	3.5156	0.155	0.33	0.35	0.5	0.65	$t = 20$	$t = 30$
0.1	1.5625	0.136	0.33	0.35	0.5	0.65	$t = 22$	$t = 30$
0	NaN	0.1	0.33	0.35	0.5	0.65	$t = 20$	$t = 35$

Table 2.2: Set B simulation parameters

Set B - *Constant expansion rate and variable sill velocity*								
m	q	U_0	U_{sill}	$xz3$	$xz5$	$xz7$	t_1	t_2
0.228	8.2656	0.1	0.13	0.35	0.5	0.65	$t = 30$	$t = 39$
0.2	6.25	0.1	0.17	0.35	0.5	0.65	$t = 31$	$t = 39$
0.15	3.5156	0.1	0.25	0.35	0.5	0.65	$t = 30$	$t = 50$
0.1	1.5625	0.1	0.2	0.35	0.5	0.65	$t = 43$	$t = 51$
0	NaN	0.1	0.33	0.35	0.5	0.65	$t = 20$	$t = 35$

Table 2.3: Set C simulation parameters

Set C - *Variable expansion rate and constant sill velocity*								
m	q	U_0	U_{sill}	$xz3$	$xz5$	$xz7$	t_1	t_2
0.15	8.2656	0.1	0.25	0.35	0.5	0.65	$t = 20$	$t = 30$
0.15	6.25	0.1	0.25	0.35	0.5	0.65	$t = 20$	$t = 30$
0.15	3.5156	0.1	0.25	0.35	0.5	0.65	$t = 30$	$t = 55$
0.15	1.5625	0.1	0.25	0.35	0.5	0.65	$t = 20$	$t = 30$

Table 2.4: Set D simulation parameters

Set D - *Constant Contraction rate with constant sill velocity*								
m	q	U_0	U_{sill}	$xz3$	$xz5$	$xz7$	t_1	t_2
-0.15	3.5156	0.044	0.33	0.35	0.5	0.65	$t = 20$	$t = 40$
-0.1	1.5625	0.063	0.33	0.35	0.5	0.65	$t = 20$	$t = 30$
0	NaN	0.1	0.33	0.35	0.5	0.65	$t = 20$	$t = 35$

Table 2.5: Set E simulation parameters

Set E - *Constant Contraction rate with variable sill velocity*								
m	q	U_0	U_{sill}	$xz3$	$xz5$	$xz7$	t_1	t_2
-0.2	6.25	0.1	1	0.35	0.5	0.65	$t = 20$	$t = 40$
-0.15	3.5156	0.1	0.65	0.35	0.5	0.65	$t = 20$	$t = 40$
-0.1	1.5625	0.1	0.48	0.35	0.5	0.65	$t = 20$	$t = 30$
0	NaN	0.1	0.33	0.35	0.5	0.65	$t = 20$	$t = 35$

Table 2.6: Set F simulation parameters

Set F - *Variable Contraction rate with constant sill velocity*								
m	q	U_0	U_{sill}	$xz3$	$xz5$	$xz7$	t_1	t_2
-0.15	6.25	0.1	0.65	0.35	0.5	0.65	$t = 20$	$t = 40$
-0.15	3.5156	0.1	0.65	0.35	0.5	0.65	$t = 20$	$t = 40$
-0.15	1.5625	0.1	0.65	0.35	0.5	0.65	$t = 20$	$t = 30$

Grid Convergence

Some recent studies [29][73][67][47] which have investigated hydraulic jumps in a similar domain using Gerris suggest that a grid resolution of 2^7 in the vertical provides adequate solutions to hydraulic jump problems that are independent of mesh size. However, to confirm that the resolution is sufficient, a convergence study is conducted here.

Results were obtained for the straight channel case ($m = 0$), with no expansion or contraction. 3D simulations were run for a grid resolution of 2^6, 2^7 and 2^8, for which data down

the center of the channel ($y = 0.5$) is compared between resolution numbers to determine the appropriate refinement level.

Shown in Fig. (2.9) are the results with a clear hydraulic jump occurring in the lee of the sill for a each of the grid resolutions. Jumps are shown to develop in the same manner, with little visible variation.

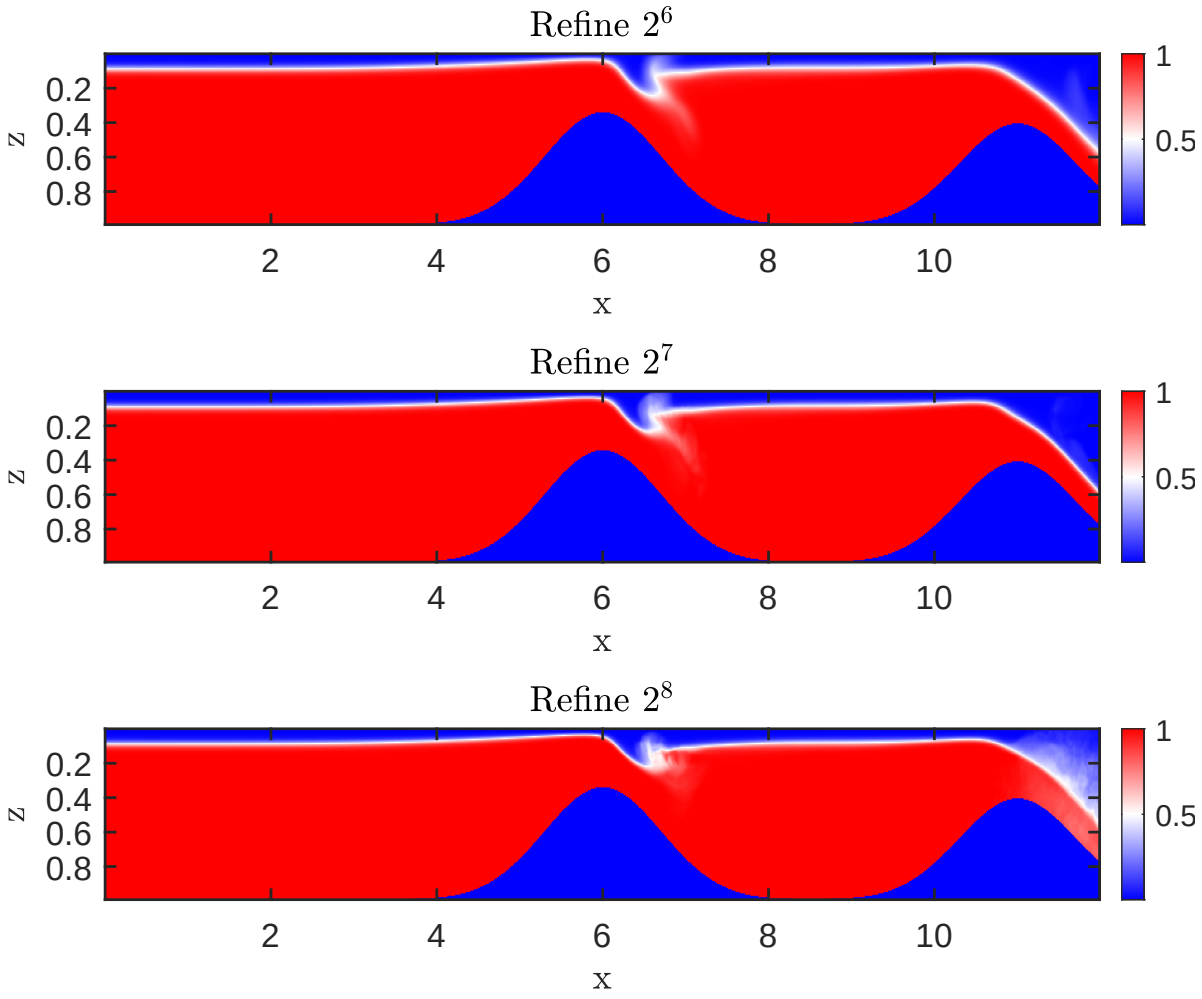

Figure 2.9: Comparison of levels of grid refinement with density plots showing jump development for data in the center of the channel for the straight channel case, $m = 0$. Coarsest grid is 2^6, while finest grid is 2^8. Topography appears in blue below the red, denser fluid.

A more quantitative measure of grid independence can be determined using the interface height. This is a measure of the position between different densities in the two-layer flow, and was the main marker for grid independence in the previously mentioned studies. Interface

height is defined as,

$$R(x) = \int_0^z \frac{\rho\,(x,z) - \rho_{min}}{\rho_{max} - \rho_{min}} \mathrm{d}z, \tag{2.9}$$

and is shown in Fig. (2.10) depicting the differences between refinement levels, for which the minimum depth of the interface heights for 2^6, 2^7, and 2^8 were 0.539, 0.571, and 0.572, respectively. The percent difference change is much smaller between the higher resolution cases than the lower, and the computing time was substantially longer for solutions with 2^8.

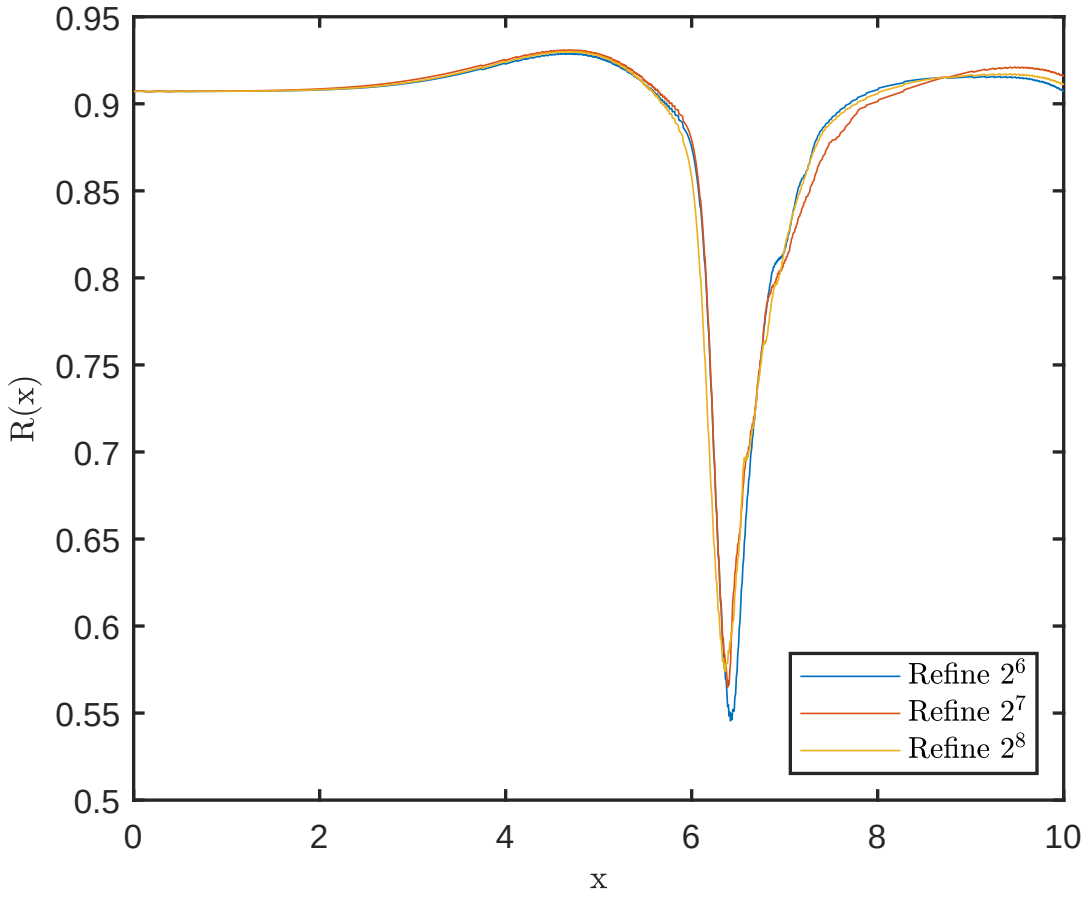

Figure 2.10: Interface height $R(x)$ for refinement levels 2^6, 2^7 and 2^8, in the straight channel case $m = 0$ along the channel centre line.

Maintaining a consistent jump location between simulations is important for verification that the solutions are independent of the level of refinement. Interfaces show very little change between refinement levels, however running a grid resolution of 2^8 drastically increased the

computational cost, while 2^6 caused the solution to become unstable near the outlet earlier than the other cases. Therefore, given previous work has been successful with similar simulations and a resolution of 2^7 [67][73], and the agreement that the results are grid independent, this work will continue with a resolution of 2^7.

2.3 Verification

Lack of experimental results for expanding and contracting channels with hydraulic jumps make analytical and observational verification challenging. However, simulations by Mucaza [67] and Ogden [6][29][76] with an identical numerical set up and simpler topographies have been compared to analytical solutions showing good agreement.

Mucaza uses the Gerris finite volume CFD solver where the sub-grid is modelled implicitly with the ILES scheme. The channel has a rectangular cross-section with 12 boxes in the x, and a height of 1. A sill exists in the channel center at $x = 6$ and follows a similar Gaussian profile that was used here, with a sill height of 0.65 also guided by the sill height as Hood Canal [7]. The velocity and density profiles are non-dimensional, and the inlet velocity is forced from zero to the maximum over $1/4$ of a time scale. Additionally, the grid resolution is refined to 2^7, with a free slip boundary with hydrostatic pressure and Neumann condition applied to the outlet density and velocity. Likewise, Ogden [6] simulated 2D and 3D flows using Gerris with resolutions of 2^8 and 2^7, respectively. A Gaussian function describing the sill and a hyperbolic tangent density profile [6]. The velocity reached a maximum at a quarter of the tidal cycle, with a hydrostatic pressure imposed on the outlet and free slip boundaries. The sill profile and domain was non-dimensionalized according to the topographic sill heights at Hood Canal, Stellwagen Bank and Knight inlet. Due to the similarities between the aforementioned simulations and those conducted in this work, mixing results were of a similar order of magnitude, while the development of the jump and interface height structure compared well. Therefore, reasonable verification to analytical and observational data can be made based on

the similarities with Ogden [6] and Mucaza [67].

Both Ogden and Mucaza compared their numerical results to the two layer theories developed by Klemp *et. al* [25] and Wood & Simpson [24] outlined in 1.2.3 and produced jumps with that show good agreement with the theoretical results. Idealized simulations without topography show excellent agreement with the theories (Ogden & Helfrich [29]; Mucaza [67]), which assume the jump occurs instantaneously. Simulations with topography variation deviate more from theoretical predictions because the channel depth varies across the jump, which is not instantaneous in real flows. However, the agreement is still reasonable given the added complexity of the simulation.

Furthermore, Ogden compared the ILES simulations conducted with Gerris, which has shown good agreement with DNS [66], to theoretical models by Borden & Meiburg who developed a circulation based model to analyze gravity currents [28]. Predictions of the vorticity flux by their theory showed good agreement with their numerical simulation results and the frontal bore velocity predicted agreed reasonably well with the front velocities in their DNS gravity currents. Ogden [6] found that for the parameters being considered the vorticity budget integrated over the jump region agreed reasonably well with the mass balance of Borden & Meiburg.

Finally, Ogden also compared the numerical results of idealized two-dimensional simulations to observational data available for Stellwagen bank. This flow is tidally driven with a sill forced hydraulic jump in the lee of the sill, similar to the simulations conducted here. Comparisons showed that the production of an undular bore with trailing shear instability and the first two wave speed modes agreed with observations. Some differences did arise due to slightly different topography in the location of the observations and instantaneous density profiles likely not the same as those upstream of the sill at the bank. Regardless, the results do indicate that the parameter space extends to jumps in the environment.

Therefore, given Mucaza [67] and Ogden [29][6] showed sufficient agreement with analytical and observational results, as well as independently conducted DNS simulations which

compared well to analytical results, and the simulation set up and results from this work are similar, the simulations used here are reliable.

2.4 Results and Discussion

The main objective of this work is to analyze how a lateral expansion or contraction coincident with a sill impacts the hydraulic jump. In order to characterize the jump and investigate how turbulence and mixing are affected, the time averaged turbulence statistics of the flow are analyzed. The jump is averaged over a period of time in which the jump is fully established and does not abruptly change from one moment in time to the next. Statistical correlations of the perturbations from this average can be calculated, allowing terms from the turbulent kinetic energy (TKE) and scalar variance equations, which quantify the mixing in the flow, to be analyzed.

Figure 2.11 shows instantaneous snapshots of the topographically forced hydraulic jump occurring along the center of the channel, for the case with no expansion or contraction ($m = 0$).

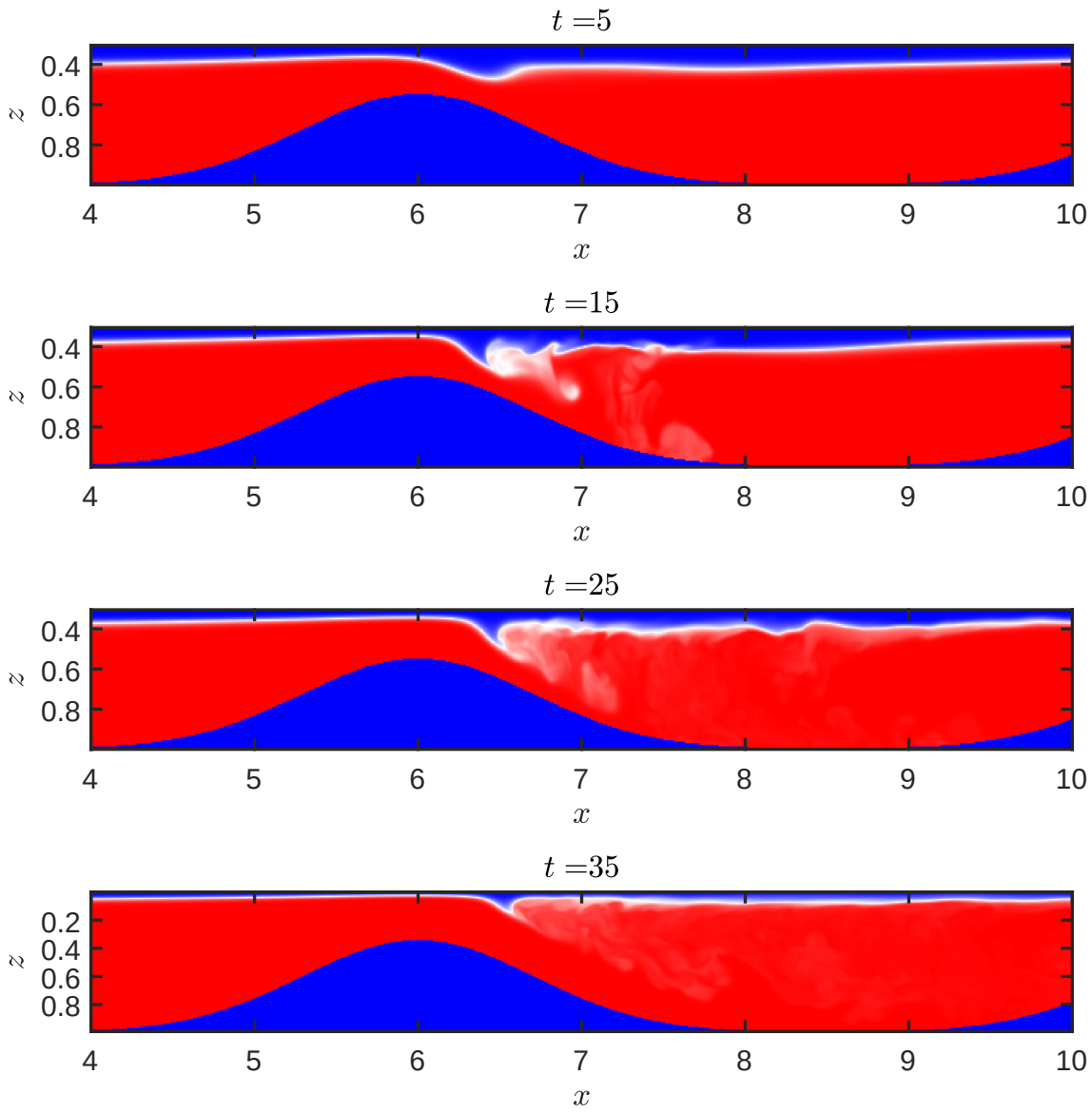

Figure 2.11: Instantaneous ρ plots of hydraulic jump along slice $xz5$ (channel center) for non-dimensional time $t = 5$ to $t = 35$ and case $m = 0$ with no cross-sectional variation. Topography appears in blue below the red, denser fluid.

The inlet velocity reaches the maximum value at t = 12.5. At $t = 5$ the stratified flow spills over the topography, becoming supercritical until a point just past the peak of the sill where the flow is met by slow downstream flow causing an internal hydraulic jump to occur. Between $t = 5$ to $t = 15$, the jump is developing and changes qualitatively with time. While turbulent eddies still exist, the jump can be considered stationary after $t = 20$. The jump may

still develop slowly, so the averaging period must be short enough that the jump is structurally similar throughout the entire averaging period.

Finally, comparing how jump structure and mixing vary across the channel is important as mixing may vary across the width due to an expansion or contraction. As mentioned, case $m = 0$, corresponding to a channel with a constant width should see little to no variation, however some may be expected due to the parabolic shape of the cross-section. Therefore, symmetric slices at $y = 0.35$ ($xz3$) and $y = 0.65$ ($xz7$) are compared for an averaging period from $t = 20$ to $t = 35$ with $dt = 0.1$, for a total of 251 instantaneous snapshots of the flow. In Figure 2.12 it is shown that the jump structure varies little between $t = 25$ to $t = 35$ for the time averaged density in slices $xz3$, $xz5$, and $xz7$. As expected, symmetry is achieved across the channel.

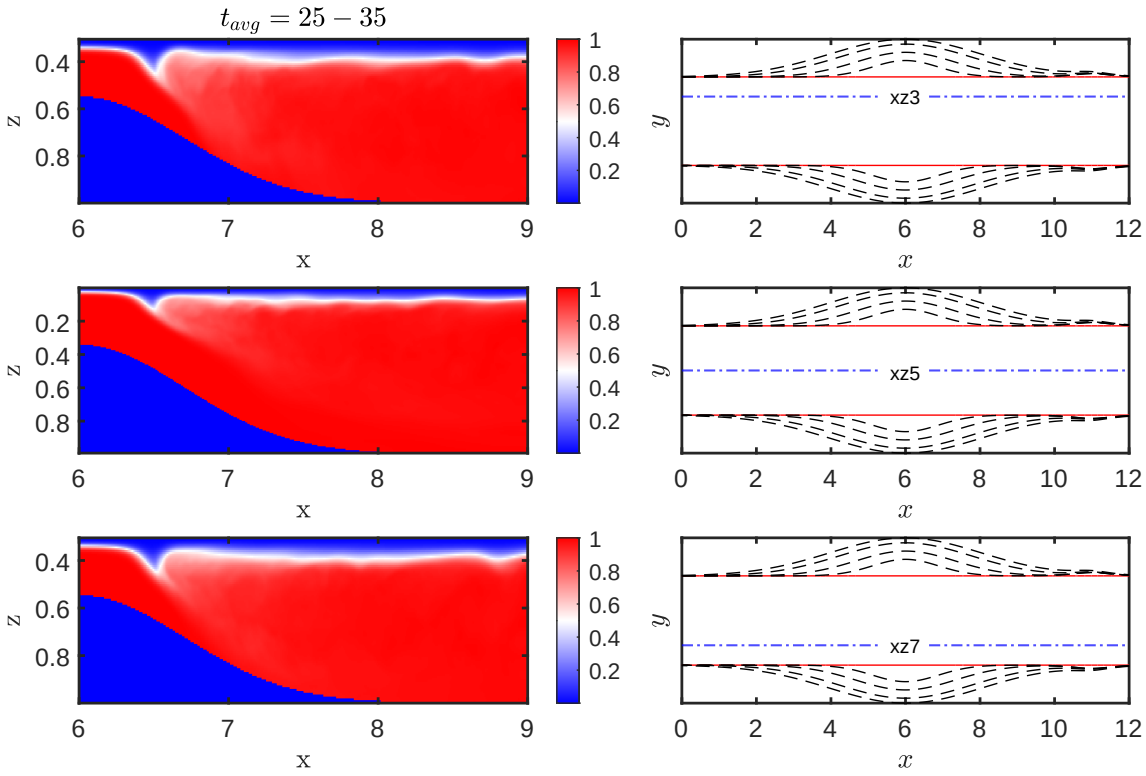

Figure 2.12: Time averaged density plots (left) between $t = 25$ to $t = 35$ for data in a position across the channel. Outline of topography (right) with domain highlighted in red ($m = 0$). Channel positions are $y = 0.35$ ($xz3$), $y = 0.5$ ($xz5$) and $y = 0.65$ ($xz7$).

The results are broken into 2 main sections: *Expansion* and *Contraction*. Within these sections, multiple sets of simulations are run with parameters shown in §2.2.2. Simulation **Set A**, which contains results for the *constant rate of expansion* with a *variable inlet velocity* U_0, are discussed first and in detail, as isolating the effect expanding geometry on mixing is the main objective. Subsequent sections will mainly look at the mixing and cross-channel variation, if any, that occurs.

2.4.1 Channel Expansion

Set A - Constant Expansion with Variable Inlet Velocity

Set A - *Constant expansion rate and constant sill velocity*					
m	q	U_0	U_{Sill}	t_1	t_2
0.228	8.2656	0.19	0.33	$t = 18$	$t = 30$
0.2	6.25	0.174	0.33	$t = 22$	$t = 30$
0.15	3.5156	0.155	0.33	$t = 20$	$t = 30$
0.1	1.5625	0.136	0.33	$t = 22$	$t = 30$
0	N/A	0.1	0.33	$t = 20$	$t = 35$

Parameters for simulation **Set A** are shown in Table 2.1, with turbulent statistic averaging done over various time ranges where the jump was stationary. Inlet velocities, U_0, increase with m such that the velocity at the sill, U_{sill}, is the same for all cases, based on the control case of $m = 0$ (straight channel). Instantaneous snapshots of the jump development for each case are shown in Figure 2.13, and demonstrate the characteristic formation of the hydraulic jump in the lee of the sill.

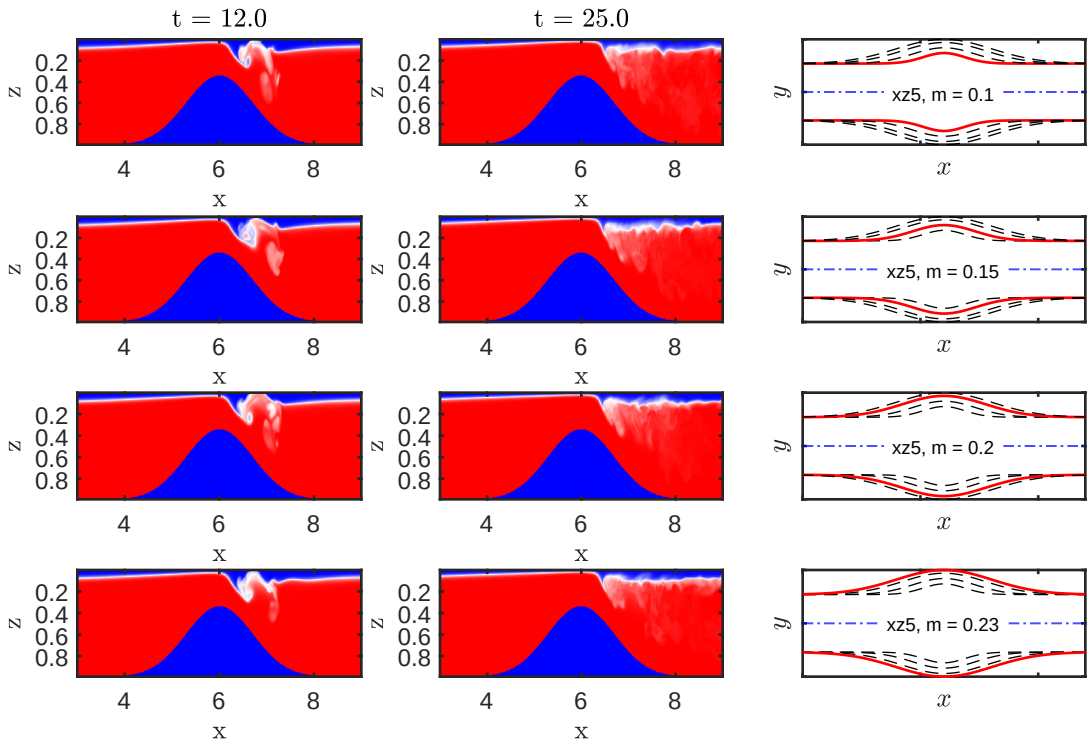

Figure 2.13: Set A instantaneous density snapshots of jump development at $t = 12$ and $t = 25$ for expanding channel with variable inlet velocity (left & middle). Corresponding topographies highlighted in red (right)

Due to the same average velocity over the sill, jump development along the thalweg is similar between all cases at $t = 12$. At this time, overturning caused by the abrupt change in velocities from upstream to downstream occurs. Furthermore, the density interface is shown to rise at the sill, before spilling over. At $t = 25$ the jump has become fully developed and stationary so that time averaging can be done.

Comparison of structure across the jump also gives an indication of any anomalies or variation that may occur across the channel.

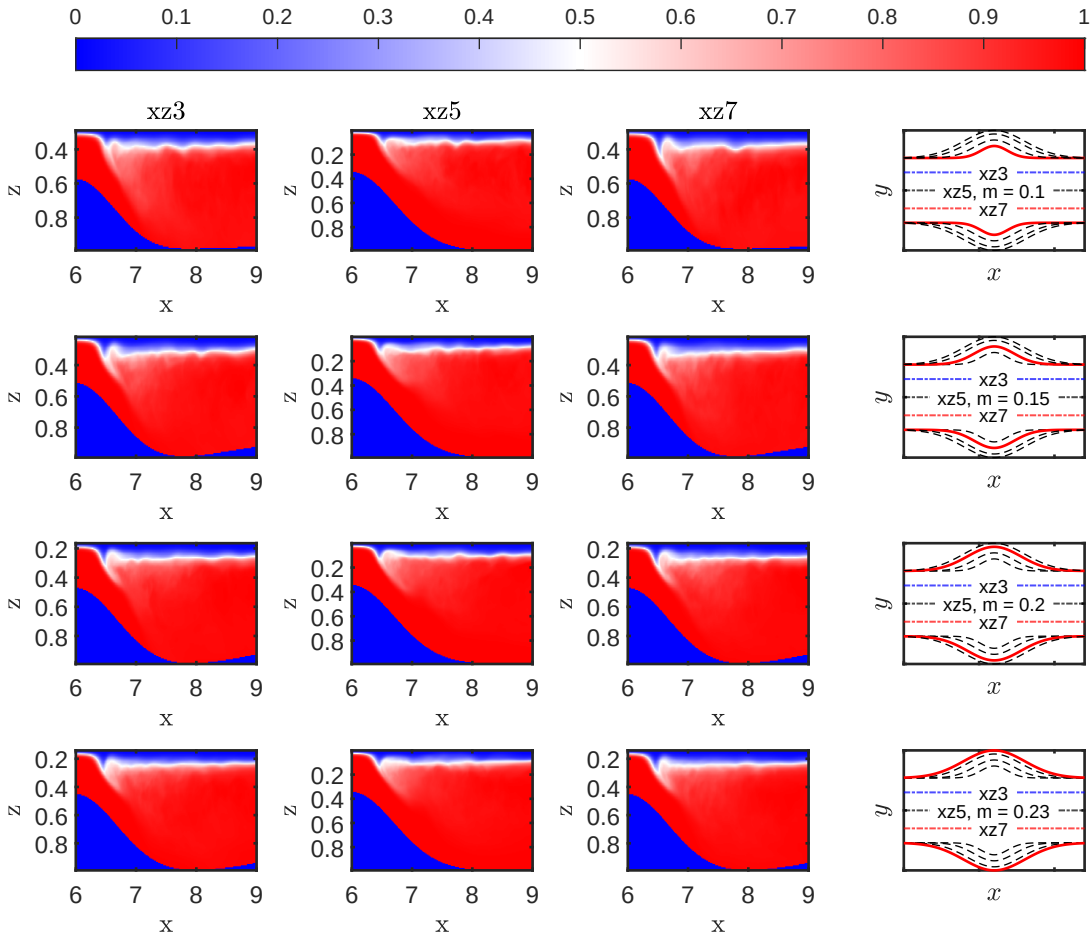

Figure 2.14: Transverse channel density comparison for expansion cases $m = [0.1, 0.15, 0.2, 0.23]$ with a constant velocity through the minimum cross-section. Slices $xz3$ to the left of center (left) and $xz5$ center slice (center) and $xz7$ right of center (right). Topography plots for each row (right) highlighted in red.

Figure 2.14 shows that, due to the symmetry, data slices $xz3$ and $xz7$ have similar structures as expected. However, a more detailed comparison of the transverse jump variation can be obtained by calculating interface height, $R(x)$, from Eq. (2.9).

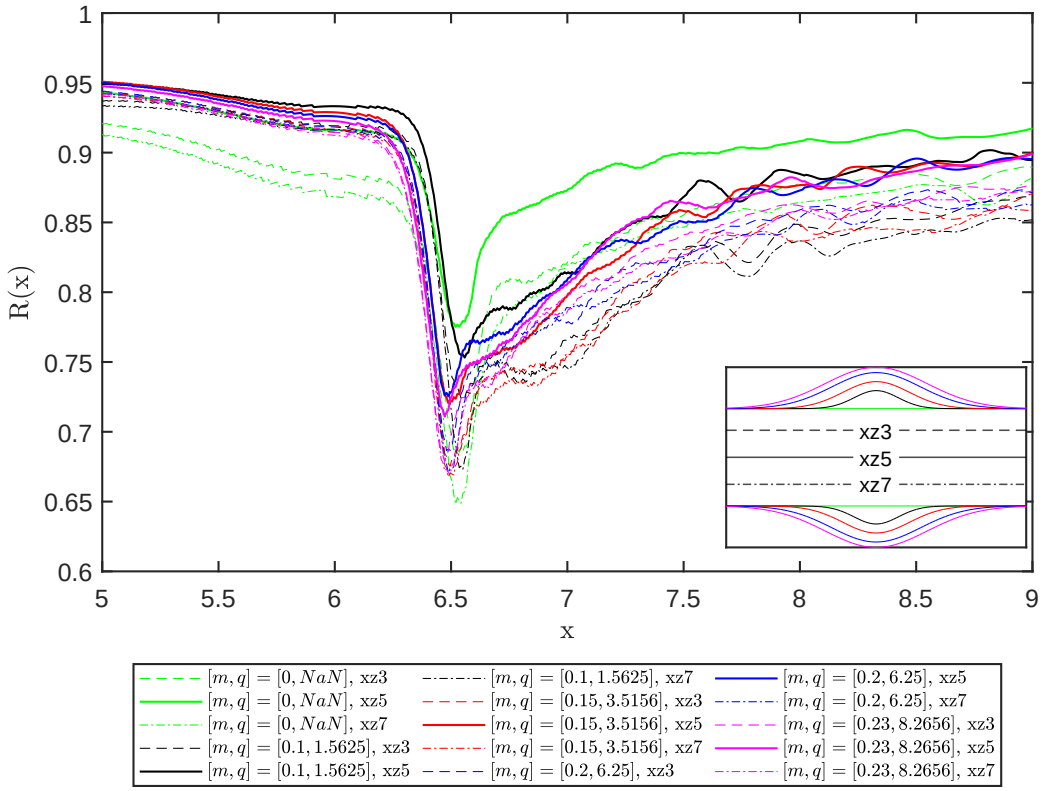

Figure 2.15: Set A interface height, $R(x)$, for expansion m at transverse channel positions $y = 0.35$, $y = 0.5$ and $y = 0.65$. Topographies corresponding to interface heights (bottom right) where solid lines indicate center of channel and dotted lines indicate off center.

A comparison of the interface heights for each case of m, and for each slice across the channel ($xz3$, $xz5$, $xz7$) is shown in Figure 2.15, showing that the position of the jump is similar for each case, and symmetry is maintained across the channel. However, for case $m = 0.1$, which has the smallest expansion, the jump occurs further downstream than for the other cases. Given the position of the jump in proximity to the minimum cross-sectional area (shown in Figure 2.7), the amount of change in the channel is small compared to the other cases, and thus shows closer agreement with case $m = 0$, for the straight channel jump.

Depths of the interface height also trend deeper with increasing values of m. This is a logical result for the sill combined with the expansion. In the case of a straight channel, the sill first causes the fluid to slightly rise as it is pushed over the sill by the forced inlet velocity;

this upstream adjustment occurs in this case due to the specific interface height and topography applied in the simulations. The lower layer then spills over the sill, becoming supercritical downstream, and forming the hydraulic jump. However, in cases with an expansion, the decrease in cross-sectional area at the sill is smaller (Fig. 2.7 & Fig. 2.15), so less upstream adjustment is required for the flow to spill over the sill; this is consistent with expectations based on single layer hydraulics. Therefore, the larger the expansion, the less the fluid has to rise due to the sill and the lower the interface height.

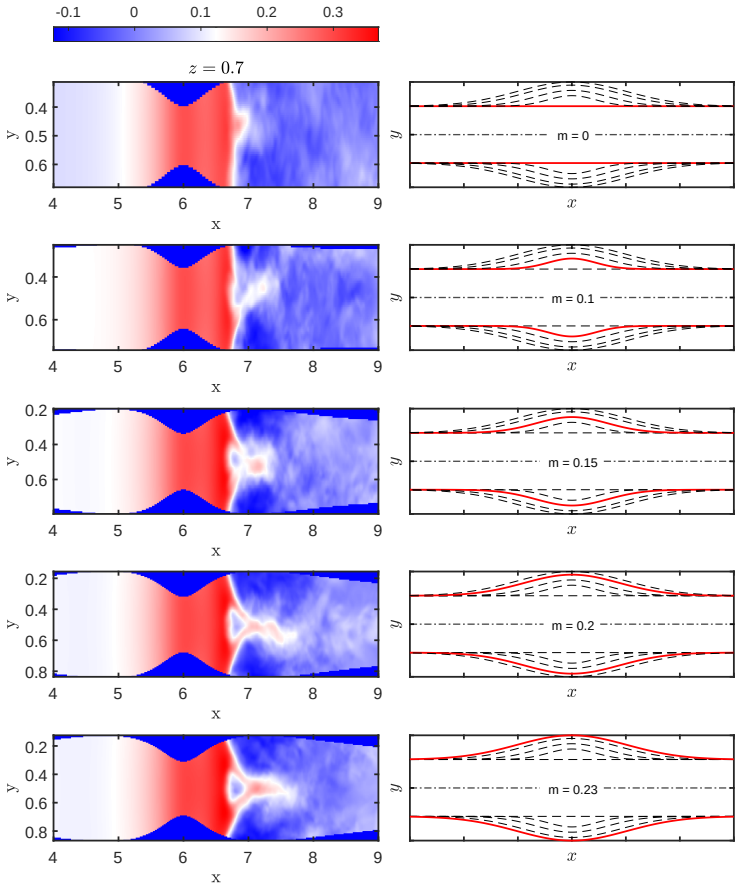

Figure 2.16: Set A time averaged u velocity for increasing rates of expansion at an xy slice z = 0.7 (left). Corresponding topographies highlighted in red (right). Sill velocity constant for each case, with non-dimensional velocity amount (top) indicated with red coloring as supercritical, and blue as sub-critical.

Time averaged velocity plots (Fig. (2.16) show the highest average velocity is along the channel thalweg and becomes increasingly uniform and intense as the amount of expansion

increases. This occurs as a result of the expansion; as flow travels over the sill at a constant average velocity between cases, the velocity off center continues diverging laterally. The flow is accelerated by the contracting sill, however on the leeward side, the channel cross-sectional area immediately increases. Due to mass conservation and diverging velocities off-center, the velocity in the expansion is immediately reduced. Center-line flow is the furthest from expansion, and has been sped up by the sill. Therefore, despite free slip conditions at the walls, the highest velocity remains in the channel center and is less effected by the geometry.

Furthermore, the velocity plots show a region in the center of the channel for which the velocity is reduced at the jump, and then accelerated to a higher velocity downstream (at $x = 7.3$). Figure 2.17, shows the time averaged u velocity in the xz direction for off-center ($y = 0.35$) and thalweg data ($y = 0.5$).

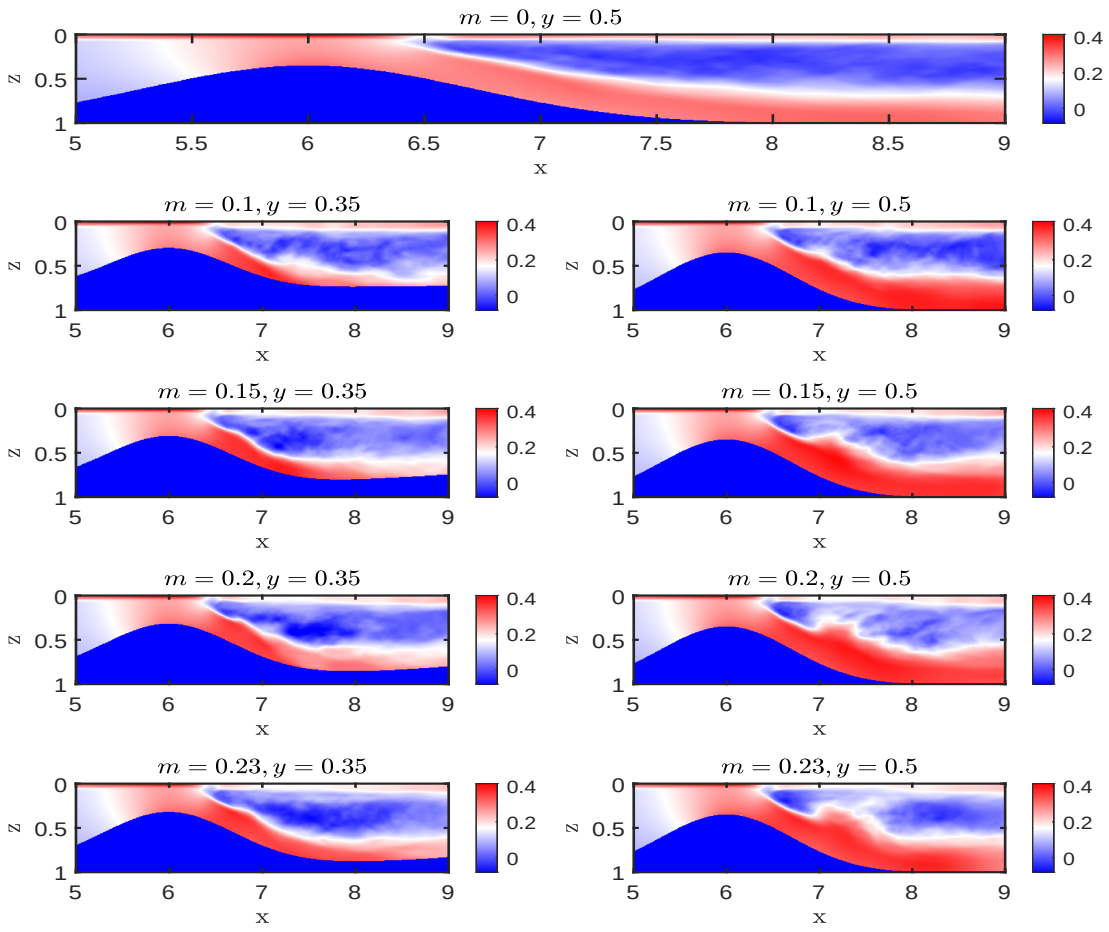

Figure 2.17: Set A along channel average u-velocity for cases $m = [0, 0.1, 0.15, 0.2, 0.23]$ (top-bottom) along the thalweg ($y = 0.5$, $xz5$) and off-center ($y = 0.35$, $xz3$) (right - left).

Given the no slip condition, the most dense fluid at the bottom boundary which would have more inertia over the sill, and the parabolic channel profile causing a relative minimum cross-section at the bottom of the channel and a maximum at the top, the velocity along the bottom of the channel is the highest. As the flow spills over the sill, the velocity at the top of the channel is immediately reduced due to the briefly increasing cross-sectional area in the lee of the sill (Fig. 2.7), however the hydraulic jump simultaneously occurs due to the sill and velocity transition and thus as m increases, the contrast in velocity becomes more intense. This results in a increase in the velocity downstream due overturning and turbulence in the hydraulic jump. Likewise, this increase in velocity is not as prominently seen in the off-center data ($y = 0.35$), where the velocity is substantially less than the thalweg. This would indicate

higher vorticity caused by the velocity variations in the jump which increases with increasing expansion.

Additionally, as m increases the channel expansion may cause the amount of vorticity to increase. The vertical and lateral rotation caused by the changes to geometry are expected to be associated with mixing in the channels. To investigate the presence and strength of these vorticies, the vertical vorticity of the average flow is calculated in a horizontal plane. Figure 2.18 shows that the magnitude of the vertical vorticity, $\omega_z = \frac{\partial u}{\partial y} - \frac{\partial v}{\partial x}$ increases with increasing rates of expansion. Streamlines, plotted over the vorticity, indicate two symmetric regions of recirculation just downstream of the jump. The streamlines and vorticity indicate that the strength and coherency of these recirculation regions increases for geometries with larger expansions.

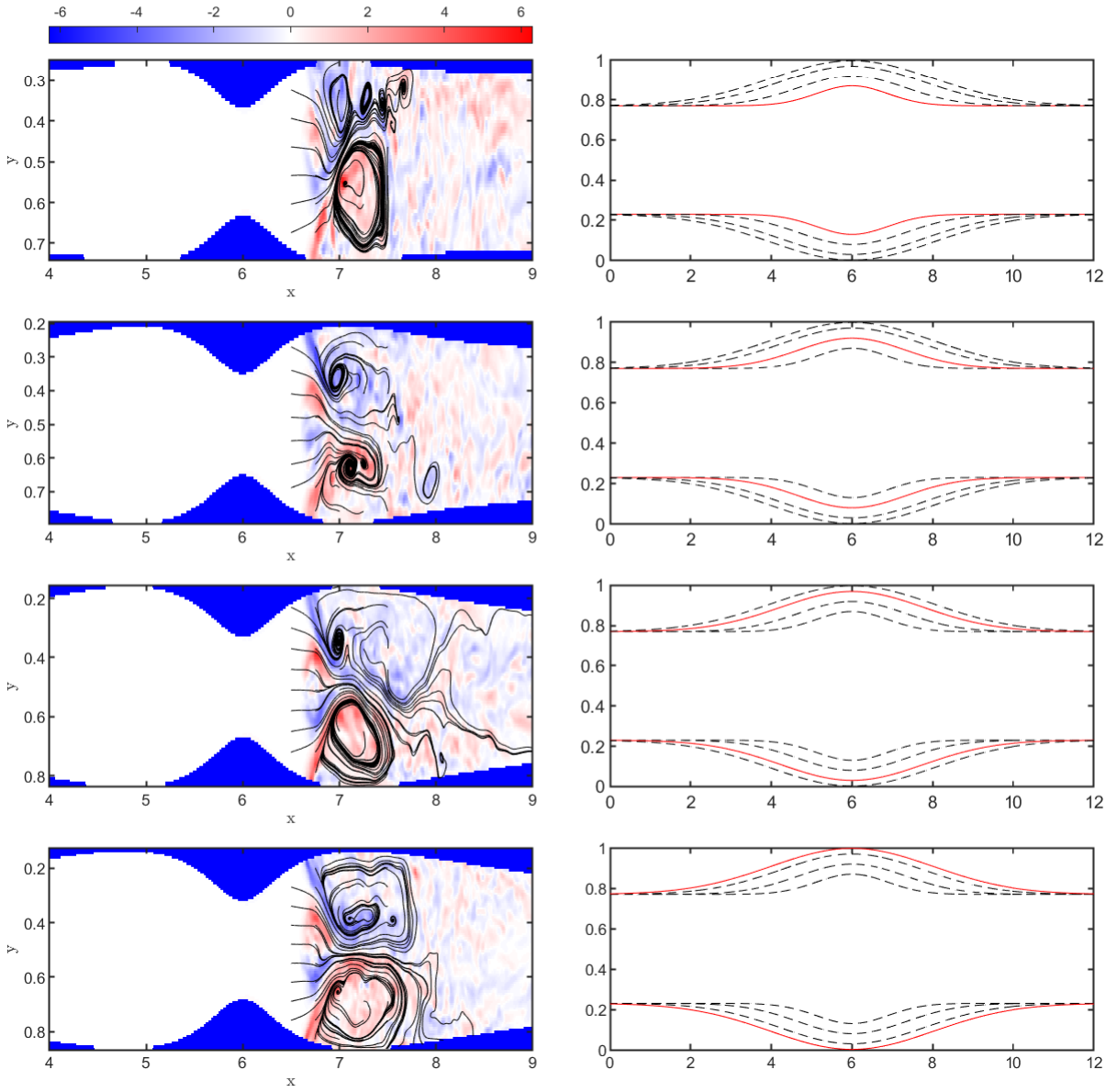

Figure 2.18: Set A time averaged vorticity, ω for increasing rates of expansion, $m = [0.1, 0.15, 0.2, 0.23]$ with a constant average velocity across the sill (left). Topography plots with corresponding topography case outlined in red (right). Results are shown across the channel at a depth of 0.3, just above the sill crest.

The larger expansion causes the flow to briefly diverge directly after being sped up by the sill due to the increase in cross-sectional area, even though the channel begins to contract downstrem. The contrast between the maximum flow in the thalweg, and the diverging flow with substantially reduced velocities closer to the geometric extents results in recirculation in the lee of the sill. Thus as the size of the expansion increases, so does the intensity of the curl.

Additionally, the vorticity appears to become more symmetric and larger as m increases, while also being the most intense toward the thalweg (see Figure 2.27 on page 84 for a comparison of all expansion simulation sets). This is likely because the larger expansions allow for larger vorticies to develop, as there is more space downstream before the channel begins to contract back to the same width as the inlet. Additionally, as the velocity plots outlined, the contrast in thalweg compared to off-center velocity increased as the expansion increased. Therefore low values of m shows smaller vorticies occurring.

Their ability to dissipate large amounts of energy and to modify water properties through mixing is one of the main reasons a better understanding of internal hydraulic jumps is important. To calculate the amount of mixing, and observe the variation as channel expansion increases, scalar variance is considered. Scalar variance is governed by,

$$\frac{\partial\overline{\theta'^2}}{\partial t} + \overline{u}_j\frac{\overline{\theta'^2}}{\partial x_j} + 2\overline{u'_j\theta}\frac{\partial\overline{\theta}}{\partial x_j} - \frac{\partial}{\partial x_j}\left(\overline{u'_j\theta'^2} + \kappa\frac{\partial\overline{\theta'^2}}{\partial x_j}\right) = -2\kappa\overline{\left(\frac{\partial\theta'}{\partial x_j}\right)^2} \tag{2.10}$$

where $\frac{\partial\overline{\theta'^2}}{\partial t} \approx 0$ since the jump is stationary over the averaging period.

$$\overline{u}_j\frac{\partial\overline{\theta}^2}{\partial x_j} = \frac{\partial}{\partial x_j}\left(\overline{u}_j\overline{\theta'^2} + \kappa\frac{\partial\overline{\theta'^2}}{\partial x_j}\right) - 2\kappa\overline{\left(\frac{\partial\theta'}{\partial x_j}\right)^2}. \tag{2.11}$$

Approximately stationary hydraulic jumps are considered, so the time derivative can be neglected. If an area integral of the remaining terms over the region of the jump is then calculated, the net flux of scalar variance out of the region of the jump plus the scalar variance dissipated within the jump region will be balanced by the production of scalar variance within the jump region. Therefore, the cumulative area integral of the scalar variance production in the region of the jump is calculated to quantify the mixing within the jump:

$$\int_a^b\int_{h_B}^1\left(w'\theta'\frac{\partial\overline{\theta}}{\partial z} + u'\theta'\frac{\partial\overline{\theta}}{\partial x} + v'\theta'\frac{\partial\overline{\theta}}{\partial y}\right)\mathrm{d}z\mathrm{d}x. \tag{2.12}$$

In this case, density is the scalar of interest, so $w'T\frac{\partial\overline{T}}{\partial z}$ is the vertical mixing component, $u'T\frac{\partial\overline{T}}{\partial x}$

is the horizontal and $v'T\frac{\partial \overline{T}}{\partial y}$ is the lateral. To quantify the mixing within the jump, an upstream point, a, is chosen for each case (both expansions and contractions) just ahead of where the jump has developed. The downstream point, b, is averaged over a region downstream of the jump shown in Figure 2.19

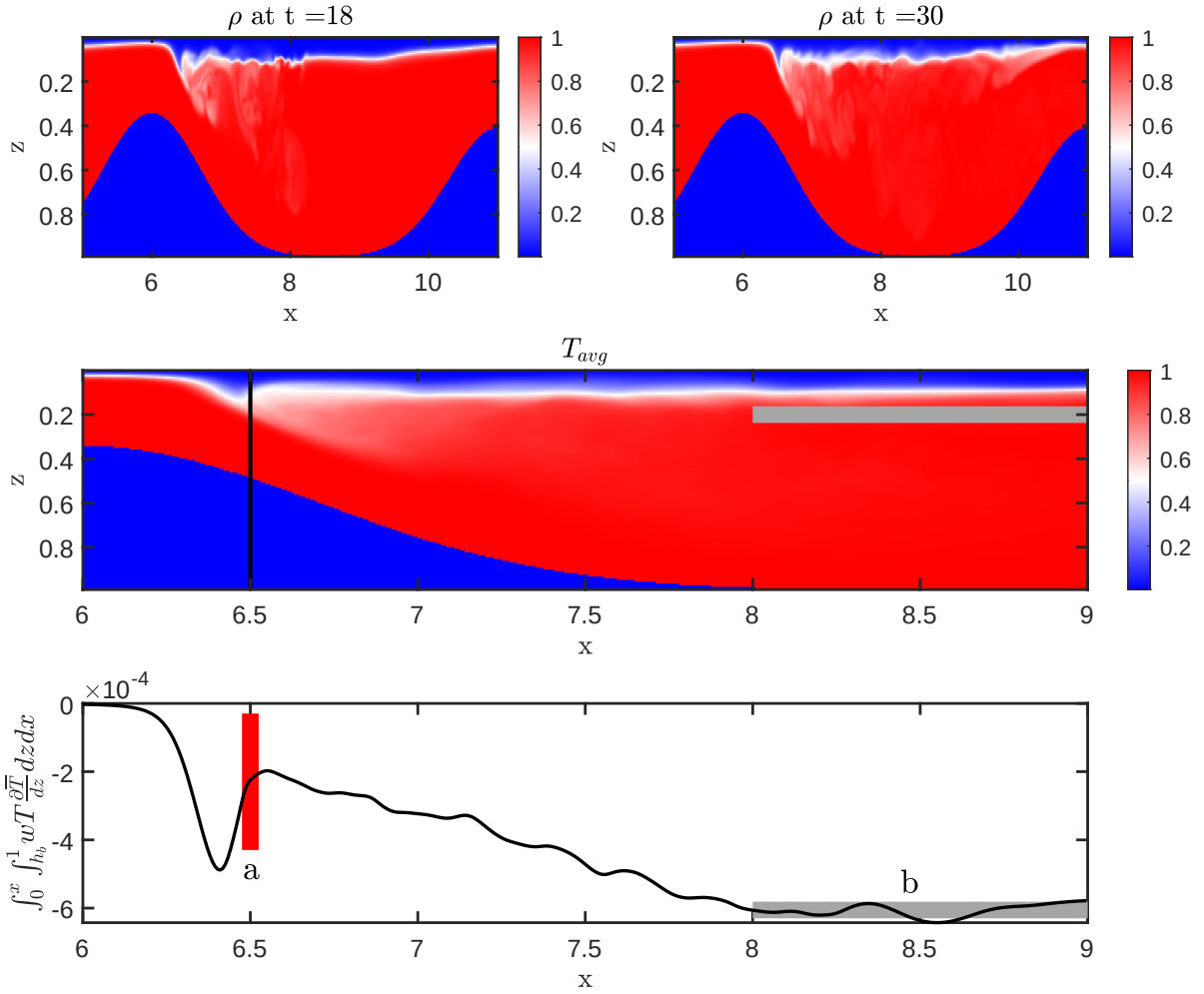

Figure 2.19: Set A instantaneous thalweg (y = 0.5) ρ snapshots (top) over turbulence averaging period for average turbulent ρ (T) (middle), and vertical scalar variance production in jump region (bottom) for expansion case m = 0.23

Figure 2.19 shows the time averaged density field, the instantaneous density fields at the initial and final time of the averaging period, the cumulative integral of the vertical scalar variance production and the point a and extent b that define the jump region for the case m = 0.23. The cumulative scalar variance production integral decreases in the region of the jump,

representing mixing caused by the turbulence in the jump. A flow with distinct, alternating, and persistent regions of high and low density have high scalar variance. As the flow mixes, high and low density fluids combine to form fluid of moderate density, reducing the scalar variance of the flow. A negative cumulative integral of scalar variance production therefore indicates mixing.

Due to the velocity profiles shown in Figure 2.16, vertical mixing is expected to be greatest in the center of the channel, $y = 0.5$ ($xz5$) where velocity is the highest because higher velocity jumps with more shear between layers have previously been shown to result in more mixing [29]. The scalar variance production term $\overline{uT}\frac{\partial\overline{T}}{\partial x} + \overline{wT}\frac{\partial\overline{T}}{\partial z} + \overline{vT}\frac{\partial\overline{T}}{\partial y}$ is expected to be dominated by the vertical component because the vertical temperature gradient is larger than the lateral temperature gradient except at the front of the jump.

Figure (2.20) shows the trend of each of the mixing terms compared to the amount of expansion, m, as well as the average amount of turbulent kinetic energy in each case for $m = 0$ (straight channel) to $m = 0.23$ (maximum expansion). The mixing is decomposed into each mixing component: Lateral, M_L (in the y-direction), Horizontal, M_H (in the x-direction), Vertical, M_v and then combined into a total mixing trend. Furthermore, turbulent kinetic energy (TKE) for the jump in each case is integrated from a to b. This gives an estimate of the turbulence produced by the jump to be compared between cases.

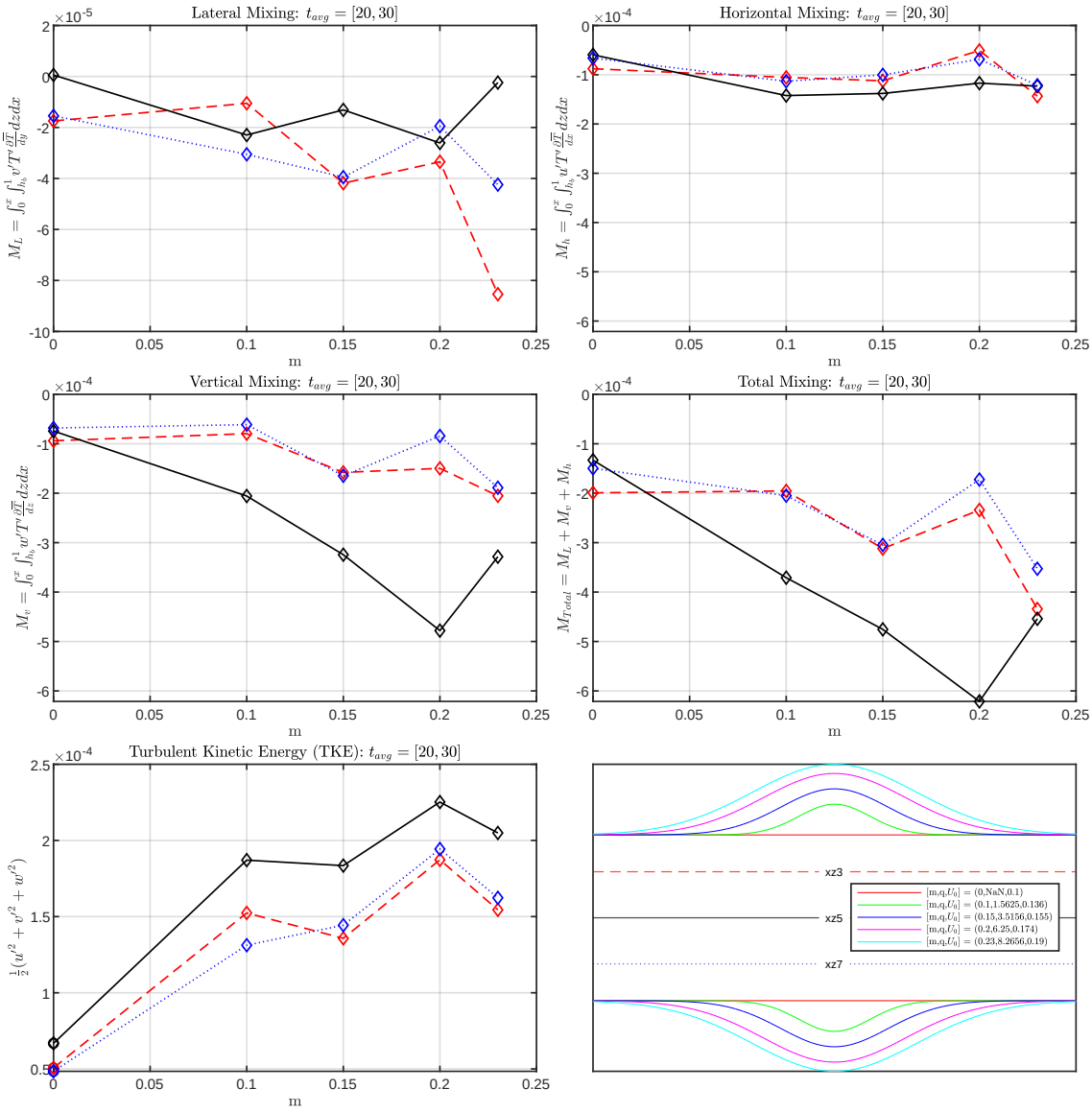

Figure 2.20: Simulation **Set A** mixing trend for time average scalar variance quantities from $t = 20$ to $t = 30$ for each component of mixing. Turbulent kinetic energy is also plotted comparing the trend to increasing m. Black line indicates channel center, while red and blue indicate off-center regions. Amount of expansion is increased with increasing m.

The results show that the amount of mixing (the magnitude of scalar variance production) increases for cases with a larger expansion (m). Lateral mixing is an order of magnitude less than the other mixing components; however, the amount of mixing off-center ($xz3$ & $xz7$) does trend toward more mixing as m increases, which is expected given the increasing vorticity

shown in Figure 2.18. Furthermore, given the constant sill velocity, increased horizontal mixing isn't expected, and thus the dominant mixing component is in the vertical. As previously mentioned, vertical mixing has been shown to be the dominant mixing component in interaction with internal tides and topography [61]. The combination of the components of mixing results in an overall trend of increased mixing with increased channel width. Given that the velocity remains constant over the sill, these results indicate that mixing is effected with a changing channel geometry.

Additionally, while the overall mixing through the jump increases as the amount of expansion increases the amount of mixing in the thalweg shows a considerable difference to that of the off-center planes. Therefore, the amount of mixing computed will depend on the location across the channel. This is significant, given Gregg & Pratt hypothesized the jump in Hood Canal may be three dimensional [7], and thus only considering one part of the channel may not fully characterize the flow. Finally, the amount of turbulent kinetic energy produced by the jump in each case is plotted, and shows a small trend upward. Comparing all cases to the straight channel case ($m = 0$), there is a significant increase in TKE as a result of changing the channel geometry, while the increase in the center of the channel is the largest. Since the u velocity is highest in the center of the channel, this is the expected result, as turbulent kinetic energy is dependent on all of the velocity fluctuations.

The goal of this section was to compare hydraulic jumps in a channel of increasing width, while isolating the effect of the geometry change by maintaining a constant average velocity at the sill. This caused the jumps to occur in a similar location (Fig. 2.15) and allowed investigation into how the geometry of the channel affects mixing and turbulence. The results show that larger expansions around a sill correspond to increased mixing, turbulence, and vorticity, due to the following factors:

- Stratification, varying velocities in top and bottom layers, and vertical turbulence caused by the increasing expansion in the region of the jump contributes to the vertical mixing, shown to be dominant.

- Increasing the channel width allows more room for lateral vorticies to develop as velocities diverge downstream of the sill and causing more rotation as m increases, and lateral mixing in the off-center increases, while the thalweg is shows no trend in lateral mixing.

- Due to the channel geometry, and constant sill velocity, vortex intensity is localized toward the channel thalweg, thus resulting in the dominant vertical mixing along the channel center.

Therefore, the net effect of the increasing expansion at the sill is a trend towards more mixing in the channel. The next section will consider a similar set of channel geometries with a constant volume flow rate, allowing the sill velocity to adjust due to the increasing expansions.

Set B - Constant Expansion with Constant Inlet Velocity

Simulation **Set B** maintains a constant volume flow rate for all simulations, which results in different average velocities at the sill for simulations with different sized expansions. The results therefore include the effect of velocity change at the sill, with parameters outlined in Table 2.2. That is, all simulations were run with a constant inlet velocity, $U_0 = 0.1$, such that the velocity at the sill varies according to the amount of expansion. In this case the, smallest expansion, $m = 0.1$, is not large enough for coherent the vorticities to form and therefore the location of the jump is similar to the straight channel interface height.

Set B - *Constant expansion rate and variable sill velocity*								
m	q	U_0	U_{sill}	$xz3$	$xz5$	$xz7$	t_1	t_2
0.228	8.2656	0.1	0.13	0.35	0.5	0.65	$t = 30$	$t = 39$
0.2	6.25	0.1	0.17	0.35	0.5	0.65	$t = 31$	$t = 39$
0.15	3.5156	0.1	0.25	0.35	0.5	0.65	$t = 30$	$t = 50$
0.1	1.5625	0.1	0.2	0.35	0.5	0.65	$t = 43$	$t = 51$
0	NaN	0.1	0.3	0.35	0.5	0.65	$t = 20$	$t = 35$

A comparison of interface heights (Fig. 2.21) for each case shows that the the jump location occurs much further downstream for $m = 0.1$ than for other cases.

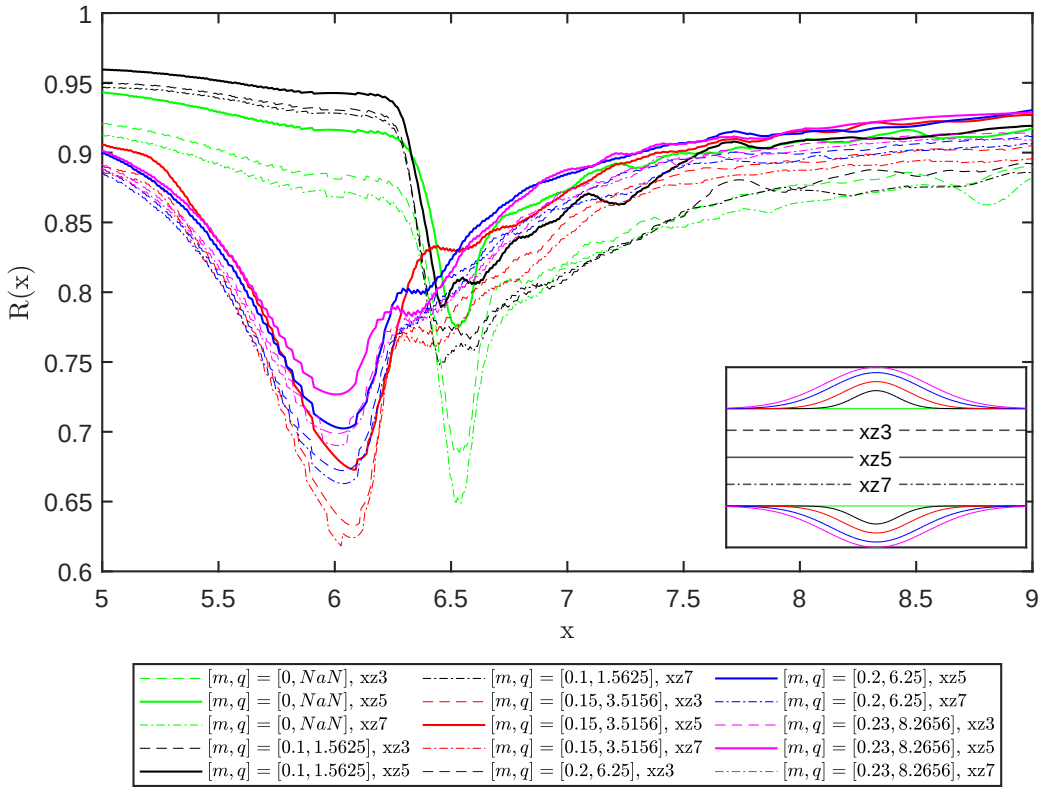

Figure 2.21: Set B Interface heights, $R(x)$, for expansion m at transverse channel positions $y = 0.35$ ($xz3$), $y = 0.5$ ($xz5$) and $y = 0.65$ ($xz7$). Plot of corresponding topographies (bottom right) where solid lines indicate channel center interface height, and dotted lines indicate off center.

Here, the velocity through the sill is relatively small for $m = 0.1$, shown in Figure 2.22 as the upstream adjustment results in a thicker, and therefore slower, lower layer. Therefore, this upstream adjustment, and the effected lower layer velocity which is similar to the straight channel case, as well as the smaller channel width compared to higher values of m, causes the jump to occur further downstream for $m = 0.1$.

For the subsequent cases, the depth of the interface increases for increasing m (expansion). A similar result as the previous simulation set develops for the interface heights as the position the jump occurs relative to the cross-sectional area, and the average sill velocity cause the interface heights to be higher, and occur further upstream as the amount of expansion increases.

The increasing expansion, causes the upstream velocity to be reduced and thus reduce the velocity resulting in the jump position moving backward slightly for larger m.

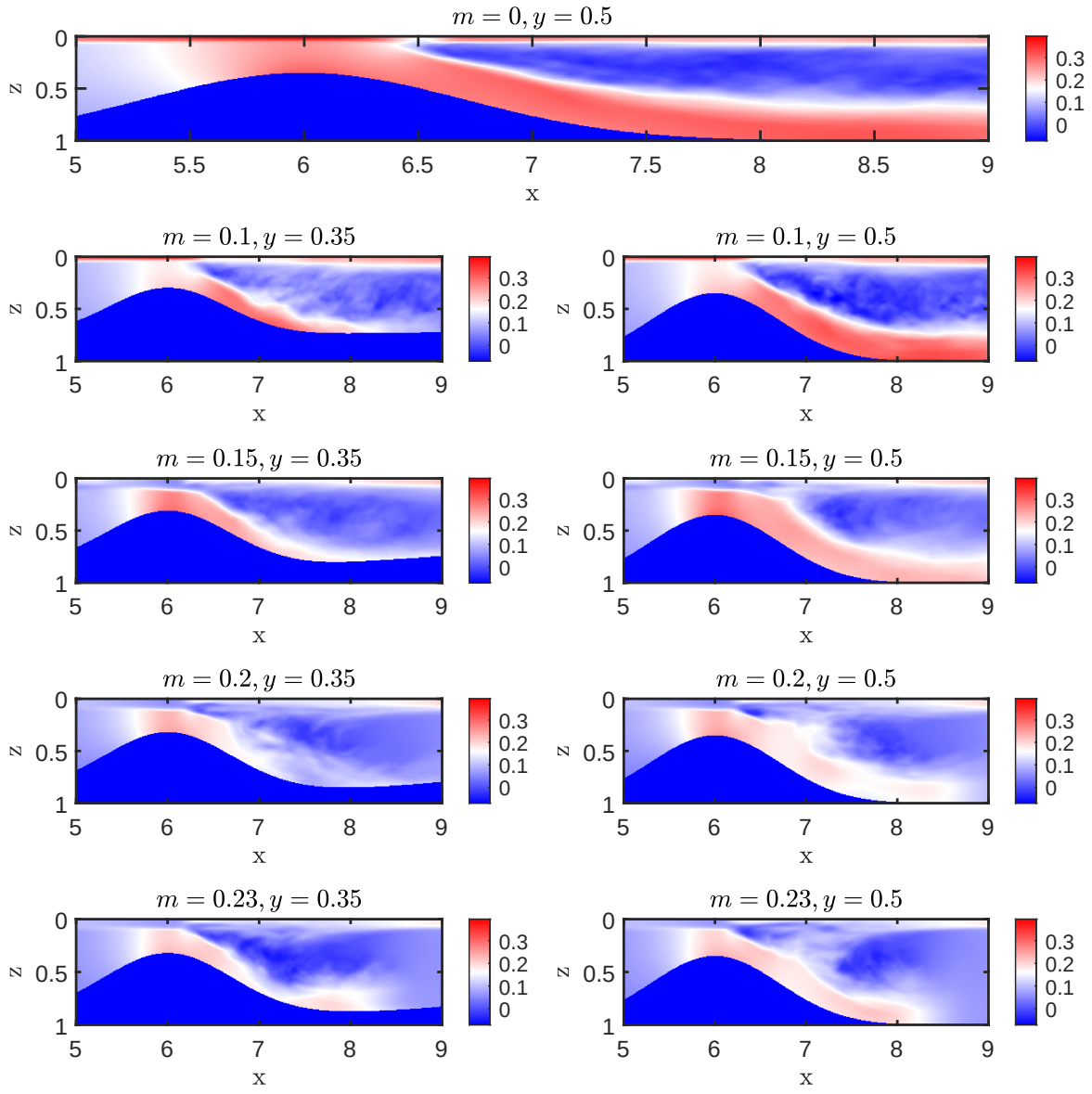

Figure 2.22: Set B time averaged u velocity for cases $m = [0, 0.1, 0.15, 0.2, 0.23]$ in the along channel direction for data along the thalweg ($y = 0.5$) and off-center ($y = 0.35$) with a constant inlet velocity $U_0 = 0.1$ (right to left). Channel plots for amount of expansion increase from top-bottom.

Figure 2.22 shows the sill velocity is reducing for larger expansions (m) due to the cross-sectional area increasing upstream of the sill (Fig. 2.7) for each. Velocity differences between the thalweg and off-center slice are also shown which indicates there is vorticity; however the

velocities are small and the vorticities should be less intense as m increases and the expansion becomes larger. This is discussed in more detail in Figure 2.27 on page 84.

The amount of mixing caused by the jump is calculated in the same manner as the previous section. The trend of mixing with increasing values of m is shown in Figure 2.23 over times $t = 20$ to $t = 50$. The mixing contributions are again decomposed into lateral, vertical, and horizontal, and then combined into the total amount of mixing. Furthermore, the turbulent kinetic energy is also calculated.

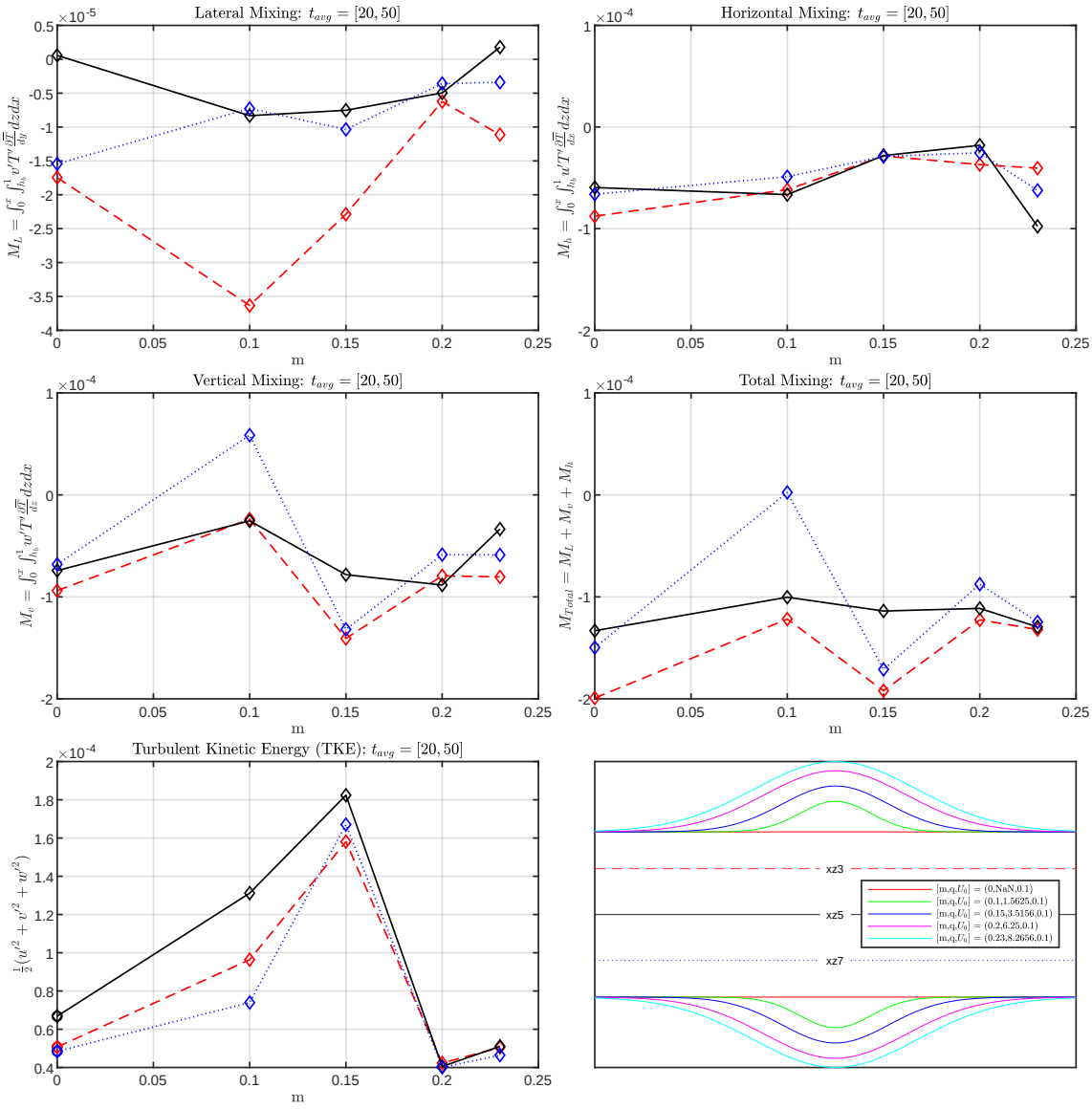

Figure 2.23: Simulation **Set B** trend for each componet of mixing (vertical, horizontal, lateral and total) for increase *m* with a sill velocity that decreases with a larger expansion. Black line indicates center channel mixing, while red and blue indicate off center.

The total mixing along the thalweg shows no trend, and this is expected because the velocity decreases for larger expansions. Lower velocity jumps result in less mixing which counteracts the effects of channel width variation, and the two combined result in no trend. Likewise, there is more velocity variation between cases of *m* for mixing between the off-center compared to the thalweg, which is likely a result of the bulk of the rotation occurring in these areas, rather

than in the center of the channel. The turbulent kinetic energy is also plotted and corresponds to the velocity fluctuations through the jump. For case $m = 0.15$ the velocity and therefore turbulent kinetic energy, over the sill is highest. The higher TKE doesn't result in more mixing because the turbulence can occur in a homogenous region of fluid and therefore doesn't modify the density.

In this set, when the effect of the velocity over the sill is not removed (like **Set A**) the velocity at the sill is reduced as the amount of expansion increases, and thus less intense and less coherent vorticities form. When the velocity changes due to the geometry, isolating the specific event-cause relationship is difficult as the position of the jump moves, upstream adjustment occurs, and vorticity is effected by the position of the jump and the size of the expansion, and thus there is scatter in the results. However, what is evident between **Set A** and **Set B** is the effect of the reduced velocity caused by the expansion counteracts the increase in mixing caused by the expansion, and thus no trend in mixing occurs.

Set C - Variable Expansion Rate with Constant Inlet and Sill Velocity

Simulation **Set C** investigates a constant m value of $m = 0.15$, while varying the rate of expansion (or the approach slope of the coastline toward the sill). Larger values of q represent a more gradual slope, while smaller q is more abrupt. The average velocity at the sill is constant between cases.

Set C - *Variable expansion rate and constant sill velocity*								
m	q	U_0	U_{sill}	$xz3$	$xz5$	$xz7$	t_1	t_2
0.15	8.2656	0.1	0.25	0.35	0.5	0.65	$t = 20$	$t = 30$
0.15	6.25	0.1	0.25	0.35	0.5	0.65	$t = 20$	$t = 30$
0.15	3.5156	0.1	0.25	0.35	0.5	0.65	$t = 30$	$t = 55$
0.15	1.5625	0.1	0.25	0.35	0.5	0.65	$t = 20$	$t = 30$

Interface heights are compared in Figure 2.24 to show the changes in the jump position between varying cases of q, while the straight channel case is shown as a reference for how a channel with no expansion causes the jump position to move upstream.

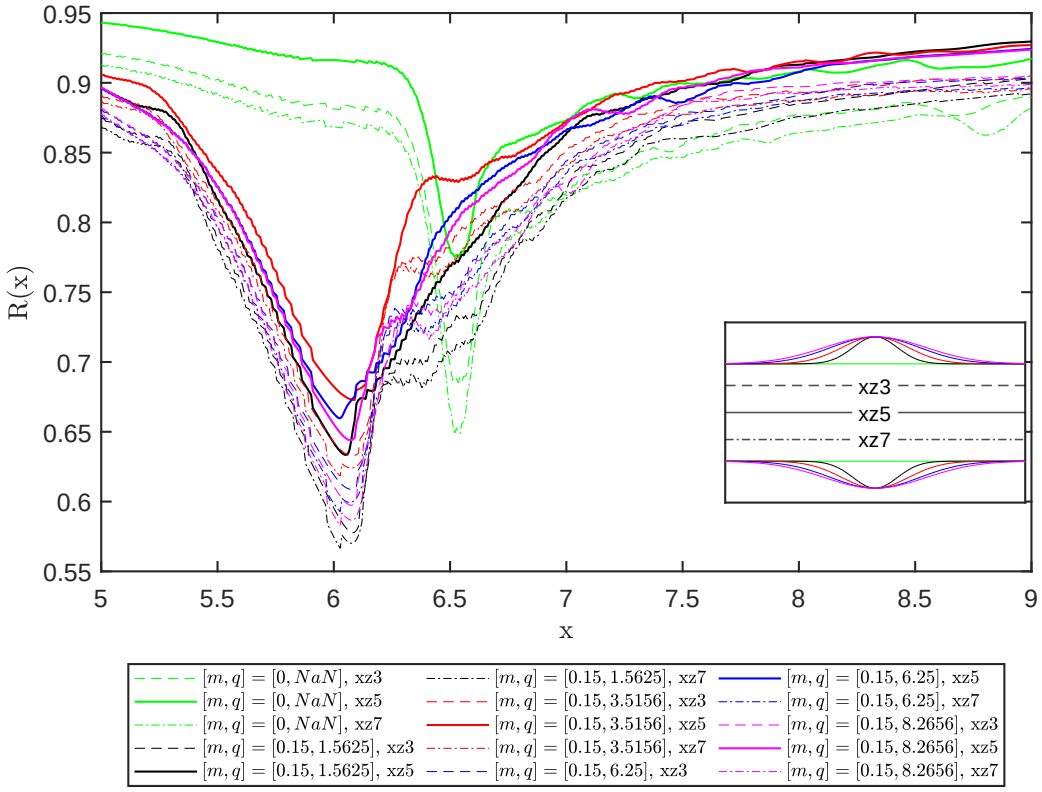

Figure 2.24: Set C interface heights with variable rate of expansion (q) and constant amount of expansion ($m = 0.15$) shown for each case of q. Simulation domain is shown (bottom right) for which the amount solid lines indicate channel center, while dotted lines indicate off-center.

The interface heights for each case show that the jump remains in approximately the same position for each, with the depths changing based on the interaction with the topography and sill height, similar to the other sets. This is expected given the cross-sectional area at the sill crest is constant for all cases compared to **Set B** where the jump position moves backwards as the upstream velocity is reduced. Additionally, jump structure across the channel remains symmetric for both *xz*3 and *xz*7 as there is very little change in the interface height between these data slices.

Velocity in the *xz*, along channel direction, is plotted in Figure 2.25, and shows that the velocity fields are simular for all cases for the slice along the thalweg. The off-center slices show slightly more variation in velocity between cases since they are closer to the side boundary,

which changes position between cases.

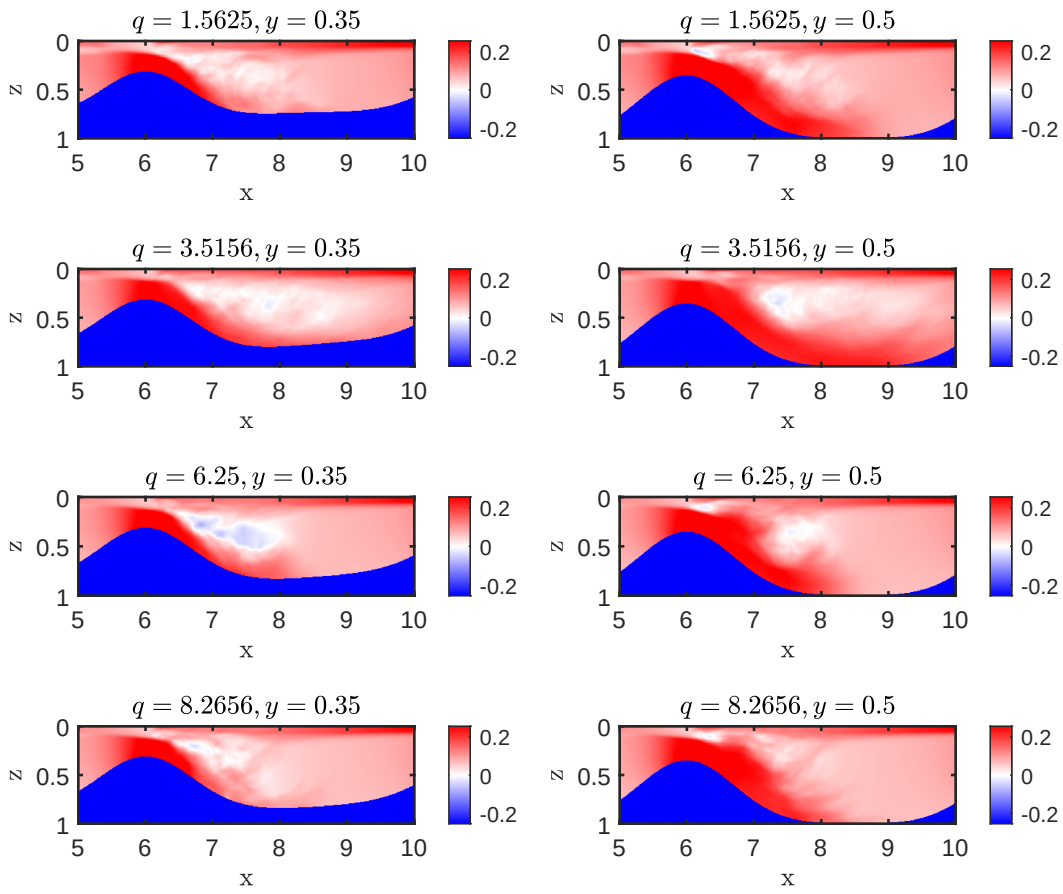

Figure 2.25: Set C along channel average u velocity for a constant $m = 0.15$, with varying rates of expansion, $q = [1.5625, 3.5156, 6.25, 8.2656]$ along the thalweg ($y = 0.5$) and off-center ($y = 0.35$) (right - left).

Due to the varying downstream rate of expansion, the velocity varies in the off-center position between cases. Therefore, a trend of mixing in the off-center position of the channel is expected.

Quantifying the mixing rates with the same approach for previous simulation sets yields the results shown in Figure 2.26.

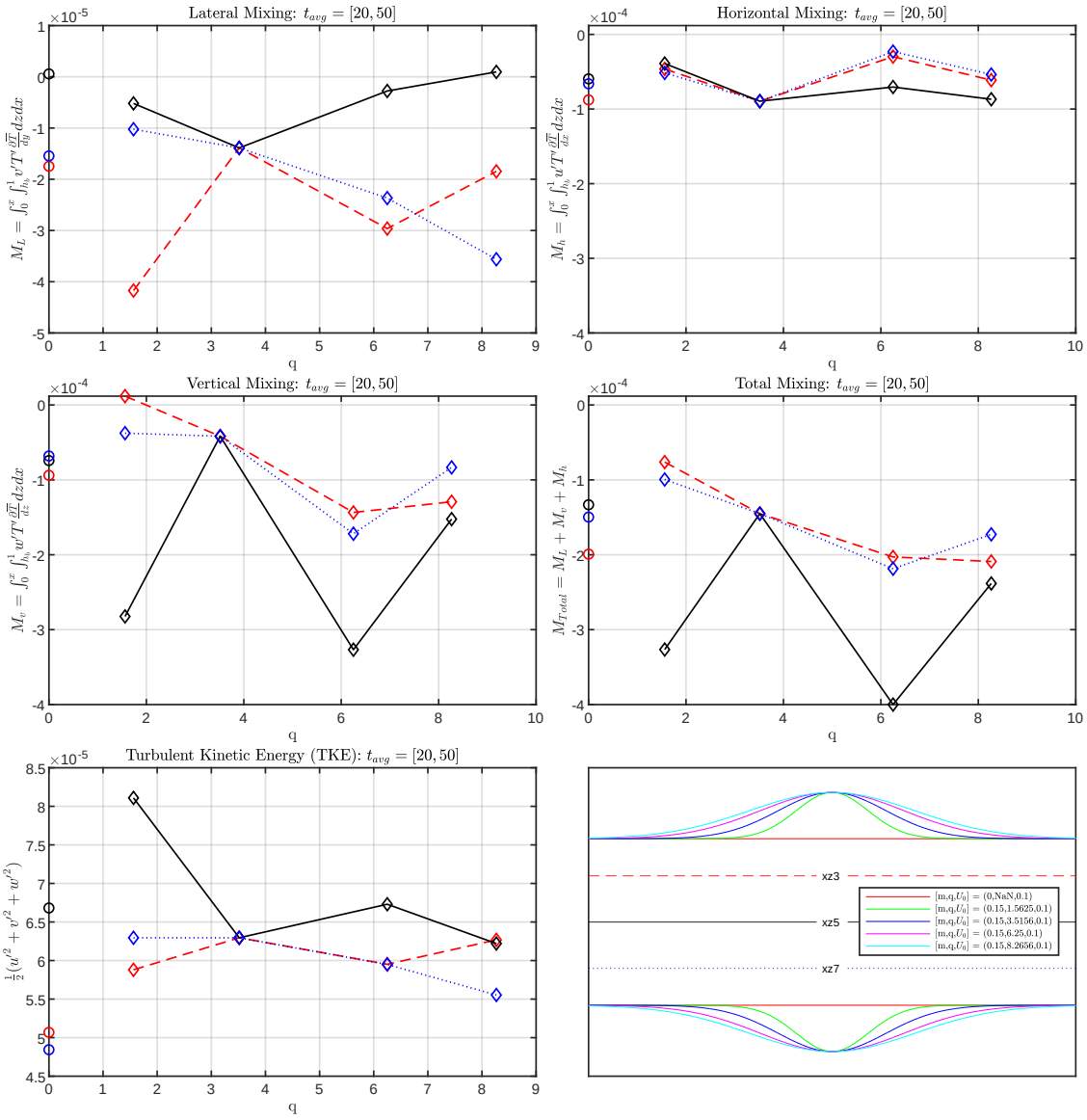

Figure 2.26: Set C mixing components (vertical, horizontal and lateral) for variable rate of expansion (q) and constant amount of expansion (m). Topography plot indicates different simulation domains (bottom right) with solid black line the center data, and dotted red and blue off center.

Lateral mixing along the thalweg is smaller than the mixing off-center, while vertical mixing shows a trend of increasing mixing with increasing u off-center, the thalweg does not show a trend. Therefore the results indicate that an increase in q (causing a decrease in the rate of expansion) results in increased mixing in the off-center region of the channel.

Qualitative Comparison of Expansion Cases

To better understand the effect of the geometry on the flow pattern, the average vorticity in each simulation is compared qualitatively.

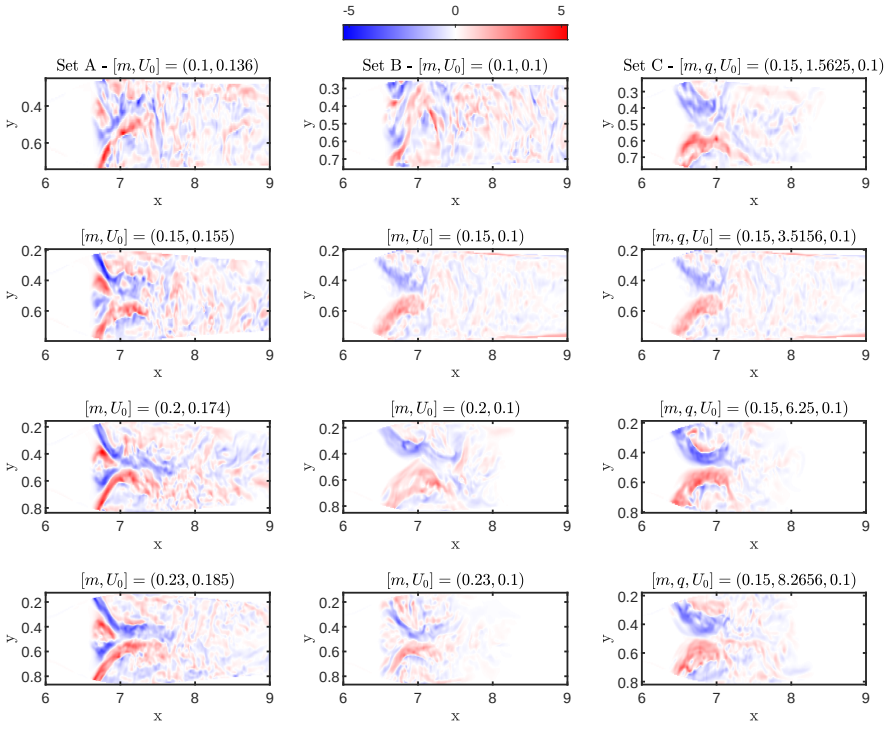

Figure 2.27: Comparison of vorticity, ω for simulation sets A (left), B (middle), C (right) for small m (top row) to large m (bottom row) (for set A and B) or a small to large q for set C. Plots are shown across the channel at a depth of 0.3.

Figure 2.27 shows the comparison between **Set A** and **Set B**, showing that **Set B** has less intense vorticity due to the velocity reduced by the sill, and the intensity of the vorticity is localized in the off-center portion of the channel, rather than localized along the thalweg as seen in **Set A**. The vorticity for **Set A** is localized toward the center of the channel, as previously outlined with the intensity increasing as m increases. Due to the constant average sill velocity, the expanding channel, and the parabolic profile, the localized vorticity in **Set A** resulted in the dominant mixing along the thalweg, with mixing increasing as the expansion increases. Conversely, **Set B** upstream velocity was reduced by the expansion as the flow begins to diverge

upstream of the sill, and thus the intensity of the re-circulation is reduced due to the velocity reduction. This results in the velocity reduction counteracting the increased mixing due to the geometry change. Finally, **Set C** shows the intensity and structure of vorticies generally increases as q increases and the rate of expansion decreases. These vorticies are less intense than **Set A** due to a lower average sill velocity, however there is a trend in the off-center mixing as the vortex intensity is localized most toward these regions of the channel, rather than along the thalweg as in **Set A**. This is likely a result of the maximum channel width at the sill not changing, and thus there is minimal disparity between upper and lower velocities as the parabolic profile of the channel at the sill is the same for all cases.

Therefore, generally for these expansion simulations, as the width of the channel at the sill increases, the amount of mixing also increases due to the geometry causing vorticy localization near the channel center to increase, while a more gradual slope allows more coherent vorticies to develop in the off-center region, resulting in a trend of more mixing in these zones.

The internal wave speeds are calculated using the Taylor-Goldstein equation (Eq. (2.13), and the continuous velocity and density profiles:

$$(U-c)\left(\frac{\partial^2}{\partial z^2}-k^2\right)w - U_{zz}w + \frac{N^2}{U-c}w = 0. \tag{2.13}$$

Here, $\phi = \phi(z)$ is the vertical structure of the internal waves, which is assumed to have the wave solution, $W = w(z)e^{ik(x-ct)}$. In the long-wave limit, $k \to 0$ gives the equation for the fastest moving waves in each direction,

$$(U-c)\frac{\partial^2\phi}{\partial z^2} - U_{zz}\phi + \frac{N^2}{U-c}\phi = 0. \tag{2.14}$$

The Taylor-Goldstein equation has been used by Gregg & Pratt [7] for calculating wave speeds in environmental flows, and the wave speeds here are calculated based on a code developed by Ogden [6]. The equation applies to a horizontal flow with a vertically varying velocity and density profile in a channel with a parallel top and bottom. This invites some error, as the

u velocity in a channel with a sill is only one component of the velocity, and internal waves aren't strictly horizontal; however, it is the best approach available for wave speed estimation and is likely an underestimation of the wave speeds.

Calculating wave speeds for each case give an improved quantification of the hydraulic characteristics of the flow. For each case, minimum and maximum wave speeds were calculated considering time averaged velocity profiles, $u(z)$ and the buoyancy frequency, $N(z)$. Long-wave modes, occur in pairs with speeds c_{-j} and c_j ($j \geq 1$) where $j = 1$ corresponds to the first mode internal wave, which is the fastest.

For any particular mode, criticality of the flow can be determined at any section across the channel. If $c_{-j}c_j < 0$ waves propagate in opposite directions and the flow is considered sub-critical with respect to j. Likewise, supercritical flow occurs when wave speed propagation is in the same direction, or $c_{-j}c_j > 0$. For a hydraulic jump to occur, transition from supercritical to sub-critical must occur. Given that the minimum wave speed (c_-j) determines criticality, as $c_j > 0$ for all cases, Figures 2.28 & 2.29 show c_2 along the channel for each case of m and for each set of simulations. Hydraulic jumps for both sets of simulations were mode 2. Since Gregg & Pratt showed no change in criticality where re-circulation was high, indicating three dimensional flow [7]. Similarly, the sign of c_2 changes across the width of the channel downstream of the jump, with c_2 often becoming positive along the thalweg while it remains negative closer to the channel sides.

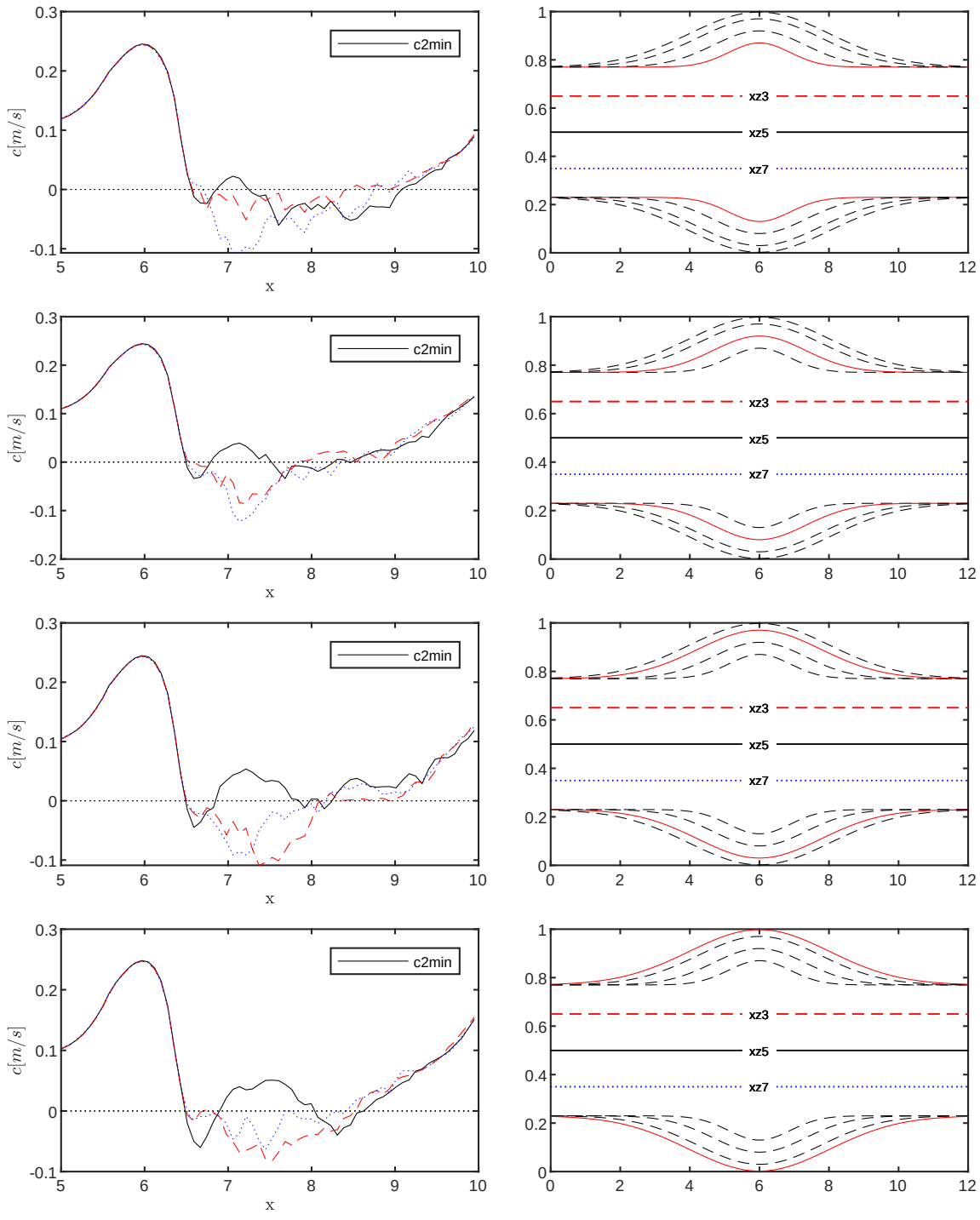

Figure 2.28: Mode 2 wave speeds, c, for **Set A** simulations along channel slices $xz3$, $xz5$ & $xz7$ (left). Black solid line corresponds to center data, while red and blue dotted lines correspond to off center. Topographies are plotted corresponding to each simulation case highlighted in red (right).

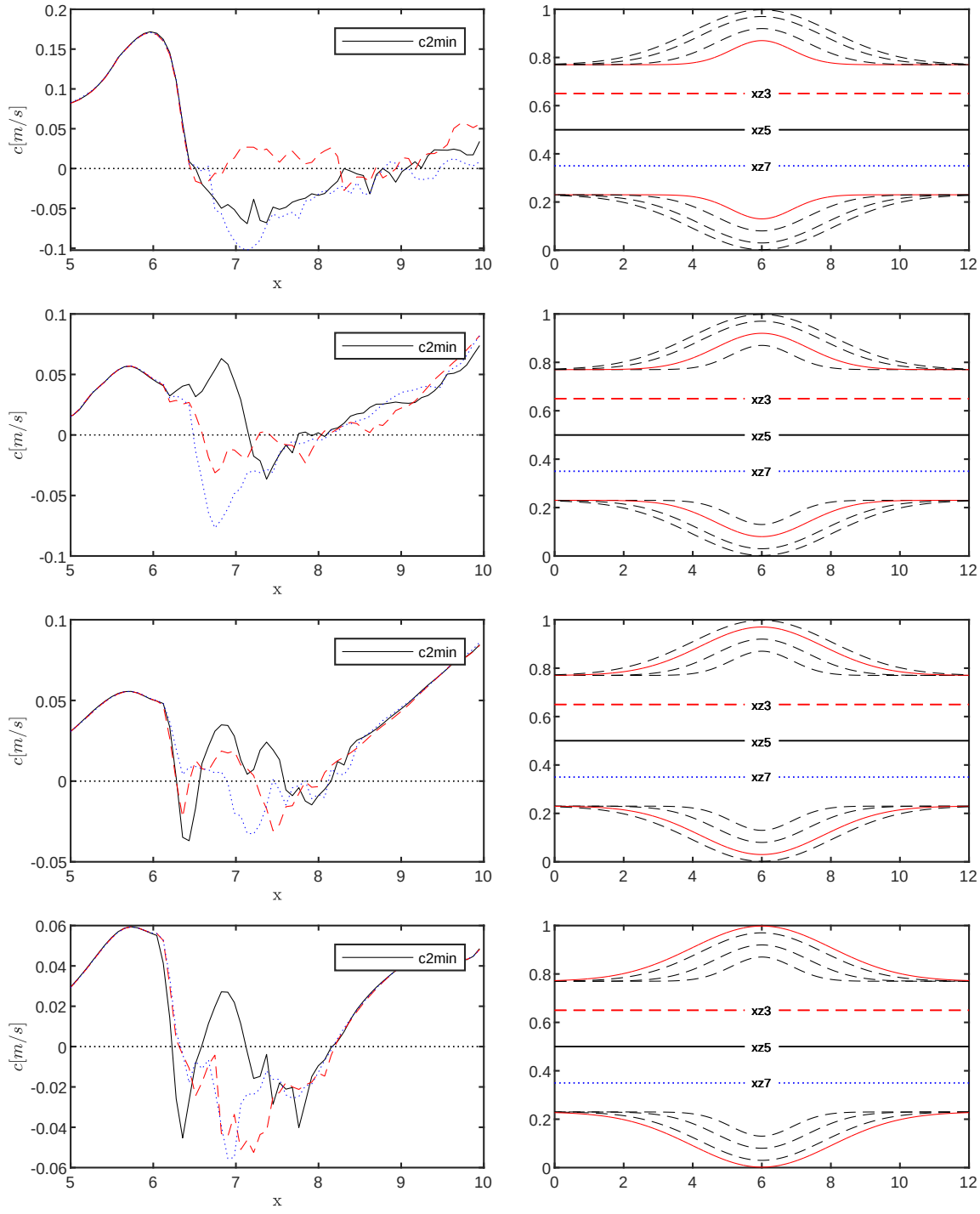

Figure 2.29: Mode 2 wave speeds, c, for **Set B** simulations along channel slices $xz3$, $xz5$ & $xz7$ (left). Black solid line corresponds to center data, while red and blue dotted lines correspond to off center. Topographies are plotted corresponding to each simulation case highlighted in red (right).

2.4.2 Channel Contraction

Set D - Constant Contraction with Constant Sill Velocity

Set D - *Constant Contraction rate with constant sill velocity*								
m	q	U_0	U_{sill}	$xz3$	$xz5$	$xz7$	t_1	t_2
-0.15	3.5156	0.044	0.33	0.35	0.5	0.65	$t = 20$	$t = 40$
-0.1	1.5625	0.063	0.33	0.35	0.5	0.65	$t = 20$	$t = 30$
0	NaN	0.1	0.33	0.35	0.5	0.65	$t = 20$	$t = 35$

In order to further understand the interactions between channel geometry, velocities, and mixing occurring in hydraulic jumps, studying contracting channels is also necessary to understand how the solutions differ or remain similar. Expanding on work completed by Ogden & Ganotaki [73], Table 2.4 outlines the parameters used for simulating hydraulic jumps through various amounts of contraction with a constant velocity across the sill. Due to the geometry of the channel and the smaller cross-sectional area, disturbances at the inlet propagate into the jump region too quickly, and therefore a sufficient averaging period is not always able to be obtained. Only two cases of m are analyzed in order to compare the results to the expansions from **Set A**.

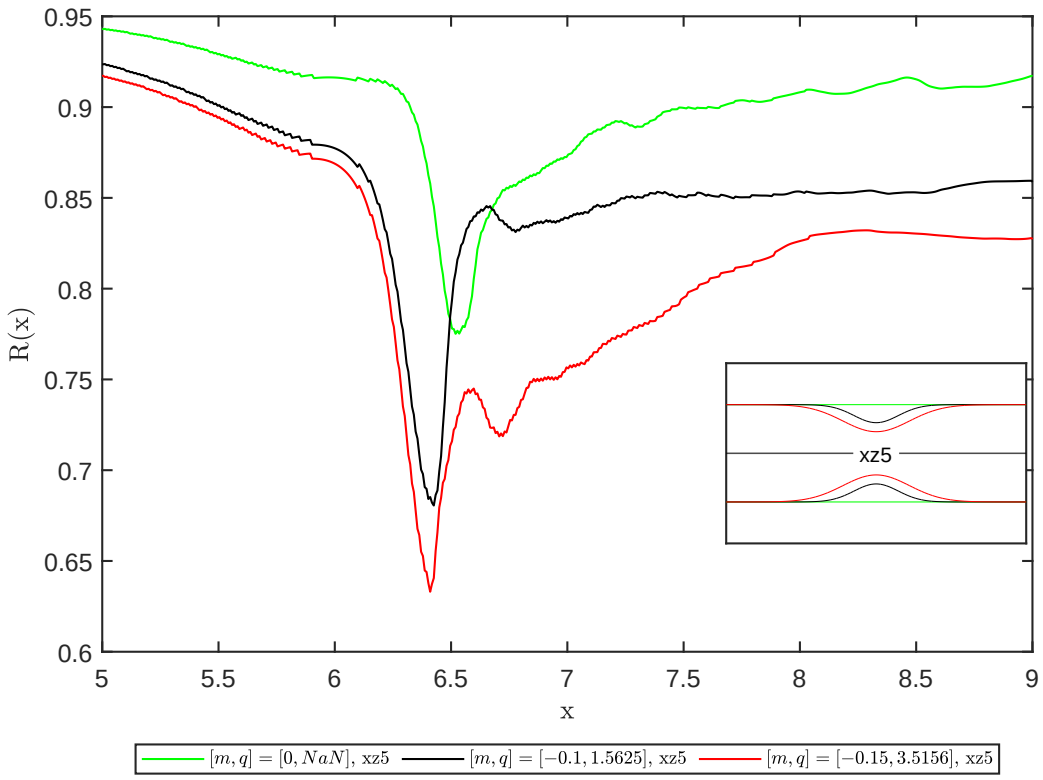

Figure 2.30: Set D interface heights, $R(x)$, for increasing contractions, m, at a constant rate, q = [1.5625, 3.5156] and constant velocity across the sill. Corresponding topographies (bottom right) relate to coloured lines and are plotted for data along the channel center.

Interface heights for decreasing values of m (smaller amount of contraction shown in Figure 2.30) show a trend toward a deeper jump for a smaller value of m. However the structure of the jump appears to be very similar downstream. Due to the velocity at the sill, U_{sill} = 0.33, the jump occurs in a similar position to the expansion cases from **Set A** results, however the interface height is much larger. The cross-sectional area in these cases increases downstream of the sill, instead of increasing and then contracting, as the cases in the previous section did. Therefore the combination of the velocity, sill height and downstream features causes the jump to quickly transition to a lower downstream velocity.

All mixing and turbulence quantities are calculated over the averaging period of t = 20 to t = 30 and shown in Figure 2.31.

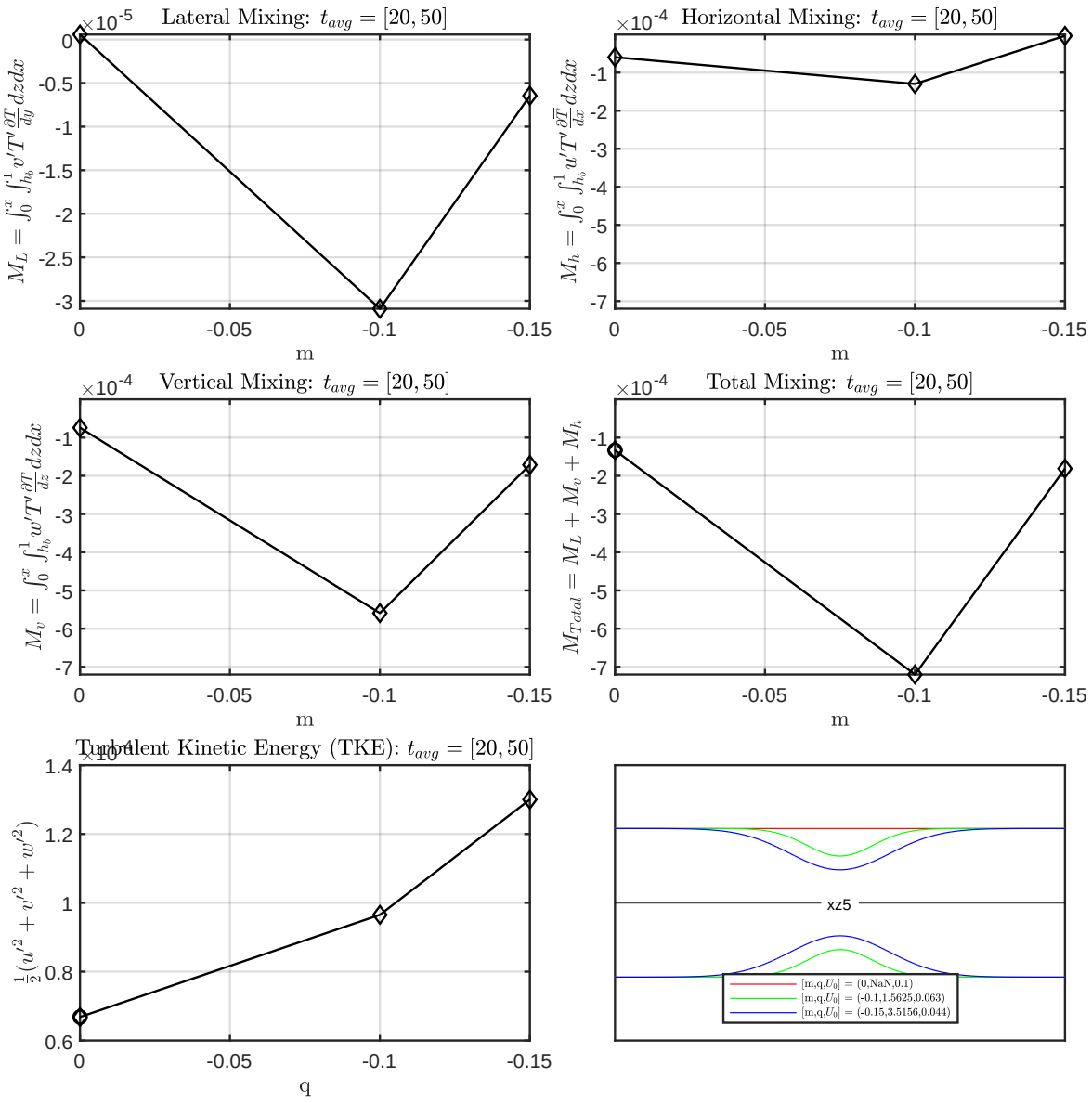

Figure 2.31: Set D - Constant contractions with variable inlet velocity mixing trend for all mixing components (Lateral, vertical and horizontal) as well as total mixing and TKE. Data plotted for channel center for increasing amounts of contraction.

Due to the narrow width of the channel, only $y = 0.5$ ($xz5$) mixing values are quantified; the other planes lie mostly outside of the channel. While there are fewer cases to compare, results do not suggest a trend. The vorticity is discussed in context with other contraction cases on page 96. Given the jump location, the constant rate of expansion, and the geometry affects the amount of vorticity, thus the mixing is affected, however a clear trend is not shown.

Set E - Constant Contraction with Variable Sill Velocity

Simulation **Set E** is similar to **Set B** as the velocity across the sill will vary, given a constant volume flow rate at the inlet. In these cases, the contraction will cause an increase in the velocity through the sill, and thus velocities for higher values of m will be sufficiently larger than all other sets of simulations. The parameters used for the simulation setup are described in Table 2.5.

Set E - *Constant Contraction rate with variable sill velocity*								
m	q	U_0	U_{sill}	$xz3$	$xz5$	$xz7$	t_1	t_2
-0.2	6.25	0.1	1	0.35	0.5	0.65	$t = 20$	$t = 40$
-0.15	3.5156	0.1	0.65	0.35	0.5	0.65	$t = 20$	$t = 40$
-0.1	1.5625	0.1	0.48	0.35	0.5	0.65	$t = 20$	$t = 30$
0	NaN	0.1	0.33	0.35	0.5	0.65	$t = 20$	$t = 35$

Interface heights (Fig. 2.32) for simulation **Set E** (Table 2.5) are as expected.

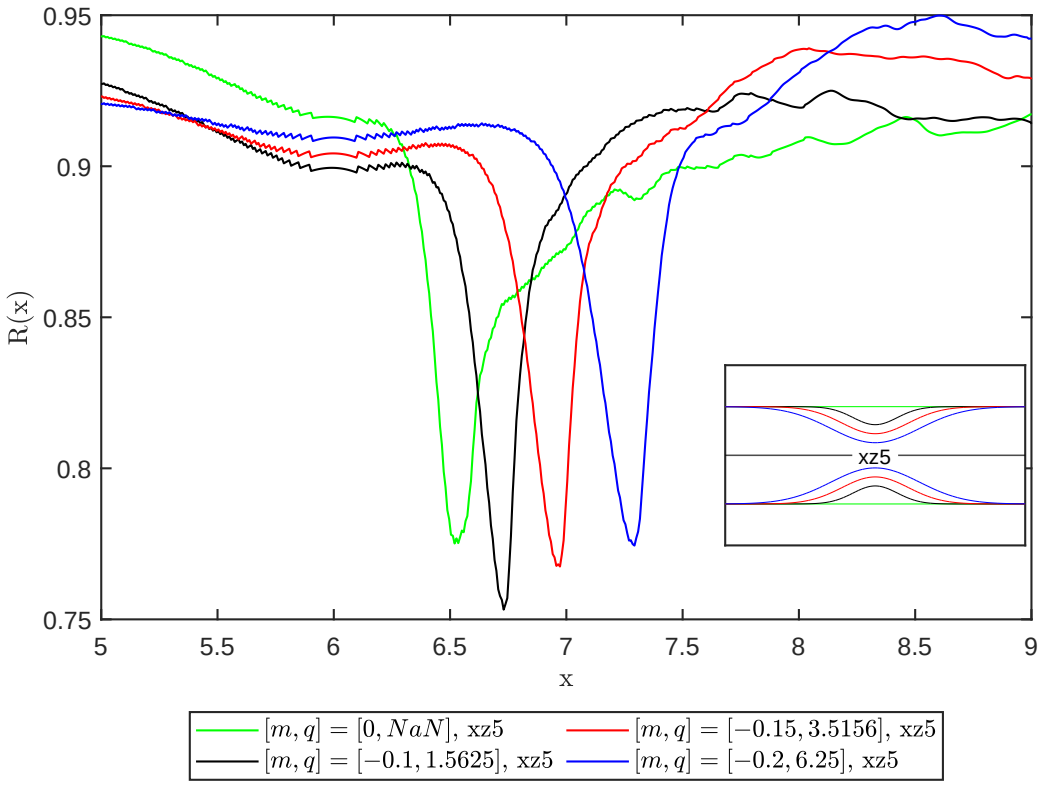

Figure 2.32: Set E interface heights, $R(x)$, for increasing contractions, m, at a constant rate, $q = [1.5625, 3.5156, 6.25]$ and variable velocity across the sill. Corresponding topographies (bottom right) relate to coloured lines and are plotted for data along the channel center.

Due to the velocity increase over the sill and through the contraction, the interface heights show that the position of the jump moves downstream for increasing magnitudes of m. Furthermore, the height of the interface is greater for larger $|m|$, and thus more turbulence and mixing is expected compared to set B, where the height of the jump decreased with an increase in m.

Likewise, the velocity just ahead of the jump is shown in Figure 2.33 along with the changing position of the jump. An upward trend is shown, along with a changing position for which the jump occurs. Given the substantial increase in velocity, and the dominance this term has on the vertical scalar variance production, mixing is expected to be largest with increasing velocity.

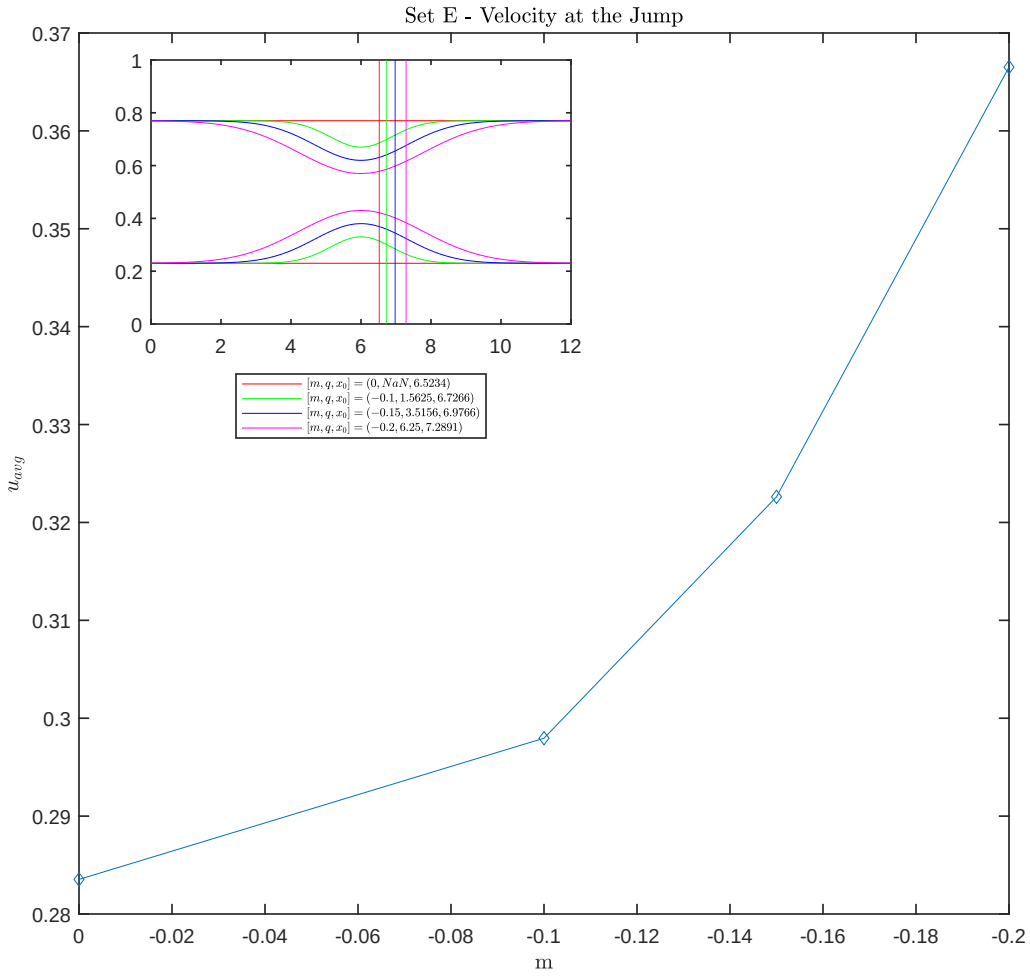

Figure 2.33: u_{avg} just ahead of hydraulic jump for Set E simulations. Results are plotted for increasing amounts of contraction. Corresponding topographies (top left) show colored lines relating to position of jump and corresponding topographies.

The mixing is quantified in Figure 2.34 and shows an increase in mixing with decreasing m, consistent with what would be expected given previous results. As the velocity increases, so does the amount of vertical mixing along the center line of the channel.

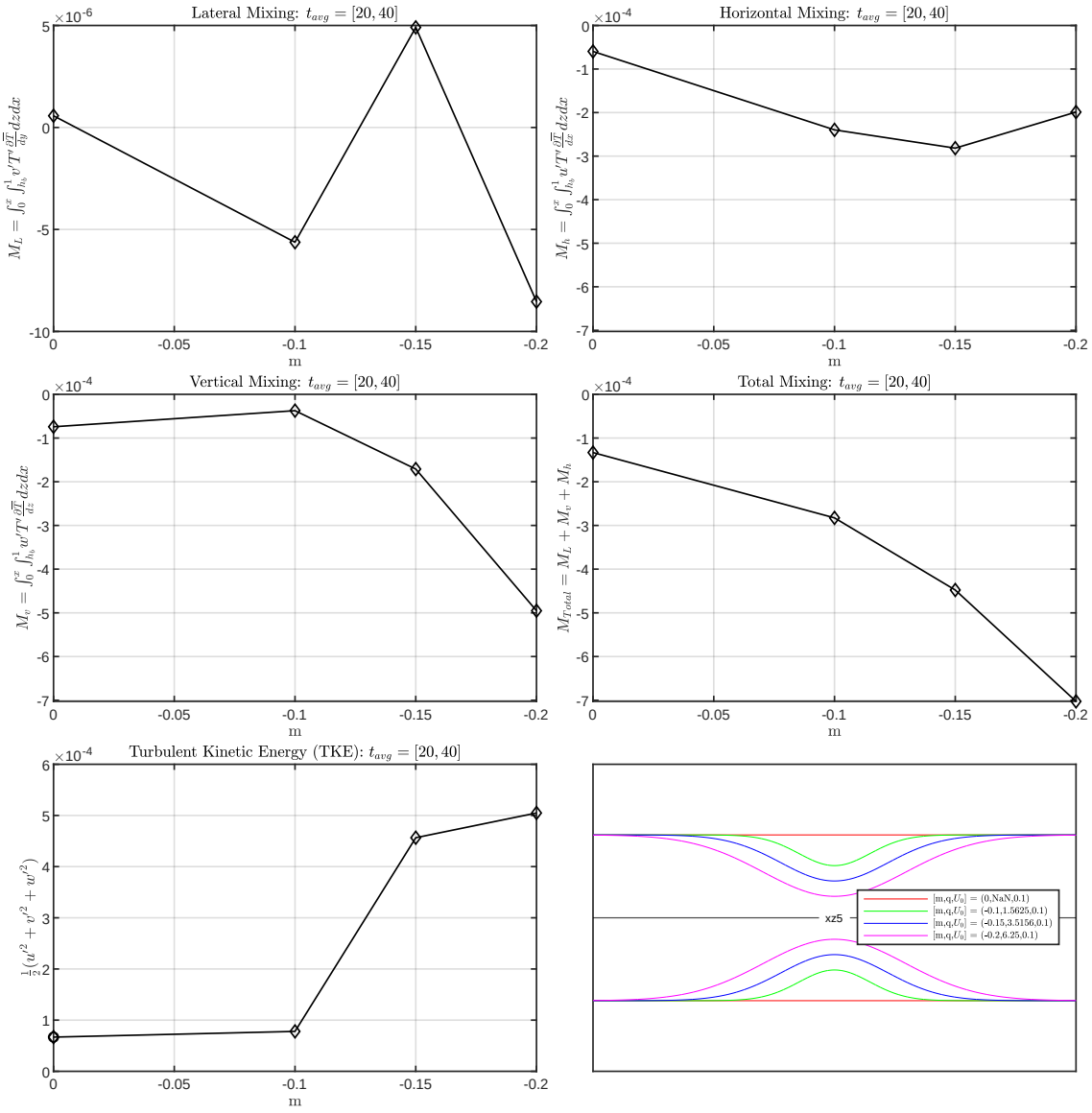

Figure 2.34: Set E - Constant contractions with constant inlet velocity mixing trend for all mixing components (Lateral, vertical and horizontal) as well as total mixing and TKE. Data plotted for channel center for increasing amounts of contraction.

Additionally, horizontal mixing shows no change as the magnitude of *m* increases, lateral mixing is two orders of magnitude smaller than vertical and turbulent kinetic energy shows an overall upwards trend. Considering vertical mixing is dominant, this indicates that overturning is high and vorticies in the lee of the sill and contraction are expected to be small.

A comparison of the vertical vorticity for all (Figure 2.35) contraction cases verifies the

above, as the jump is occurring in an expanding region downstream, rather than a contracting zone like in sets A - C.

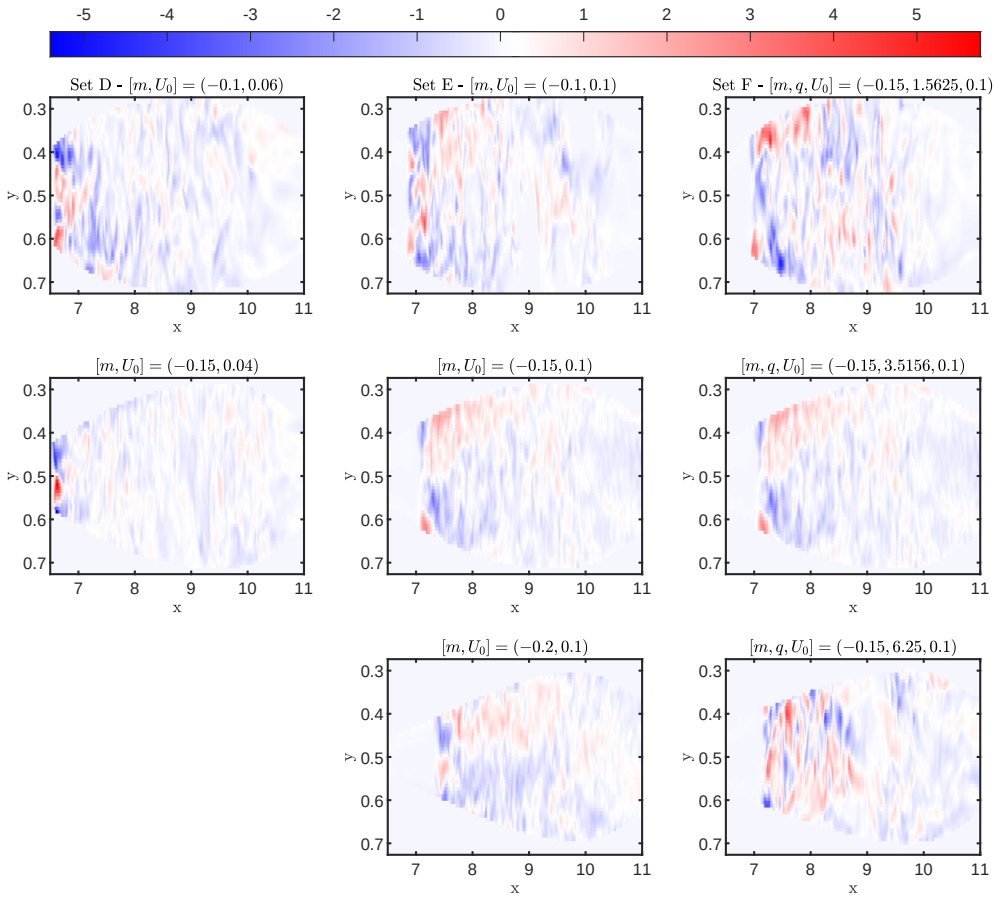

Figure 2.35: Comparison of vorticity, ω_z, for simulation sets **D, E & F** (left - right) plotted at a depth of 0.3 in the across channel slice. Smallest contraction amount (top row) to largest (bottom row) is shown for each case.

Furthermore, the vorticity for all cases of contracting channels is significantly smaller than in the expansion cases. The largest ω intensity occurs at the exit of the contraction, and vorticies are significantly diffused downstream. Furthermore, there is not a coherent vorticity structure as seen in the expansion cases. The most structured vorticity occurs in **Set E**, which also has the most mixing. The results for **Set F** will be discussed in the following section.

Set F - Variable Expansion Rate with Constant Sill Velocity

The final set of simulations varies the rate of contraction, while maintaining a constant minimum channel width, corresponding to $m = -0.15$. The simulation set-up parameters are outlined in Table 2.6.

Set F - *Variable Contraction rate with constant sill velocity*								
m	q	U_0	U_{sill}	$xz3$	$xz5$	$xz7$	t_1	t_2
-0.15	6.25	0.1	1	0.35	0.5	0.65	$t = 20$	$t = 40$
-0.15	3.5156	0.1	0.65	0.35	0.5	0.65	$t = 20$	$t = 40$
-0.15	1.5625	0.1	0.48	0.35	0.5	0.65	$t = 20$	$t = 30$

The interface heights for simulation **Set E** show that the jump position is markedly further upstream than for the control case of a straight channel. Given the average velocity across the sill is constant between cases, the variation in interface position results from a combination of downstream position (i.e. where the jump is occurring in relation to the expanding portion of the channel) and velocity change due to the amount of downstream expansion through the jump.

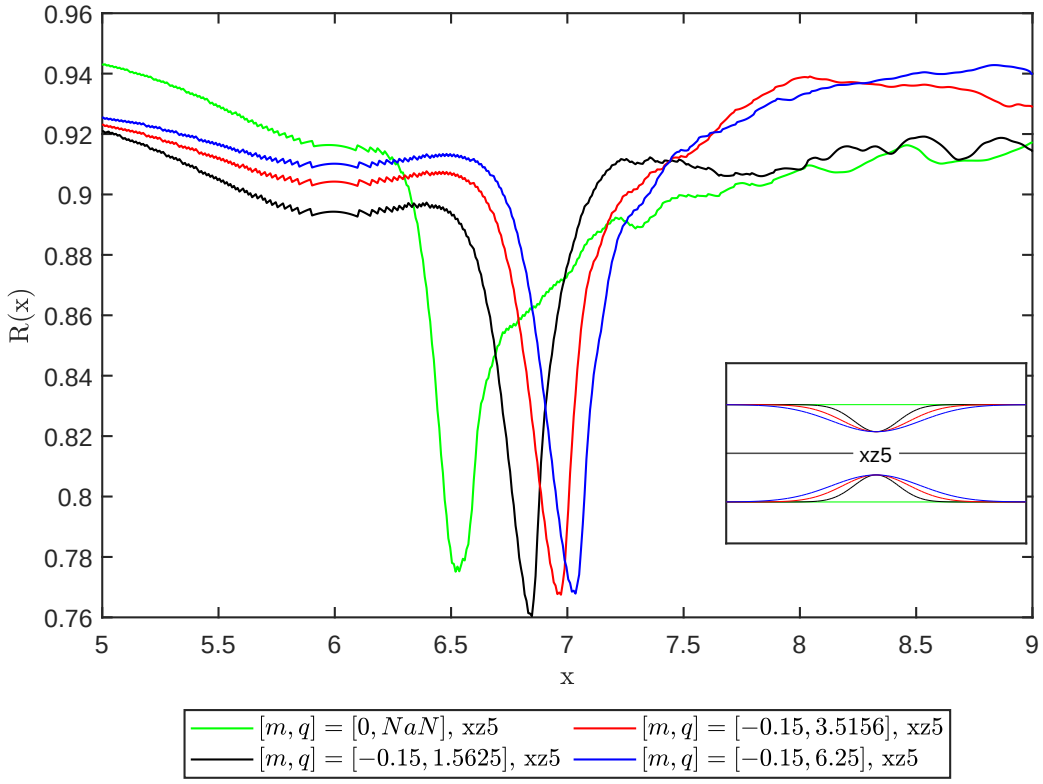

Figure 2.36: Set F interface heights, $R(x)$, for constant amounts of contractions, m, with variable rate, $q = [1.5625, 3.5156, 6.25]$. Corresponding topographies (bottom right) relate to coloured lines and are plotted for data along the channel center.

Furthermore, the position of the jump trends downstream with a smaller rate of contraction (larger q). For small q, the channel downstream cross-sectional area returns to the maximum extents much quicker than larger values of q, and thus the transition from supercritical to sub-critical flow occurs earlier. Furthermore, while the larger q occurs further downstream, the height of the jump is larger than for the smaller cases, or for the straight channel case ($m = 0$). This is a result of the momentum of the flow being larger as the transition is further downstream, and thus the size of the jump is bigger.

Finally, the mixing is quantified in Figure 2.37.

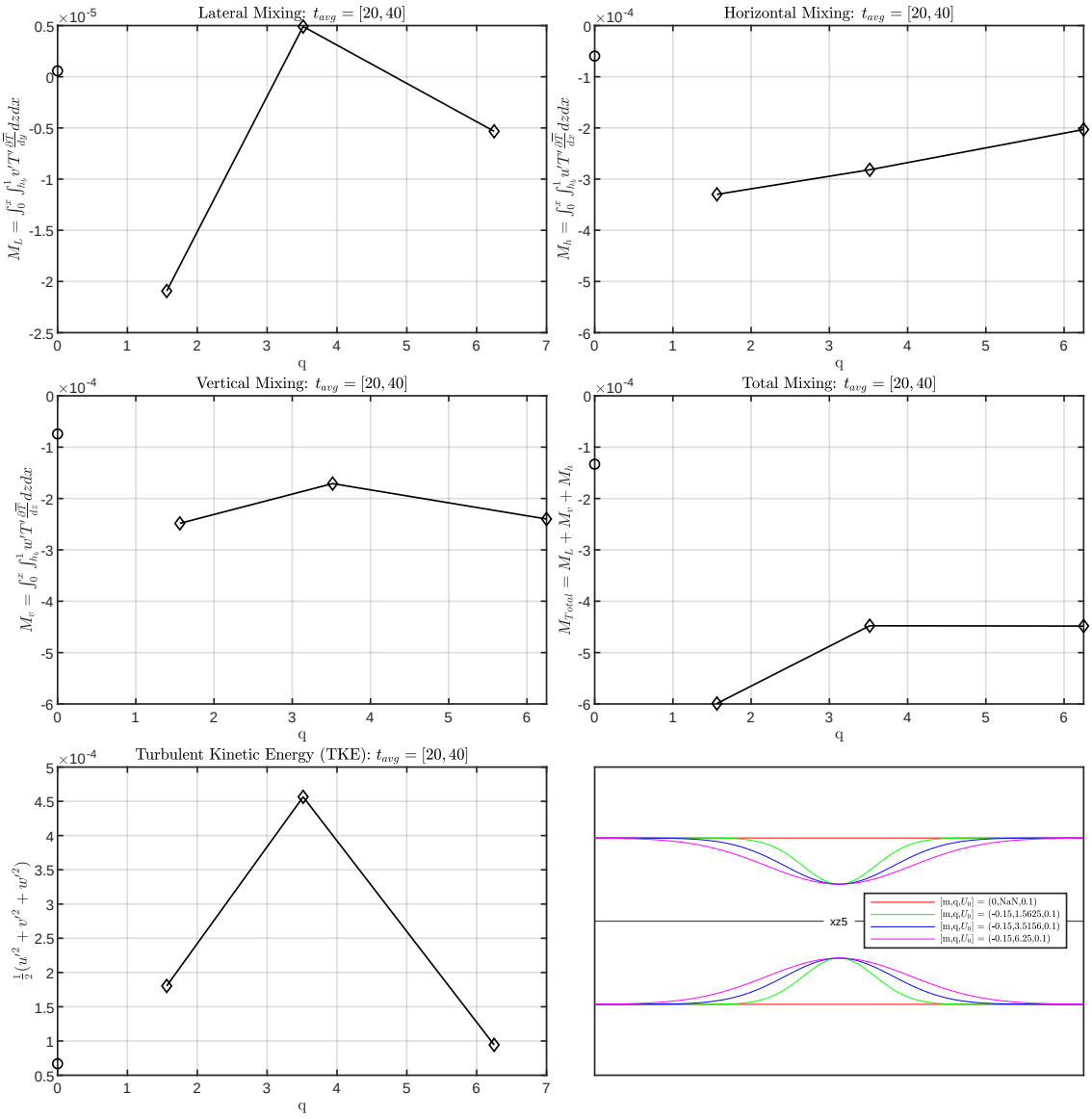

Figure 2.37: Set F - Constant contraction amount, m, with variable rate, q, mixing trend for all mixing components (Lateral, vertical and horizontal) as well as total mixing and TKE. Data plotted for channel center for increasing amounts of contraction.

The results do not show a significant trend towards more or less mixing for the vertical or total mixing, while horizontal mixing trends slightly toward decreasing with in increasing rate of expansion. Given that the position of the jump does not drastically change between cases, and the vorticity is localized toward the exit of the contraction rather than the channel center is likely the contribution to no trend seen. Additionally, the vorticity plots in Figure 2.35 showed

that the intensity was largest for $q = 1.5625$ and $q = 6.25$, which corresponds to the lateral and vertical mixing, as well as the turbulent kinetic energy. The variety in these results is likely due to the moving jump position and the downstream cross-sectional area for which the jump occurs. These results are consistent with those shown by Ganotaki [73] for which the total mixing is reduced as q increases. While there is scatter in the data due to the above factors, the mixing results for the straight channel case are plotted as a point and show that while there is not a significant trend in **Set F**, there is still significantly more mixing than case $m = 0$. This is further evidence that altering the geometry of the channel through either an expansion or contraction will increase mixing.

2.5 Conclusion

The goal of this chapter was to develop a better understanding of how channel width variation effects the mixing that occurs in a hydraulic jump. The results are summarized below:

Set A showed that mixing in the channel increased as the cross-sectional area at the sill increased. The dominant source of the mixing was the vertical component, which is expected given the mixing of layered densities is more likely to mix vertically, and is consistent with results seen in channels in the environment [3]. The average velocity at the sill remained constant, and thus the effect of the geometry on the mixing was isolated from a reduction in velocity. The factors that contributed to the mixing included the parabolic shape of the channel, which resulted in a maximum velocity in the lower layer in the lee of the sill, and a minimum velocity through the jump. This effect of the velocity difference caused a secondary increase in velocity in the leeward side of the sill along the thalweg, but significantly different in the off-center portion of the channel. This velocity difference due to the changing geometry resulted in the vorticity intensity in the center of the channel increasing as the cross-sectional area increased, and thus the amount of mixing increased markedly. Of note is the development of the vorticity in the off-center portion of the channel was less substantial than the thalweg, and

while the amount of mixing did increase in these regions, it was less significant.

Conversely, **Set B** simulated the same geometry, however the average velocity at the sill was reduced by the increasing cross-sectional area. This significantly reduced the velocity in the center of the channel, and contributed to an increase of more coherent, but less intense vorticies occurring in the off-center locations. As the flow diverged into the expanded region just downstream of the sill, the channel also begins to contract, increasing the velocity of the flow, but also increasing the amount of turbulence, and thus the flow in these regions is slower, or negative. This results in the velocity reduction counteracting the mixing caused by the channel geometry, and thus no trend in mixing is seen.

Set C maintained a constant expansion of $m = 0.15$ between cases, while the rate of expansion, q, was varied. Larger q corresponds to a decrease in the rate of expansion, and thus a more gradual slope, rather than a sharper slope for small q. Since the cross-sectional area the the sill was the same between cases, the average sill velocity was constant for each. The thalweg mixing had scatter in the results which was consistent with where the vorticity intensity was localized, and varied between cases due to the location of the jump. This had some variation as the cross-sectional area downstream was different, as well as some change in the position, so a coherent trend did not occur. Likewise in the off-center portion of the channel the vorticity intensity was dominant, and increasing due to increasing room for these to develop. Therefore, a more gradual expansion (larger q) results in more total mixing in the lateral regions of the channel as q increases.

While the focus of this work is on expanding channels due to the their similarities to Hood Canal, contracting channels were also investigated, however less results were available due to wave propagation at the boundaries. Additionally, only the thalweg data was available due to the topography cutting into the off-center data.

Set D also maintained a constant average sill velocity, but for contracting channels varying from $m = 0$ to $m = -0.15$. The results showed that there was no discernible trends in mixing, and this was likely due to a combination of the location the jump occurred, the parabolic

shape of the channel and the reduced downstream vorticity. For the cases of expansion in **Set A-C** the downstream contractions after the jump caused coherent vorticies to develop, while the contracting cases expand downstream, and thus Figure 2.35 shows non-coherent and non-intense vorticy structure. Specifically, most of the intensity occurs off-center at the exit of the contraction and is immediately diffused downstream due to the rapidly expanding cross-section and the jump. Generally, it is expected that altering the geometry of the channel will affect the mixing, however with less available data, it is challenging to make any definitive statements for these cases. Furthermore, depending on how the vorticity interacts with the layers of the stratified flow, the increase in mixing may not be captured. For example if the circulation is parallel to the layers, then mixing across densities would not be thoroughly captured. Turbulent Kinetic energy was increased as the channel contracted more, and thus given the previous results, this channel geometry is likely affecting the mixing.

Set E results showed a clear trend toward more mixing as the channel contraction increased. Given vertical mixing was dominant, the position of the jump moved downstream and the velocity drastically increased between cases, the increased mixing is attributed to the velocity increase. This is indirectly a consequence of the changing geometry. Therefore, given results for **Set A, Set B, and Set E** changing the geometry affects the mixing, but how the geometry affects the velocity is also an important consideration.

Set F results showed that mixing was increased compared to a channel with no change to the geometry extents, but the change between cases was not significantly affected. The amount of mixing is related to the intensity of the vortex formation, which was the least intense, nor localized to the thalweg for $q = 3.5156$, and the results reflected this. However with non-coherent vorticies forming due to the rapid downstream expansions, the trend is less explicit.

Finally, qualitative results of interface height, time averaged velocity and wave speeds in addition to quantitative results showing how the mixing varies across the channel suggest that simply calculating results along the thalweg [44] may not provide a complete picture of the flow characteristics [4].

In conclusion, a change to the channel geometry through either an expansion or contraction does impact the amount of mixing in and across the channel, due to the ability for vorticies to develop, the parabolic profile of the channel, the position of the jump, and how the velocity is affected by the changing geometry. All these factors also indicate that the entire flow field is important to consider, rather than only that along the thalweg.

The sill for these simulations was simple, and designed to force a hydraulic jump to occur, the next section will look at a more complex bottom topography in 2D and investigate how that complexity also affects the mixing.

Chapter 3

2D Internal Hydraulic Jump with Realistic Topography

3.1 Introduction

This chapter investigates the effect of topographic details on wave speeds, mixing and hydraulic jumps in Hood Canal. As discussed in §1.2.4 & §1.2.3 the complexities in the topography quickly complicate two-layer theory solutions, and thus, as the thalweg becomes more complicated, numerical simulations are more useful for understanding the details of the flow. While the previous chapter allowed lateral variation in the coastline, which hasn't previously been studied thoroughly (see §1.3.2), the domain is highly idealized. This chapter will investigate how along channel details in Hood Canal's specific topography impacts a stratified flow, in a 2D domain. Gregg & Pratt [7] provided data about the spatial and temporal structure of the flow in Hood Canal, but the complexity of the details of the density profile and bathymetry make comparison to two-layer theories difficult. They indicated the need for a geometrically complex, time dependent model that simulates some of the flow features at Hood Canal to further the understanding of the hydraulic control over the sill. Using existing data for the region obtained from Washington State, Department of Ecology, Environmental Information Manage-

ment System [1], shown in Fig. (1.1), this chapter focuses on simulating 2D flow forced over a similarly complex topography profile to that of Hood Canal, considering both flood and ebb tide.

The objectives to be studied are:

- Investigate how wave speeds vary over the sill in both ebb and flood tide.
- Compare mixing amounts downstream of the sill
- Compare mixing with idealized results from chapter §2

3.2 Numerical Modelling

3.2.1 Simulation Setup

Topography

The 2D topography profile in the region around the sill is based on the bathymetry data collected by Washington University Ecology Department [1]. A 12^{th} order polynomial fit along the deepest part of the channel is used to define the simulation domain. The topography data for the region of interest is shown in Fig (3.1); density profiles from points to the North and South of the simulated domain are used to simulate flood and ebb tide, respectively. Additionally, the location of the maximum channel width at the sill is shown, as well as the location of the sill, the channel thalweg and where the data values were collected.

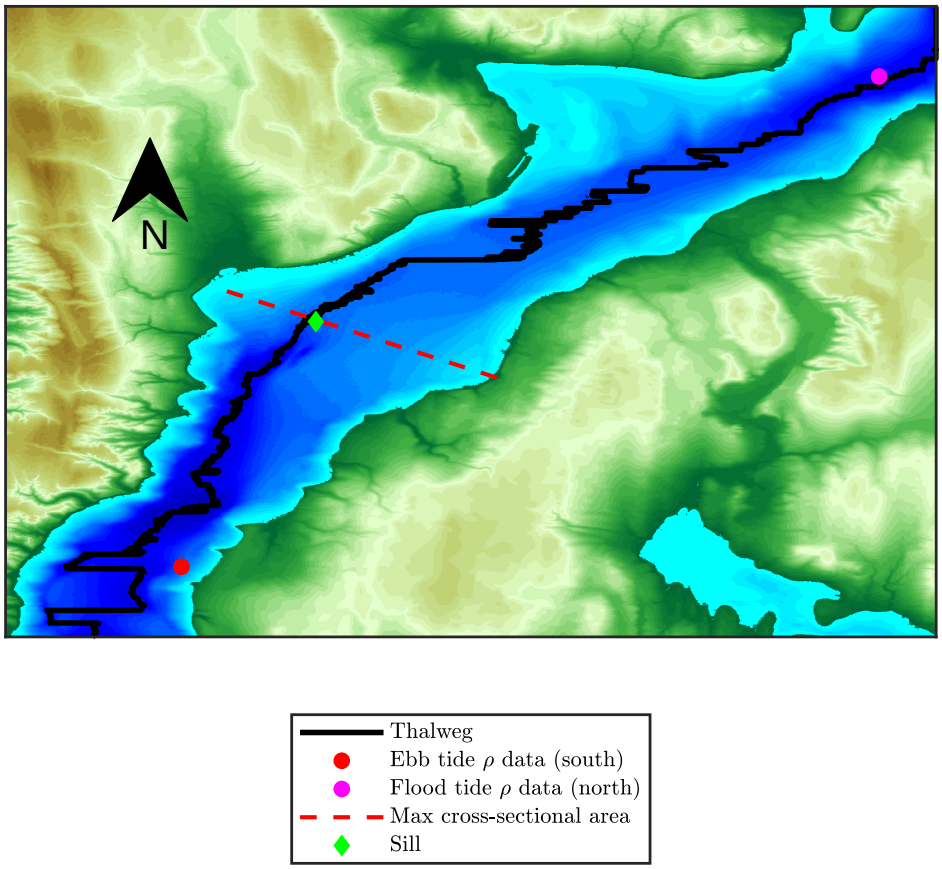

Figure 3.1: Hood Canal bathymetric data between Washington University [1] density data in the south (red) and north (magenta). Data for the thalweg is plotted and used for polynomial fit. The sill creates a hanging valley towards the relative west (⋄) and occurs in the middle of the maximum cross-sectional area (expansion). The channel has been rotated to run north-south for reference to density profiles.

For two dimensional flow, x is the along channel direction, while y is the channel depth. Additionally, flood tide occurs from the north, spilling over the sill, while ebb tide is driven from the south, experiencing blocking upstream of the sill. Ebb tide experiences a steep slope up to the sill and a gentle decline downstream of the sill, while flood tide has a much steeper drop-off after the sill. Figure 3.2 shows the thalweg profile for the topography with the 12^{th} order polynomial fitted function that is used in the simulation. This fit shows good agreement with the measured topography, as the depth and location of the sill are captured, as well as the

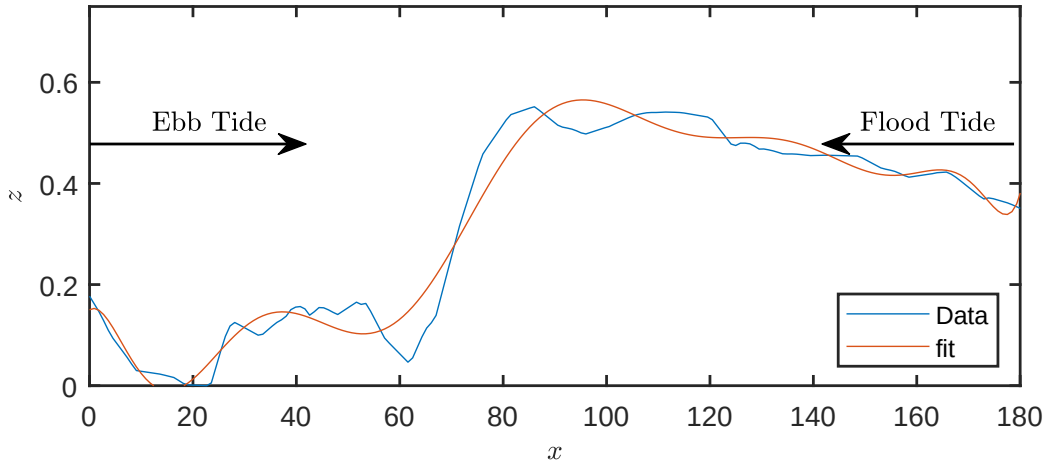

Figure 3.2: Polynomial fit to Hood Canal topographic data at deepest part of channel for 2D slice. Thalweg data represented by blue line, while curved fit used for simulation domain boundary represented in orange.

rate of change upstream and downstream with topography perturbations appropriately located.

Initialization

Density profiles were fit from data to the north and south of the simulation to a 15^{th} order polynomial. The data were selected in the month of September, when fresh water mountain runoff is considered to be high, resulting in more density variation through the depth of the fluid [7]. The Southern data was available for depths down to 98 m while the North only had data up to 25 m, however the greatest density variation occurs closer to the surface, therefore Northern data collected to 25-m was determined adequate as deeper variation is minimal. Density values at 25 m were repeated to a depth similar to that seen in the southern data. All parameters are non-dimensional in the simulations; density is scaled using $T = \frac{\rho - \rho_{min}}{\rho_{max} - \rho_{min}}$ as shown in Fig. (3.3).

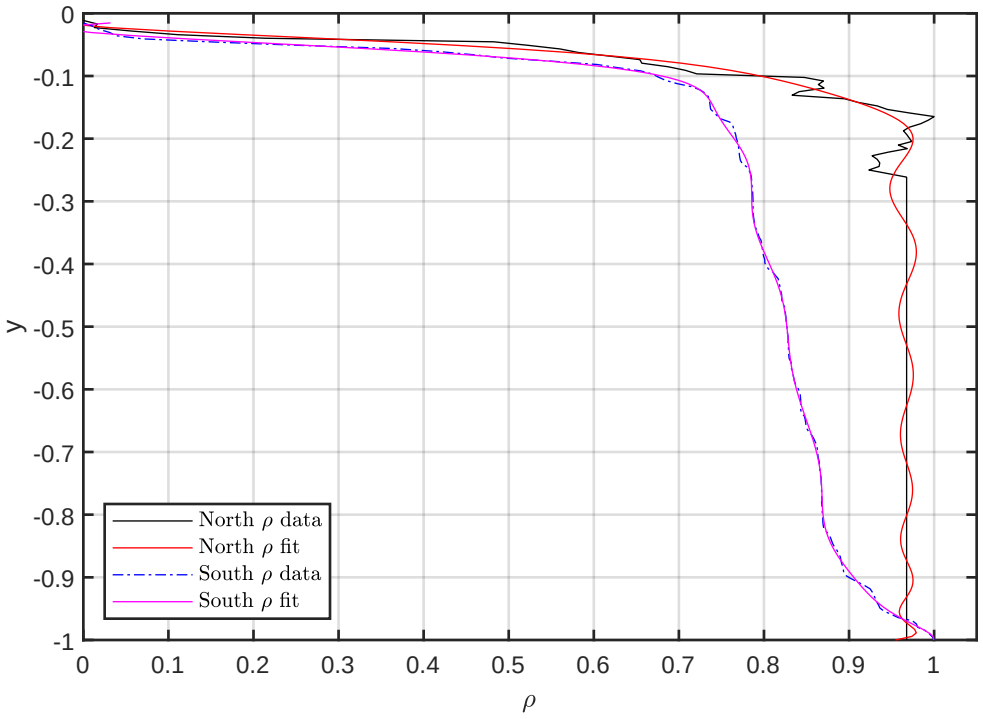

Figure 3.3: Density profile data for North (flood tide) and South (ebb tide) ends of Hood Canal collected from Washington University [1]. Density and depth is non-dimensional for simulations and fit to a smooth curve.

The simulations are forced with a velocity that is constant in depth and increases sinusoidally in time from zero until the maximum value is reached; the inlet velocity is then held at the maximum value so that statistical properties of a quasi-steady jump can be analyzed. The value of the maximum inlet velocity is taken from a low resolution 3D simulation of Hood Canal, described in chapter §4 where the vertically averaged velocity at the center of the north and south ends of the channel is used to force the 2D simulations described here. The 3D simulations of Hood Canal described in chapter 4 are the first step for future work related to this project. The velocity is non-dimensionalized as $U_0 = \frac{U_{avg}}{\sqrt{g'L}}$ where g' is the reduced gravity and L is the channel depth. This yields a flood tide velocity of $u_f = 0.1196$ and an ebb tide velocity of $u_e = 0.0929$ which gives the same volume flow rate in 2D at each inlet.

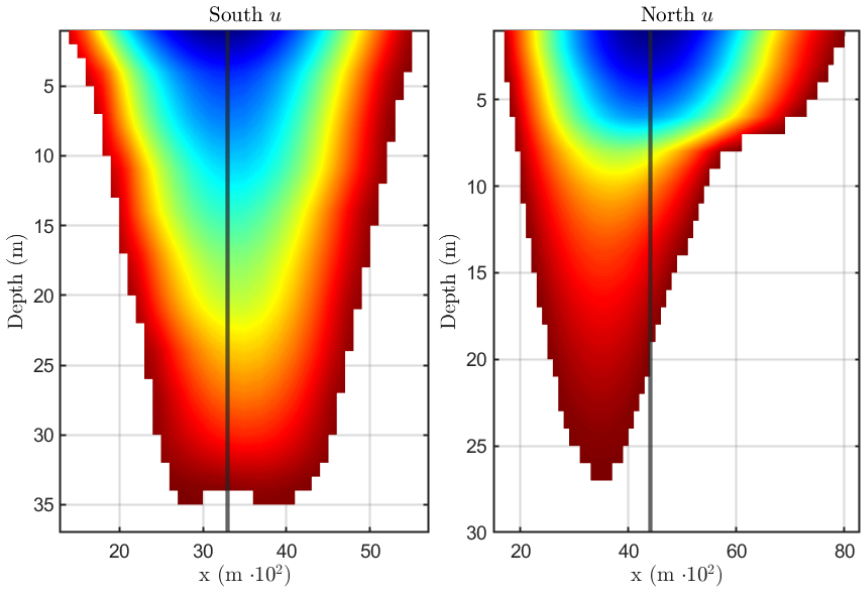

Figure 3.4: Velocity profile data for North and South ends of Hood Canal collected from Washington University [1] and obtained through forced simulation data. Average constant velocity used for simulations calculated along black line in center of channel for respective directions.

The solutions in this chapter also utilize Gerris flow solver described in §2. Furthermore, a grid size of 2^7 cells in the vertical is similarly used as results were previously shown to be grid independent [67][29] [73]. Thus, using a 2^7 grid resolution, and the above parameters, results are obtained for a 2D flow in both flood and ebb tide.

3.3 Results and Discussion

Mixing

The instantaneous velocity, time averaged density field, and cumulative integral of scalar variance are plotted in Figure 3.6 and Figure 3.5 for flood and ebb tide, respectively. The averaging period is chosen between $t = 150$ to $t = 250$ as the jump is quasi-steady through this time.

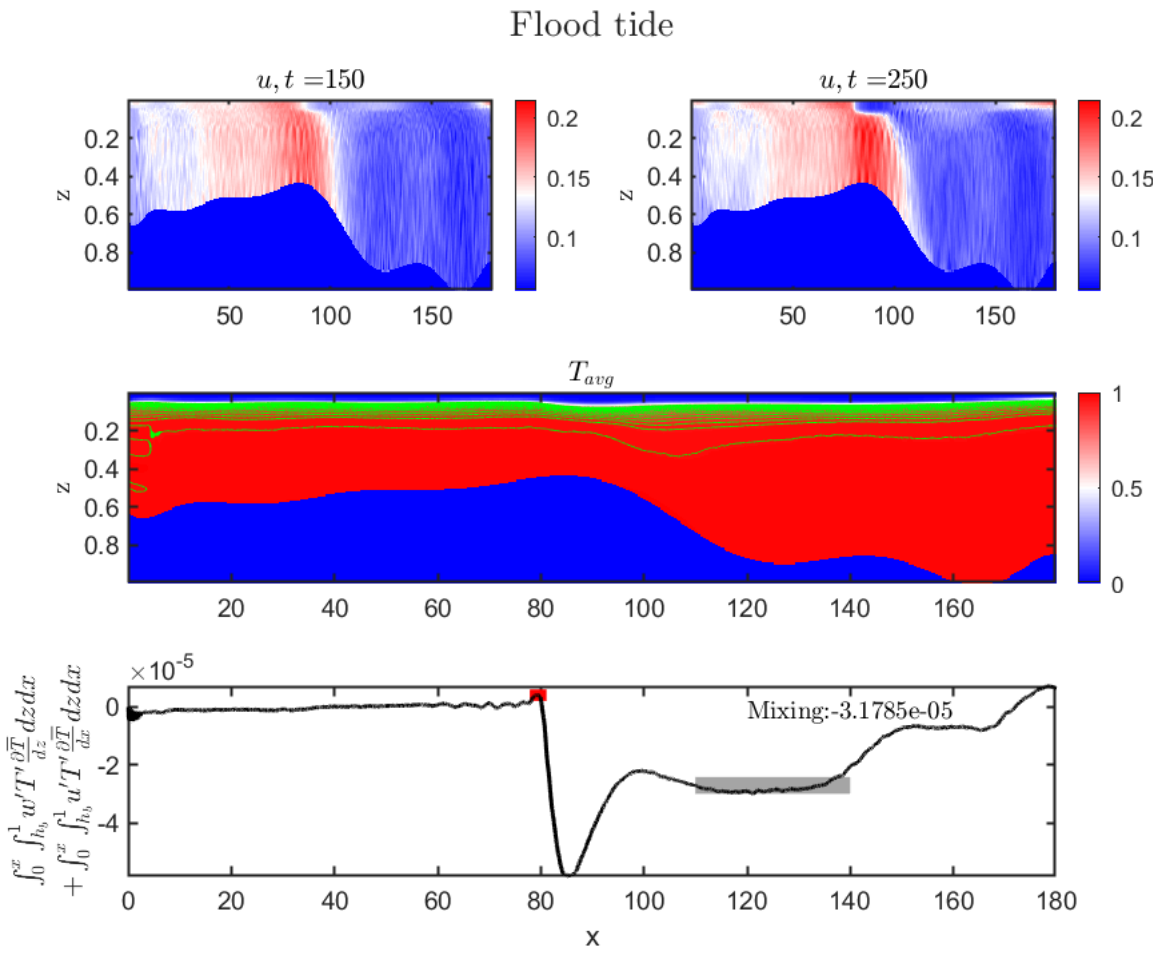

Figure 3.5: Flood tide instantaneous u-velocity at $t = 150$ to $t = 250$ (top), time averaged density with isopycnals (middle) and cumulative scalar mixing over the averaging period (bottom)

Velocity profile results for flood tide show that the velocity increases substantially over the sill. Similar to the lateral contraction cases in the previous section, as the channel cross-sectional area reduces due to the reduced depth, the velocity must increase to conserve mass, and thus a higher velocity is seen over the sill than the inlet. Downstream of the sill, the velocity is abruptly decreases as the vertical channel height sharply changes. This results in a small jump of the isopycnals, or lines of constant density, which are shown in green in the density plot; this fluctuation may be a hydraulic jump. Furthermore, the velocity snapshots show smaller internal waves within the domain, which appear as the alternating white and blue coloring downstream of the sill in the velocity plots. These structures are higher frequency

internal waves propagating with shorter wavelengths through the flow, caused by the smaller scale topographic variations and the continuous stratification. These waves would also occur in a 3D flow, and may increase the total mixing in the jump. Furthermore, a small jump is seen in the upper portion of the channel where stratification is the highest. Downstream of the sill, there is an expansion of the upper layer after the flow spills over the sill. Finally, the cumulative integral of the vertical scalar variance production is plotted and the total vertical mixing through the jump is calculated based on a point upstream and a region downstream of the jump. The mixing results are on a smaller order of magnitude compared to the §2. Given the abrupt change in downstream topography, more mixing is expected to occur in flood tide. While the mixing is smaller to the previous chapter, the jump is still coherent, and the formation of internal waves was not previously seen in the simpler topography. Therefore, the amount of mixing is non-negligible and therefore, the role of the bottom topography and lateral variations should be considered together.

Mixing, velocity and density results for ebb tide between $t = 150$ and $t = 250$ are plotted in Figure 3.6. Results show the instantaneous velocity for the channel, the flood tide density profile and the integral of cumulative scalar variance for the vertical mixing component. The total mixing through the jump for ebb tide is an order of magnitude less than for flood tide. This result is expected given the contrast in the downstream velocity. The topography profile for flood tide is not smooth upstream, but gradually contracts, and then abruptly changes causing a hydraulic jump to occur. Ebb tide, however, has a lower inlet velocity than flood, and must quickly adjust to the same sill velocity, but the downstream slope is much more gradual. Therefore the downstream velocity from the sill does not change as abruptly.

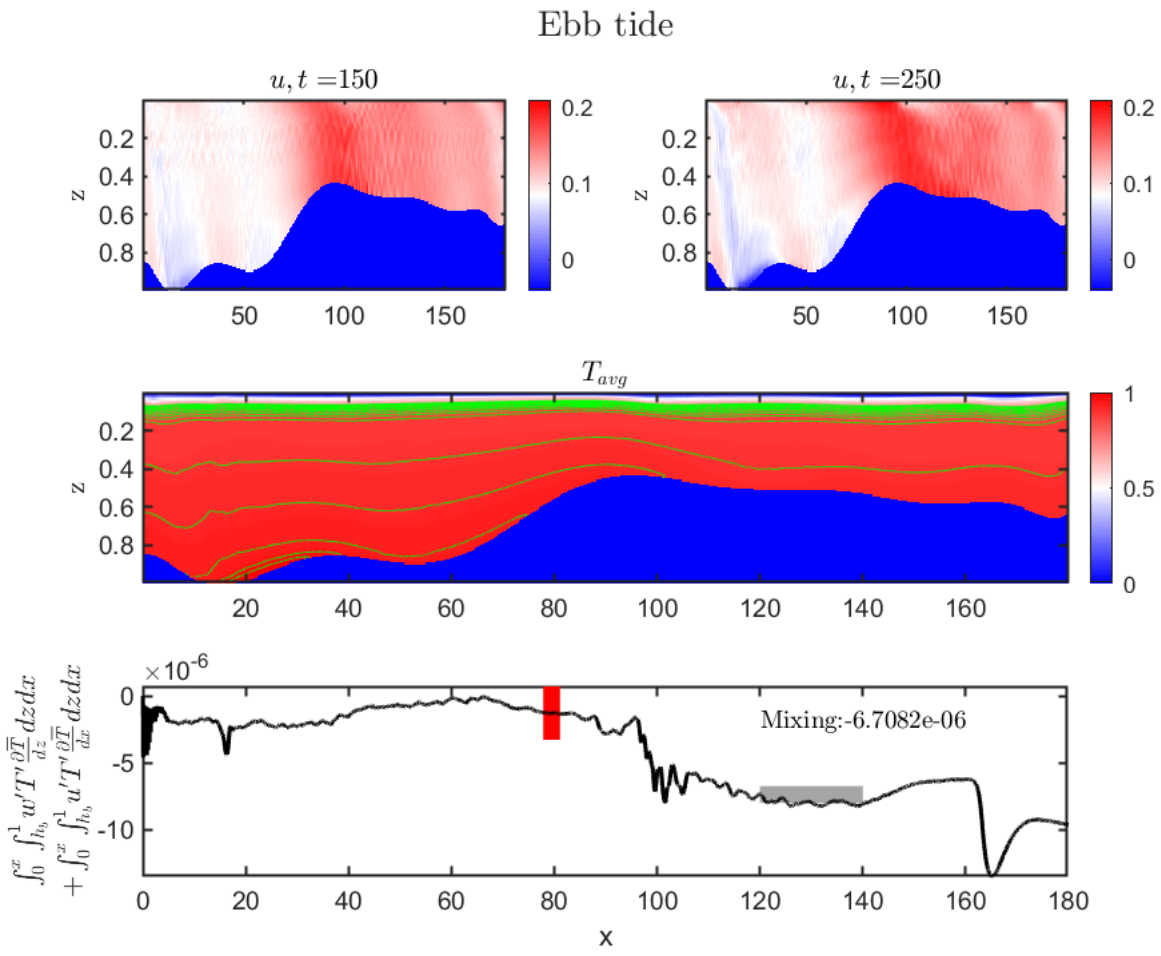

Figure 3.6: Ebb tide instantaneous u-velocity at $t = 150$ to $t = 250$ (top), time averaged density with green isopycnals (middle) and cumulative scalar mixing over the averaging period (bottom)

The substantial difference between amounts of mixing is likely a result the the variation in density profiles between the two flow directions. Additionally, the mixing is only accounted for in the scalar variance production equation if it occurs between fluids of different densities, which predominately occurs at the top of the channel. Lamb has shown that wave speeds with different stratification and the same velocity profile over similar topography have variation of 4% of the mean value of the solutions [77]. Figure 3.3, shows that the density profile for flood tide (forcing from the North) varies mostly in the upper layer, while ebb tide (forcing from the South) changes through most of the depth of the channel. The velocity profile shows shearing

between velocities in the upper portion of the channel where the stratification is the greatest. This contrast in the velocities through the apparent jump is likely where the turbulence is strongest, while also occurring at the interface, thus the mixing is higher. Likewise, the velocity profiles for ebb tide show vertical bands of similar velocities, which appears to be propagating waves downstream. This variation in velocity profiles is likely causing mixing across interfaces in flood tide, but not in ebb, thus resulting in more mixing for the former. Therefore, how the flow is stratified, how that corresponds to the direction of the flow over complex topography significantly impacts the amount of mixing in these simulations.

Wave Speeds

As stated in §2, the wavespeeds are calculated using the Taylor-Goldstein Equation (Eq. 2.13), but are estimations as the solution assumes vertical density and u velocity profiles in a straight channel, whereas these simulations involves complex topography with along channel variation and a vertical velocity component, resulting in a larger velocity magnitude.

The flood tide topography features create conditions for an overflow to occur as the sill plunges to large depths on the leeward side. Due to the periodic tidal forcing occurring at Hood Canal, time averaging for the simulation must be chosen relatively early, as analyzing later times may result in some features that would not actually occur in the channel due to the tide switching. The simulation reaches maximum velocity at $t = 50$ and therefore, averaging is done over a time period of $t = 150$ to $t = 250$ for which which the the results have sufficient time to develop, but waves that may begin to compound from continuous velocity over the sill do not.

The wave speeds for flood tide are plotted in Figure 3.7, and show that mode 1 remains largely sub-critical, while briefly almost reaching supercritical at the peak of the sill, and returning to sub-critical downstream. Due to the error associated with the wave speed calculation, wave speeds are likely underestimated, because the velocity magnitude is larger than just the horizontal component. Mode 2 wave speeds are largely supercritical through the apparent

jump, and become nearly sub-critical downstream.

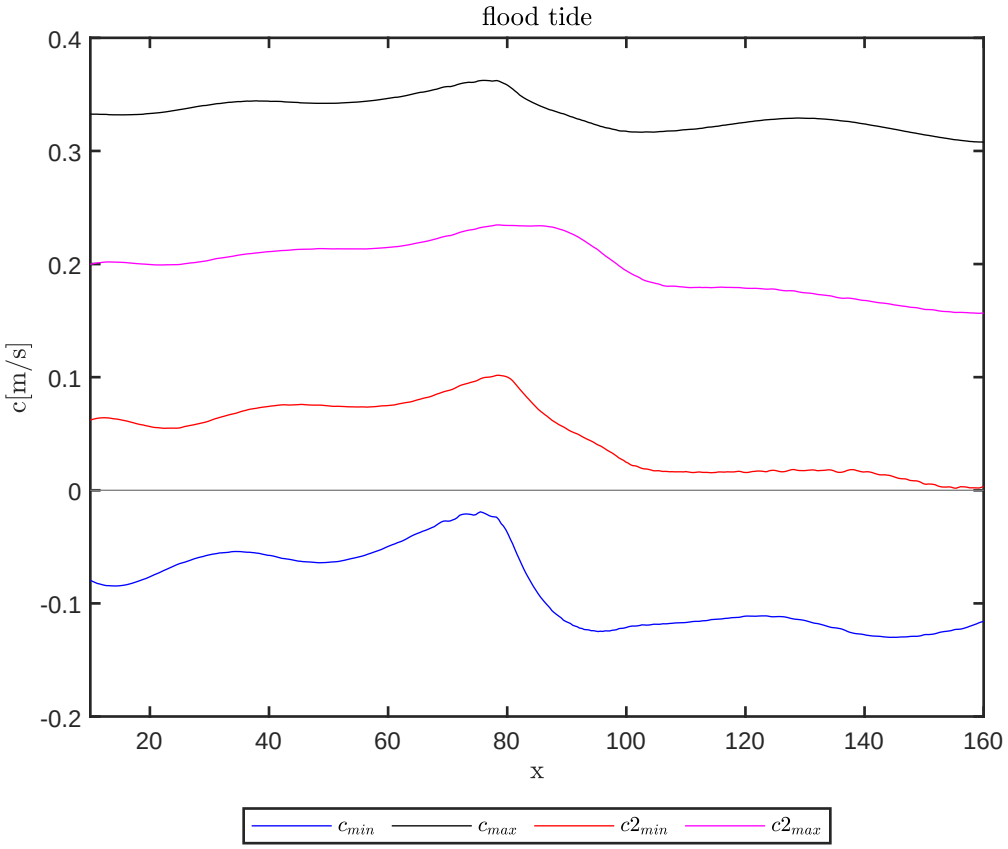

Figure 3.7: Mode 1 and 2 wave speeds during flood tide, averaged over $t = 150$ to $t = 250$. Plots show along channel min/max wave speeds corresponding to sub or supercritical flow.

Simulation results are compared to Gregg & Pratt's data from 2003 because they were collected during the same season as the density profiles used in the simulation. They found that during maximum flood, mode 1 was critical over the sill, while modes 2 and 3 remained largely supercritical during most of the tidal cycle. Furthermore, past the sill the flow remained strongly supercritical through the remainder of flood [7]. The wave speed results in Figure 3.7, deviate from the results, which largely depends on the forcing velocity, which has been approximated, while transverse velocities are excluded due to the 2D nature of the problem. Mode 1 does not quite reach supercritical (although it is likely underestimated) and mode 2 remains supercritical through the entirety of the flow. Given the approximations made, such as

the maximum at peak flood, the estimation of the thalweg, and the wave speed error, this quality of agreement is expected. Nonetheless, the impact of the Hood Canals 2D bathymetry on mixing is can still be estimated. The discrepency between the simulation and observations also suggest that channel width variations, which are significant in Hood Canal, may be important to include in more realistic simulations.

Ebb tide wave speeds (fig. 3.8) were strongly sub-critical for mode 1 until just ahead of the sill where they were briefly supercritical, before returning to slightly sub-critical, and alternating due to the downstream changes in the topography. Mode 2 was mostly supercritical through the entire apparent jump. Considering the abrupt topography change, the stratification and the velocity at the sill, this result for the wave speeds is expected. Additionally, the downstream grade of the channel is much shallower, and thus the u component becomes much more of a maximum compared to the estimation for flood tide.

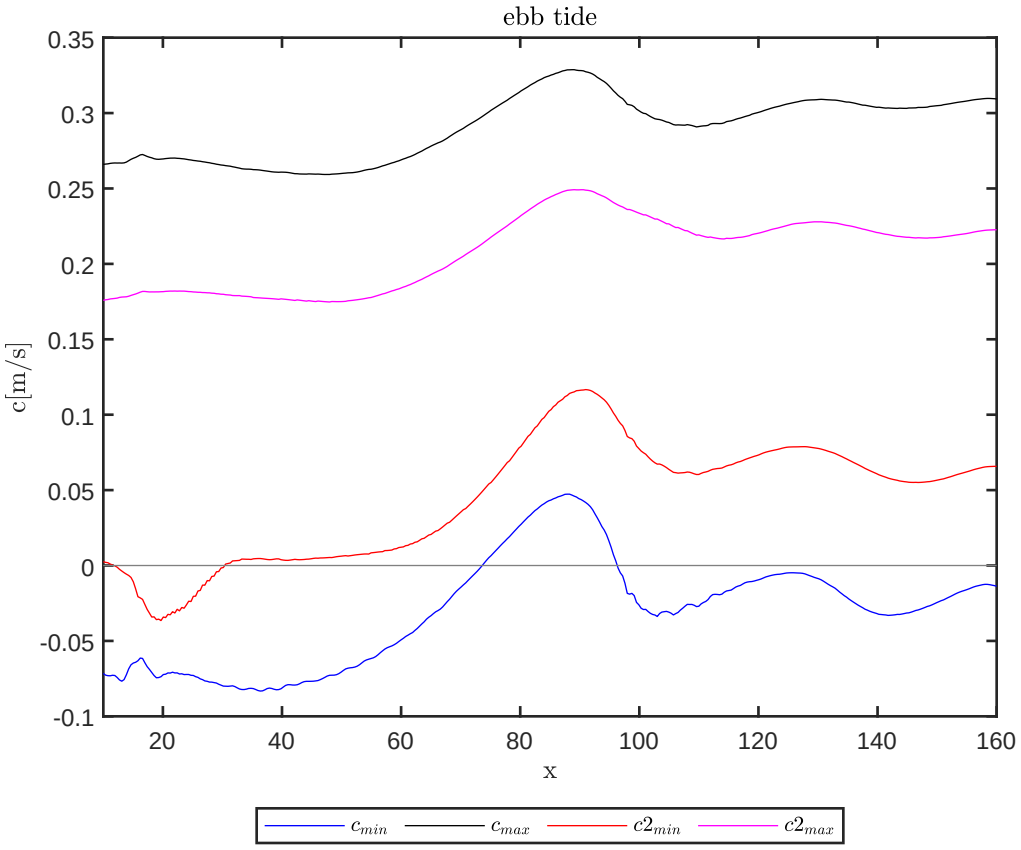

Figure 3.8: Mode 1 and 2 wave speeds during ebb tide, averaged over $t = 150$ to $t = 250$. Plots show along channel min/max wave speeds corresponding to sub or supercritical flow.

These results are somewhat consistent with observations seen in Hood Canal, for which ebb tide was mostly sub-critical where the depth of the channel was large, and became briefly supercritical through the crest of the sill [7]. The jump in these simulations is not clearly apparent in the velocity profiles or isopycnals; however the wave speeds do suggest a jump is forming over the sill. This is, however, not unexpected given the drastic changes in velocity at the sill crest. Furthermore, Gregg & Pratt [7] also found that for ebb and flood, mode 2 wave speeds were mostly supercritical for all of their observations for most of these tidal cycles.

Gregg & Pratts [7] observations also showed that the density field for flood tide resembled an overflow with internal hydraulic control at the sill. A similar result is seen here via the isopycnals plotted in Figure 3.6; however, the wave speeds they saw were largely super crit-

ical, while the wave speeds depicted here are not. Likewise, the ebb tide flow they observed produced many examples of super-critical flows at the choke point (the shallowest portion of the channel topography, the sill) of the channel, which is also observed here, while the density field did not clearly show a hydraulic jump. The isopyncals shown for ebb tide in this work indicate somewhat similar results, however there was much more upstream variation in observations. These partial indications of a hydraulic jump are the motivation to study the flows with this complex topography.

3.3.1 Comparisons with 3D simulations

Finally, one of the main motivators for studying hydraulic jumps in Hood Canal is to investigate the amount of mixing that occurs, as this may contribute to the hypoxic conditions, as reduced mixing results in a reduction of oxygen ventilation and nutrient supply, and can specifically be affected by a decrease in deep water renewals due to the complexity of the topography, affecting the aquaculture [9].

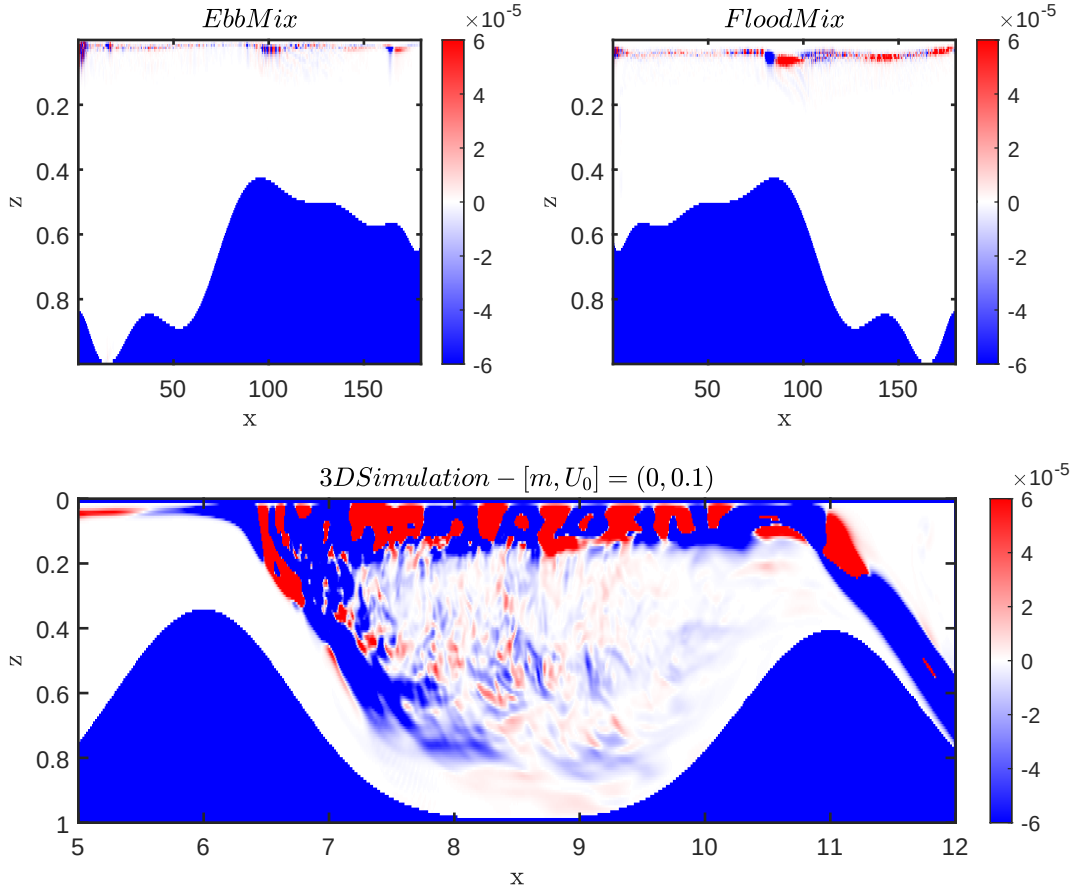

Figure 3.9: Mixing comparisons for §2 and §3 data. 2D mixing intensity for ebb (top left) and flood tide (top right) shown compared to mixing intensity for straight channel case, $m = 0$, in the channel center from chapter 2

Figure 3.9 shows a comparison of the straight channel ($m = 0$) thalweg mixing, and ebb and flood tide plotted as colors of intensity through the channel. Case $m = 0$ was selected as the inlet velocities are comparable, as well as the sill height. There is a substantial difference between the realistic simulation, and the idealized. While mixing for both ebb and flood tide were considerably lower than the results for the idealized 3D simulations, the mixing was also largely localized far from the channel depths. Given the realistic density profiles used for ebb and flood tide, and the reduced mixing, this may result in a reduction in the displacement of the bottom water and nutrients. Given the differences between these results, the stratification and topography clearly are important considerations.

3.4 Conclusions

The objective of this chapter is to investigate the effect of details such as small scale topographic variation and realistic density profiles on the jump that occurs in Hood Canal. Most important is to understand what type of realistic considerations need to be made when studying hydraulic jumps in channels and straits in nature. The wave speed results obtained were similar to those seen in Hood Canal, however there were some differences, which can likely be explained by the method used to calculate the wave speeds, the approximate velocity forcing, and the simplified 2D simulations. The changing topography between flood and ebb clearly had an effect on how much mixing occurs in this simulation, but the variations in wave speed results compared to Hood Canal demonstrate that a more realistic domain is important in order to accurately compare results to Gregg & Pratts [7] observations at Hood Canal and to fully characterize the hydraulic jumps occurring in these complex channels. Gregg & Pratt [7] obtained different results as they obtained data at different points along the channel, for example they did not necessarily see a jump occurring along the thalweg, and the flow was not at peak tide as they expected. Results for this work show that the direction of the flow does impact the amount of mixing because of the stratification and the topographic slope downstream of the sill, and that wave speeds down the thalweg vary. Furthermore, some higher frequency waves occurred in this set of simulations because of small scale along channel topography variations, shown in Figures 3.5 & 3.6, which were not present in §2. Flood tide also showed much more mixing than ebb tide, although both were much less intense, and localized toward the surface compared to the previous chapters highly mixed simulations, and thus the combination of density profiles and tide-topography interaction surely has an effect on the amount of mixing, and potentially the hypoxia in Hood Canal, although the 2D simulations are not specific enough to verify the latter. In summary, the results obtained in this chapter provide a few conclusions on the factors affecting mixing:

- Small along channel variations in the topography generated higher frequency internal

waves which may contribute to the mixing in the jump.

- The stratification has an important effect on the amount of mixing that occurs. Depending on where in the depth the most turbulence occurs, how the flow is stratified and the topographic profile, the mixing may increase. Flood tide had the more mixing than ebb, which was expected given the direction of the flow over the topography, however, this was still localized to the top of the channel.

Thus given these results, and the comparisons made with Hood Canal, it is important and necessary to realistically describe the flow domain in order to obtain a better characterization of the flow field.

Chapter 4

Conclusion

4.1 Mixing in Complex Domains

The objective of this work is to determine how topographic channel variations around a hydraulic jump affects the mixing within the channel, a topic that has not been thoroughly investigated, with motivation stemming from the geometry and impact of mixing at Hood Canal. The results show that topographic changes to the channel have an effect on the mixing both in the center of the channel (away from the geometry changes), as well as towards the transverse bounds. Furthermore, 2D simulations show that smaller scale details in the bottom topography affect the mixing, and that the entire flow field is relevant for these hydraulic jumps

Chapter §2.4.1 specifically investigated how expansions around a hydraulic jump forced by a sill affect the mixing. Results isolating the geometry effect (**Set A**) showed that increasing the size of the expansion increases the amount of mixing and the vorticity in the channel. Along channel velocity through the center of the channel was the highest, as it has the most direct along channel path and thus vertical mixing in the center of the channel was dominant. Conversely, when the geometry effects were not isolated from the effect of velocity (**Set B**), the along channel velocity decreases with the expansion, resulting in a weaker jump and weaker vortices after the jump, which reduces mixing. This reduction in mixing is balanced by the

increased mixing that occurs due to the channel width variation; these counteracting factors result in no trend in mixing as the channel width varies. Furthermore, for simulation set **Set C**, when the channel width remained constant, but the rate of expansion was varied, as the slope of the expansion became more gradual there was more room for vorticies to develop. Therefore, the vortex intensity increased as the rate of expansion decreased, and the mixing in the off-center portion of the channel increased. Likewise, chapter §2.4.2 conducted similar investigations, but with a contraction with the sill. In these cases, results showed that when the effect of the geometry was isolated, no trend in mixing occurred, while the coupled results led to a substantial increase in mixing. For the combination of the contraction and increasing velocity, the vertical mixing increased substantially as the velocity was significantly increased through the sill as channel became more narrow. Given these results, it is clear that multiple factors effect the mixing, which are challenging to isolate.

- For a given flow rate expansions increase mixing, but decrease velocity, thus having a net insignificant effect on the mixing

- Increasing the amount of expansion results in coherent and structured vorticities which are either increased or decreased in intensity depending on the velocity over the sill. If the average velocity is constant, the increasing expansion and parabolic topography profile results in more intense vorticies, and more intense mixing.

- Decreasing the rate of expansion provides more room for vorticies to develop downstream of the jump, which become more coherent and intense and result in dominant mixing in the off-center portion of the channel.

- In simulations where the velocity was increased due to the contracting channels, the vertical mixing was dominated by the increase in velocity. Ganotaki and Ogden [73] obtained similar results, including unstructured vorticies in the lee of the jump. They also concluded that mixing was dominated by the increasing intensity of the jump due to the velocity increase.

- Wavespeeds, vortictiy and mixing trends for expansions show that consideration of the full flow field is important for locations like Hood Canal, which has complicated topography and an expansion coincident with a sill.

While results for chapter §2 investigated the effects of idealized geometry, the thalweg remained smooth and constant. Therefore, chapter §3 simulations looked at how the complexity of the thalweg and flow details at Hood Canal affected the channel mixing. The results were compared to some observations by Gregg & Pratt [7] and showed that topographic as well as stratification details have important effects on hydraulic jumps in channels in the environment. The small changes in topography generate higher frequency internal waves, which have been shown to contribute to mixing [77], and thus indicate cross-waves could form in more complex 3D domains. Jump intensity also varied between flood and ebb tide due to the stratification, for which a localized change at the top in flood tide resulted in more mixing where the velocity change was the most dramatic, while ebb tide was stratification deeper in the flow and had less mixing across a the density interface. Furthermore, due to the turbulence and mixing localized to the top portion of the channel compared to the 3D simulations for which mixing occurred much deeper, there is indication that oxygen content in the bottom of the channel could be affected by the reduced mixing. However, more realistic 3D simulations are necessary to further investigate this.

Therefore, lateral variations and complex bottom boundaries in topography, specific stratification and velocity forcing are all factors that can increase mixing in environmental flows in complex channels.

4.2 Future Work

The results obtained in this work show that hydraulic jumps occurring in complex topography requires consideration of the entire flow field, and as such studying the full 3D flow of Hood Canal should be a topic of future work.

In an effort to stimulate that work, the setup of a 3D simulation using Hood Canals bathymetry, velocity, and stratification data is outlined here in order to alleviate some of the potential challenges that could be faced when setting up a realistic simulation. Furthermore, since flows occurring in nature are complex to accurately model, the simulation tool MITgcm is recommended as it includes models for a number of environmental factors that cannot as easily be simulated in Gerris. This includes simulating factors that can affect flow features, including density stratification, surface meteorological forcing, complex topography, [31] and rotation. Due to the difficulty with obtaining observational data, and the variation that can occur between regions given different temperature profiles, densities and topographical features, developing these robust simulations and obtaining accurate results becomes more important, but also more difficult. The following will outline some of the initial steps taken, and some of the lessons learned for modelling a 3D realistic flow in Hood Canal.

4.2.1 MIT General Circulation Model

While Gerris is a useful tool for ideal simulations with complex boundary features, some components are not able to be simulated, including surface winds and more complex stratification profiles. Therefore, the MIT General Circulation Model [21], which is commonly used for simulating environmental flows, is recommended for this work, and initial steps to set up this simulation are described here. Some of the flow features that were previously modelled relied on ideal estimates of velocity profiles and density stratification, while MITgcm is able to read in more realistic matrix data. Specifically, using exact data for the Temperature and Salinity, as well as topographic data rather than fitting the data to a function will provide more realistic simulation results.

MITgcm uses one hydrodynamic kernel to study both atmospheric and oceanic phenomena. The flow is governed by the Boussinesq, Navier-Stokes equations (Eq. 2.8). MITgcm supports use of the non-hydrostatic model, is important to accurately capture the dynamics with an internal hydraulic jump. The non-hydrostatic capability makes it particularly useful on smaller

scale simulations ($100m$) in which vertical fluctuations and sub-grid turbulence are important.

Furthermore, the state of the fluid at any time is characterized by the distribution of velocity $\mathbf{v}$, active tracers θ (temperature) and S and a density $\rho = \rho(\theta, S, p)$. The ability of MITgcm to treat nonhydrostatic dynamics in complex geometry makes it an ideal tool for studying internal wave dynamics and mixing in ocean canyons that is driven by large amplitude barotropic tidal currents imposed through open boundaries.

Finally using the topographic data available from Washington University, Department of Ecology, allows a realistic three dimensional description of the bathymetry. Initial simulation results shown below are not well resolved enough to make any conclusions about the existence of a jump, but outline and approach as a starting point for future, more complex, studies of Hood Canal.

4.2.2 Simulation Setup

MITgcm uses a combination of Temperature and Salinty profiles to specify the density field, in contrast to Gerris, which calculates density as a single variable. Observational density profiles for Hood Canal were available at either end of the channel, and the density profiles were interpolated between the two ends. For the this initial setup, only two profiles were used, and interpolated across the entire channel, however, future work should consider using additional available data at an intermediate point in the channel, as the interpolation occurs over a great distance, and may not be as accurate near the sill. Adding a third data profile will allow more accurate development of the stratification field.

Additionally, the data provided for the North and South regions of the channel had different depths which did not reach the channel bottom. Since the largest stratification occurs near the top, repeating the final Temperature and Salinity data points until equal depths was sufficient. For example, if the North density has 25 m of data points, and the South has 96 m, copying the last data point in the North set from 25 m to 96 m is sufficient given the density variation at these depths does not drastically vary.

For this simulation the temperature and salinity profiles were obtained from the Environmental Information System collected by the Department of Ecology in the state of Washington. Northern profiles were collected on September 29th, 2016 at a latitude of 47.837 and longitude of -122.628, while southern profiles were collected on September 26, 2016 at a latitude of 47.667 and longitude of -122.82, just passed the sill. Due to the up-welling caused by runoff from the Olympic mountains occurring in the spring and fall, and the availability of data in September, this was the optimal time of year for the simulation data to give an accurate representation of the conditions present when a hydraulic jump is postulated to exist [7].

Using a nesting approach, a course initital simulation is recommende to calculate the realistic distribution of velocities and scalars that can be used to initialize and force subsequent finer simulations. The initial grid size was chosen as 80 cells in x (transverse direction), 60 in y (along channel direction) and 16 in z (depth). The simulation is nested meaning results from the previous simulation are used to force the next finer simulation, in order to refine the domain. Additionally, due to the meandering channel, which can cause numerical difficulties when the inlet velocity must turn abruptly, a useful solution was to extrude the inlet and outlet of the topography shown in Figure 4.1 .

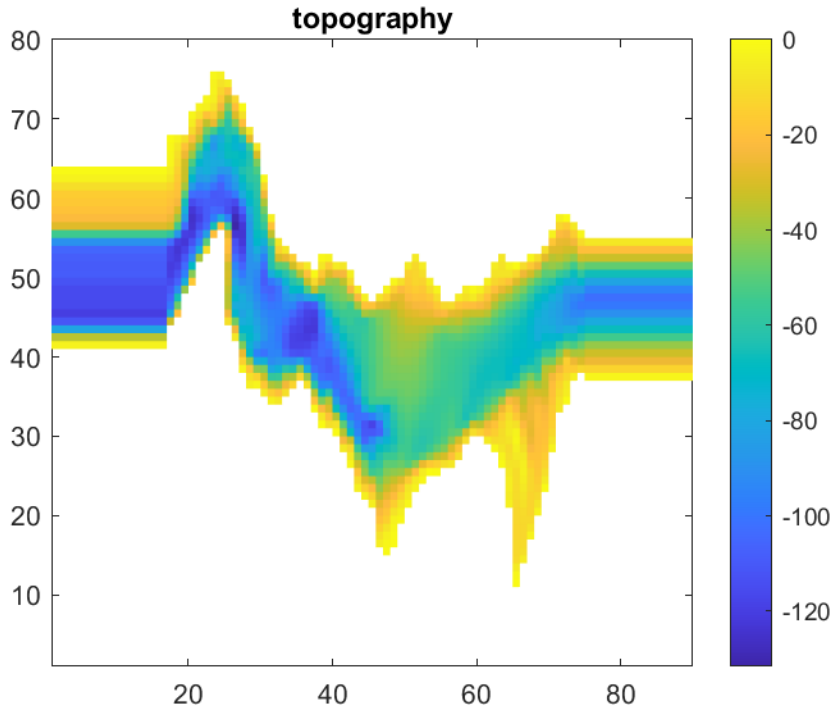

Figure 4.1: Top view of extruded topography profile for Hood Canal MITgcm simulation initial setup.

By extending the topography, and forcing a flow rate from the left (of the figure), a velocity profile is develops for the flow based on the topography at the inlet. Allowing more room for this profile to develop reduces numerical errors due to the abrupt change in topography right at the initial inlet. Results for this unrefined simulation were used to force the next simulation, for which the channel was cut to a smaller portion around the sill, shown in Figure 4.2

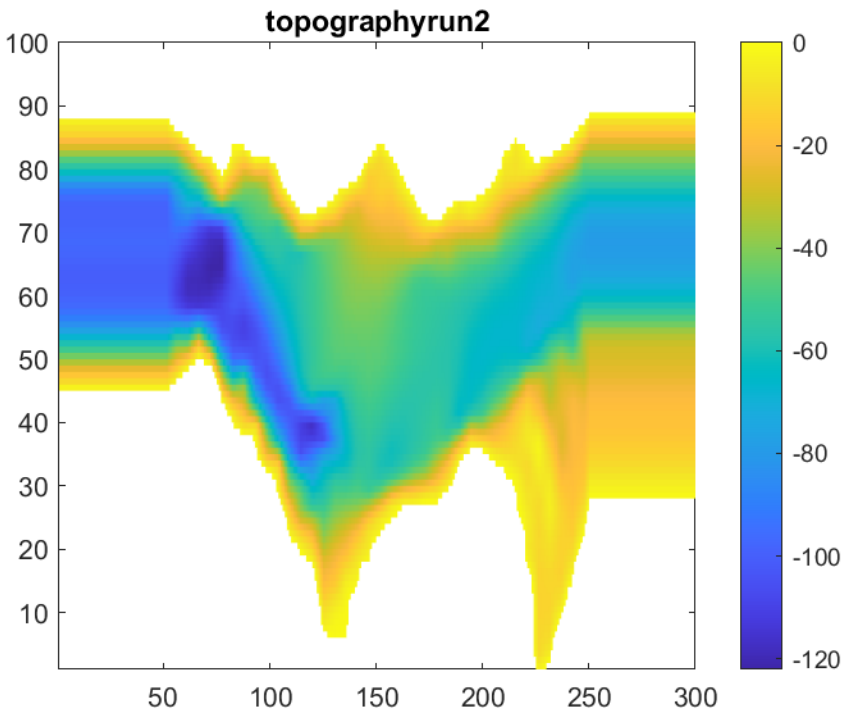

Figure 4.2: Top view of extruded topography cut to region around sill with increased grid refinement

Cutting the topography to the region around the sill removes the complex parts of the channel that cause instabilities in the flow, and impact the solution before the flow is able to develop over the sill. Furthermore, since MITgcm allows the flow to be tidally driven, running for two full tidal cycles allows all the flow features to fully develop more fully, which is more consistent with a flow field in nature. This is more realistic than §3 results as only maximum tidal forcing in either direction could be simulated. The resolution is further refined by using the velocity, temperature and salinity results from the previous simulation to force the subsequent simulations, while decreasing grid size with each nested simulation. Resolving the velocity profile in this manner also proved specifically useful for the 2D simulations as shown in §3 (Fig. 3.4).

This process is presented to guide a more detailed study of the flow in Hood Canal, which could include rotational effects [67], surfaces winds, etc.

4.2.3 Recommendations

The following points are outlined to assist future researchers in expediting the set-up process for Hood Canal:

- For initialization of temperature and salinity profiles, if available choose multiple locations along the region of interest in Hood Canal. This will reduce the amount of error which can arise from interpolating profiles across long distances.

- Choose a boundary location in the channel which is sufficiently straight for at least 5 grid cells. This will minimize the numerical instabilities that form when forcing the flow immediately into a complex area with a low grid resolution

- Increase the number of intermediate nested simulations. The above results used 3 simulations and doubled the resolution in each set. The optimal depth (z) cell size is about $1m$, but decreasing cell size too abruptly may introduce error.

- Extruding the inlet and outlet 50 cells in each was extremely useful for developing the velocity profile and removing the instabilities.

These recommendations may assist researchers in improving simulation results and obtaining meaningful information for flow in Hood Canal.

Bibliography

[1] Washington Department of Ecology, "Environmental information management system." http://www.ecology.wa.gov/eim/, 2020. Accessed: 2020-2022.

[2] Y. Yasuda and W. H. Hager, "Hydraulic jump in channel contraction," *Canadian Journal of Civil Engineering*, vol. 22, no. 5, pp. 925–933, 1995.

[3] G. Egbert and R. Ray, "Significant dissipation of tidal energy in the deep ocean inferred from satellite altimeter data," *Nature*, vol. 405, pp. 775–778, 2000.

[4] J. M. Klymak and M. C. Gregg, "Three-dimensional nature of flow near a sill," *Journal of Geophysical Research: Oceans*, vol. 106, no. C10, pp. 22295–22311, 2001.

[5] J. Sánchez-Garrido, G. Sannino, L. Liberti, J. G. Lafuente, and L. Pratt, "Numerical modeling three-dimensional stratified tidal flow over Camarinal sill, Strait of Gibraltar," *Journal of Geophysical Research*, vol. 116, 2011.

[6] K.Ogden and K. Helfrich, "Internal hydraulic jumps in two-layer flows with upstream shear," *Journal of Fluid Mechanics*, vol. 789, no. 64-92, 2016.

[7] M. Gregg and L. Pratt, "Flow and hydraulics near the sill of Hood Canal, a strongly sheared, continuously stratified fjord," *American Meteorological Society*, vol. 40, pp. 1087–1105, 2010.

[8] M. Gregg and E. Özsoy, "Flow, water mass changes, and hydraulics in the bosphorus," *Journal of Geophysical Research*, vol. 107, 2002.

[9] J. Newton, C. Bassin, M.Kawase, W. Ruef, M. Warner, and A. Devol, "Hypoxia in Hood Canal: An overview of status and contributing factors," *Proc. Georgia Basin Puget Sound Research Conf.*, 2007.

[10] M. J. Warner, M. Kawase, and J. A. Newton, "Recent studies of the overturning circulation in hood canal," in *Proceedings of the 2001 Puget Sound Research Conference*, p. 9, Puget Sound Water Quality Action Team Olympia, Washington, 2001.

[11] M. A. Noble, A. L. Gartner, A. J. Paulson, J. Xu, E. G. Josberger, and C. Curran, "Transport pathways in the lower reaches of hood canal," *US Geological Survey Open-File Report*, vol. 1001, p. 35, 2006.

[12] D. Fagergren, A. Criss, and D. Christensen, "Hood Canal low dissolved oxygen: Preliminary assessment and corrective action plan," *Puget Sound Action Team*, 2004.

[13] H. Chanson, "Current knowledge in hydraulic jumps and related phenomena. a survey of experimental results," *European Journal of Mechanics-B/Fluids*, vol. 28, no. 2, pp. 191–210, 2009.

[14] F. M. White, "Fluid mechanics," 2013.

[15] W. H. Hager, *Energy dissipators and hydraulic jump*, vol. 8. Springer Science & Business Media, 2013.

[16] L. Arneborg and B. Liljebladh, "Overturning and dissipation caused by baroclinic tidal flow near the sill of a fjord basin," *Journal of physical oceanography*, vol. 39, no. 9, pp. 2156–2174, 2009.

[17] J. M. Klymak and M. C. Gregg, "Tidally generated turbulence over the knight inlet sill," *Journal of physical oceanography*, vol. 34, no. 5, pp. 1135–1151, 2004.

[18] A. Staalstrøm, L. Arneborg, B. Liljebladh, and G. Broström, "Observations of turbulence caused by a combination of tides and mean baroclinic flow over a fjord sill," *Journal of Physical Oceanography*, vol. 45, no. 2, pp. 355–368, 2015.

[19] A. Demuren and H. Grotjans, "Buoyancy-driven flows—beyond the boussinesq approximation," *Numerical Heat Transfer, Part B: Fundamentals*, vol. 56, no. 1, pp. 1–22, 2009.

[20] S. Popinet, "Gerris: a tree-based adaptive solver for the incompressible euler equations in complex geometries," *Journal of computational physics*, vol. 190, no. 2, pp. 572–600, 2003.

[21] J. Marshall, A. Adcroft, C. Hill, L. Perelman, and C. Heisey, "A finite volume, incompressible navier-stokes model for studies of the ocean on parallel computers," *Journal of Geophysical Research*, vol. 102, 1997.

[22] C. S. Yih and C. R. Guha, "Hydraulic jump in a fluid system of two layers," *Tellus*, vol. 7, no. 3, pp. 358–366, 1955.

[23] V. Chu and R. Baddour, "Surges, waves and mixing in two-layer density stratified flow," *Proc. 17th Congr. Intl Assoc. Hydraul. Res*, vol. 1, pp. 303–310, 1977.

[24] I. Wood and J. Simpson, "Jumps in layered miscible fluids," *Journal of Fluid Mechanics*, vol. 140, pp. 329–342, 1984.

[25] J. B. Klemp, R. Rotunno, and W. C. Skamarock, "On the propagation of internal bores," *Journal of Fluid Mechanics*, vol. 331, pp. 81–106, 1997.

[26] Z. Borden, E. Meiburg, and G. Constantinescu, "Internal bores: an improved model via a detailed analysis of the energy budget," *Journal of fluid mechanics*, vol. 703, pp. 279–314, 2012.

[27] M. Li and P. F. Cummins, "A note on hydraulic theory of internal bores," *Dynamics of atmospheres and oceans*, vol. 28, no. 1, pp. 1–7, 1998.

[28] Z. Borden and E. Meiburg, "Circulation-based models for boussinesq internal bores," *Journal of Fluid Mechanics*, vol. 726, 2013.

[29] K. Ogden and K. R. Helfrich, "Internal hydraulic jumps in two-layer flows with upstream shear," *Journal of Fluid Mechanics*, vol. 789, pp. 64–92, 2016.

[30] J. C. Sánchez-Garrido, G. Sannino, L. Liberti, J. García Lafuente, and L. Pratt, "Numerical modeling of three-dimensional stratified tidal flow over camarinal sill, strait of gibraltar," *Journal of Geophysical Research: Oceans*, vol. 116, no. C12, 2011.

[31] P. Baines, "Topographic effects in stratified flows," 1995.

[32] D. D. Padova and M. Mossa, "Hydraulic jump: A brief history and research challenges," *MDPI*, 2021.

[33] G.Bidone, "Experiences sur la propagation des remous.," *Natural History Museum Library*, vol. 30, pp. 195–292, 1820.

[34] R. Riegel and J. Beebe, "The hydraulic jump as a means of dissipating energy," *Miami Conservancy District*, pp. 60–111, 1917.

[35] H. Rouse, T. Siao, and S. Nagaratnam, "Turbulence characteristics of the hydraulic jump," *J. Hydraul. Div*, vol. 84, pp. 1–30, 1958.

[36] H. Rouse, "On the use of dimensionless numbers," *Civil Eng.*, vol. 4, pp. 563–568, 1934.

[37] L. Armi, "The hydraulics of two flowing layers with different densities," *Journal of Fluid Mechanics*, vol. 163, pp. 27–58, 1986.

[38] K. Polzin, K. Speer, J. Toole, and R. Schmitt, "Intense mixing of Antarctic Bottom Water in the equatorial Atlantic Ocean," *Nature*, vol. 380, no. 7, pp. 54–57, 1996.

[39] H. Stommel and H. G. Farmer, "Control of salinity in an estuary by a transition," *J. Mar. Res*, vol. 12, no. 1, pp. 13–20, 1953.

[40] L. St.Laurent and A. Thurnherr, "Intense mixing of lower thermocline water on the crest of the Mid-Atlantic Ridge," *Nature*, vol. 448, no. 9, pp. 680–683, 2007.

[41] D. M. Farmer and L. Armi, "The flow of atlantic water through the strait of gibraltar," *Progress in Oceanography*, vol. 21, no. 1, pp. 1–103, 1988.

[42] D. Farmer and J. Dungan Smith, "Generation of lee waves over the sill in knight inlet," in *Fjord oceanography*, pp. 259–269, Springer, 1980.

[43] L. Armi and D. Farmer, "A generalization of the concept of maximal exchange in a strait," *Journal of Geophysical Research: Oceans*, vol. 92, no. C13, pp. 14679–14680, 1987.

[44] D. Farmer and L. Armi, "Stratified flow over topography: The role of small-scale entrainment and mixing in flow establishment," *Proceedings of the Royal Society of London. Series A: Mathematical, Physical and Engineering Sciences*, vol. 455, no. 1989, pp. 3221–3258, 1999.

[45] J. M. Klymak and M. C. Gregg, "The role of upstream waves and a downstream density pool in the growth of lee waves: Stratified flow over the knight inlet sill," *Journal of physical oceanography*, vol. 33, no. 7, pp. 1446–1461, 2003.

[46] P. F. Cummins, "Stratified flow over topography: time-dependent comparisons between model solutions and observations," *Dynamics of atmospheres and oceans*, vol. 33, no. 1, pp. 43–72, 2000.

[47] K. G. Lamb, "On boundary–layer separation and internal wave generation at the knight inlet sill," *Proceedings of the Royal Society of London. Series A: Mathematical, Physical and Engineering Sciences*, vol. 460, no. 2048, pp. 2305–2337, 2004.

[48] Y. D. Afanasyev and W. R. Peltier, "On breaking internal waves over the sill in knight inlet," *Proceedings of the Royal Society of London. Series A: Mathematical, Physical and Engineering Sciences*, vol. 457, no. 2016, pp. 2799–2825, 2001.

[49] N. Hassanpour, A. Hosseinzadeh Dalir, A. Bayon, and M. Abdollahpour, "Pressure fluctuations in the spatial hydraulic jump in stilling basins with different expansion ratio," *Water*, vol. 13, no. 1, p. 60, 2020.

[50] K. B. Winters and H. E. Seim, "The role of dissipation and mixing in exchange flow through a contracting channel," *Journal of Fluid Mechanics*, vol. 407, pp. 265–290, 2000.

[51] N. Bray, J. Ochoa, and T. Kinder, "The role of the interface in exchange through the strait of gibraltar," *Journal of Geophysical Research: Oceans*, vol. 100, no. C6, pp. 10755–10776, 1995.

[52] M. J. Castro, J. A. Garcıa-Rodrıguez, J. M. González-Vida, J. Macıas, C. Parés, and M. E. Vázquez-Cendón, "Numerical simulation of two-layer shallow water flows through channels with irregular geometry," *Journal of Computational Physics*, vol. 195, no. 1, pp. 202–235, 2004.

[53] C. Wunsch and R. Ferrari, "Vertical mixing, energy, and the general circulation of the oceans," *Annu. Rev. Fluid Mech.*, vol. 36, pp. 281–314, 2004.

[54] S. M. Durski, S. M. Glenn, and D. B. Haidvogel, "Vertical mixing schemes in the coastal ocean: Comparison of the level 2.5 mellor-yamada scheme with an enhanced version of the k profile parameterization," *Journal of Geophysical Research: Oceans*, vol. 109, no. C1, 2004.

[55] D. Holland, R. Rosales, D. Stefanica, and E. Tabak, "Internal hydraulic jumps and mixing in two-layer flows," *Journal of Fluid Mechanics*, vol. 470, pp. 63–83, 2002.

[56] S. Legg and J. Klymak, "Internal hydraulic jumps and overturning generated by tidal flow over a tall steep ridge," *Journal of Physical Oceanography*, vol. 38, no. 9, pp. 1949–1964, 2008.

[57] K. Polzin, J. Toole, J. Ledwell, and R. Schmitt, "Spatial variability of turbulent mixing in the abyssal ocean," *Science*, vol. 276, no. 5309, pp. 93–96, 1997.

[58] J. M. Klymak, J. N. Moum, J. D. Nash, E. Kunze, J. B. Girton, G. S. Carter, C. M. Lee, T. B. Sanford, and M. C. Gregg, "An estimate of tidal energy lost to turbulence at the hawaiian ridge," *Journal of Physical Oceanography*, vol. 36, no. 6, pp. 1148–1164, 2006.

[59] J. Nash, M. Alford, E. Kunze, K. Martini, and S. Kelly, "Hotspots of deep ocean mixing on the oregon continental slope," *Geophysical Research Letters*, vol. 34, no. 1, 2007.

[60] G. A. Lawrence, "On the hydraulics of boussinesq and non-boussinesq two-layer flows," *Journal of Fluid Mechanics*, vol. 215, pp. 457–480, 1990.

[61] E. Kunze, J. F. Dower, I. Beveridge, R. Dewey, and K. P. Bartlett, "Observations of biologically generated turbulence in a coastal inlet," *Science*, vol. 313, no. 5794, pp. 1768–1770, 2006.

[62] W. Munk and C. Wunsch, "The moon and mixing: Abyssal recipes ii," *Deep-Sea Res*, vol. 45, no. 1, pp. 977–2, 1998.

[63] G. Ivey, K. Winters, and J. Koseff, "Density stratification, turbulence, but how much mixing?," *Annu. Rev. Fluid Mech.*, vol. 40, pp. 169–184, 2008.

[64] J. Taylor, S. de Bruyn Kops, C. Caulfield, and P. Linden, "Testing the assumptions underlying ocean mixing methodologies using direct numerical simulations," *Journal of Physical Oceanography*, vol. 49, no. 11, pp. 2761–2779, 2019.

[65] T. Osborn, "Estimates of the local rate of vertical diffusion from dissipation measurements," *Journal of physical oceanography*, vol. 10, no. 1, pp. 83–89, 1980.

[66] S. Hickel, N. Adams, and N. Mansour, "Implicit subgrid-scale modeling for large-eddy simulation of passive-scalar mixing," *Physics of Fluids*, vol. 19, no. 9, p. 095102, 2007.

[67] M. Mucaza, "Complicating factors in hydraulic jumps: the effects of the earths rotation," *Electronic Thesis and Dissertation Repository*, vol. 8166, 2021.

[68] M. L. Waite and P. K. Smolarkiewicz, "Instability and breakdown of a vertical vortex pair in a strongly stratified fluid," *Journal of Fluid Mechanics*, vol. 606, pp. 239–273, 2008.

[69] S. Remmler and S. Hickel, "Direct and large eddy simulation of stratified turbulence," *International journal of heat and fluid flow*, vol. 35, pp. 13–24, 2012.

[70] B. Blocken and C. Gualtieri, "Ten iterative steps for model development and evaluation applied to computational fluid dynamics for environmental fluid mechanics," *Environmental Modelling & Software*, vol. 33, pp. 1–22, 2012.

[71] N. Soontiens and S. E. Allen, "Modelling sensitivities to mixing and advection in a sill-basin estuarine system," *Ocean Modelling*, vol. 112, pp. 17–32, 2017.

[72] S. Legg and A. Adcroft, "Internal wave breaking at concave and convex continental slopes," *Journal of Physical Oceanography*, vol. 33, no. 11, pp. 2224–2246, 2003.

[73] M. Ganotaki and K. A. Ogden, "Influence of channel width variations on structure and mixing of internal hydraulic jumps," 2020.

[74] B. L. White and K. R. Helfrich, "Rapid gravitational adjustment of horizontal shear flows," *Journal of Fluid Mechanics*, vol. 721, pp. 86–117, 2013.

[75] A. Aspden, N. Nikiforakis, S. Dalziel, and J. Bell, "Analysis of implicit les methods," *Communications in Applied Mathematics and Computational Science*, vol. 3, no. 1, pp. 103–126, 2009.

[76] K. Ogden, "Internal hydraulic jumps in shallow flows over topography," in *APS Division of Fluid Dynamics Meeting Abstracts*, pp. E1–003, 2016.

[77] K. G. Lamb, "Conjugate flows for a three-layer fluid," *Physics of Fluids*, vol. 12, no. 9, pp. 2169–2185, 2000.

Curriculum Vitae

Name:	Dylan MacRiner
Post-Secondary Education and Degrees:	University of Western Ontario London, ON 2015-2020 B.E.Sc. University of Western Ontario London, ON 2020 - 2022 M.E.Sc.
Honours and Awards:	MITACS RTA 2020-2021
Related Work Experience:	Teaching Assistant The University of Western Ontario 2020 - 2021